# Search for the Lepton Flavor Violating Decay $Z \rightarrow e\mu$

DISSERTATION

Presented in Partial Fulfillment of the Requirements for the Degree Doctor of Philosophy in the Graduate School of The Ohio State University

By

Waruna Sri Fernando, B.S., M.S.

Graduate Program in Physics

The Ohio State University

2010

Dissertation Committee:

Prof. K. K. Gan, Advisor

Prof. Brian Winer

Prof. Stuart A Raby

Prof. Fengyuan Yang

# ABSTRACT

We present a search for the lepton flavor violating decay $Z \to e\mu$ in proton-proton collisions at a center of mass energy of 7 TeV using approximately 3.1 pb$^{-1}$ of data recorded with the ATLAS detector at the CERN large hadron collider. Candidate events have two isolated high $p_T$ leptons (an electron and a muon), no jets, and little missing transverse energy. We observe no events with $e\mu$ invariant mass above 60 GeV/c$^2$. This demonstrates that we can suppress the $e\mu$ background to a negligible level and are sensitive to exotic $e\mu$ production. We set 95% confidence upper limit on the $Z \to e\mu$ branching ratio of 2.0 $\times 10^{-4}$.

This is dedicated to my mother Eva, my father Lionel, my wife Inoka and my son Hiru.

# ACKNOWLEDGMENTS

# Table of Contents

## Chapters

viii

# List of Figures

# List of Tables

# Chapter 1
## Lepton Flavor Violation

## 1.1 The Standard Model

The Standard Model (SM) of particle physics is a theoretical description of the fundamental building blocks of matter and three of the four known fundamental interactions between them (i.e. strong, weak, and electromagnetic except gravity) expressed using quantum field theory. The fundamental particles of matter are described as a spin 1/2 fermionic excitations of relativistic quantum fields. The interactions or forces between those particles are interpreted as exchanges of integer spin bosonic excitations of relativistic quantum fields.

### 1.1.1 Theoretical Formalism of the SM

There were several attempts to construct a gauge theory for the weak interaction starting with Fermi's theory of $\beta$ decay in 1934 [1]. In this model interaction of particles are point like. Although this model adequately described the low energy behavior of weak interactions, scattering probabilities for some processes become larger than unity (unitary violation) at the energy scale of $\sim 80$ GeV. This unsatisfactory behavior caused the search for the correct theory to continue. In 1957, Schwinger [2] suggested a model with a triplet of fields based on the group $O(3)$. In this model fermions interact weakly by exchange of gauge bosons. The charged gauge bosons were associated with the heavy charged bosons and the neutral gauge boson was identified as the photon. Bludman [3] in 1958, proposed an $SU(2)$ weak isospin group based model which also required three vector bosons. In this model the neutral gauge boson was associated with a new massive vector boson. In

1961 Glashow [4] suggested the gauge group $SU(2) \otimes U(1)$ to accommodate both weak interactions ($SU(2)$) and electromagnetic interactions ($U(1)$). In addition to the gauge boson triplet associated with the generators of $SU(2)$, a neutral field ($B_\mu$) related to $U(1)$ is required in this model. The conserved charge associated with this symmetry is weak hypercharge ($Y$) which is related to the weak isospin and the electric charge. Through spontaneous symmetry breaking, the Higgs mechanism [5] gives mass to particles and, at the same time, preserves the gauge invariance and renormalizability. This model is called the Glashow-Weinberg-Salam model [6] or simply, the SM of electroweak interactions. With the inclusion of the strong force, described by the $SU(3)$ gauge group, the SM became a gauge theory of the group $SU(3) \otimes SU(2) \otimes U(1)$ that describes all three interactions.

### 1.1.2 Fundamental Fermions

The fundamental fermions can be broken into two groups: leptons and quarks. Each of these groups includes three generations of particles. The main difference between the generations of particles is their masses. Each generation of leptons consists of an electrically charged lepton with a named flavor and a neutral lepton called neutrino of the same flavor. However, each generation of quarks has a quark with +2/3 electric charge, a quark with -1/3 electric charge. Quarks have an additional property called color, of which there are three possible values, e.g. red, green, and blue. Charged particles interact via the electromagnetic interaction. Charged and neutral particles interact via the weak interaction. The particles with color interact via the strong interaction.

The $SU(2)$ part of the SM introduces the "weak isospin" $I_3$ and the $U(1)$ introduces the hypercharge ($Y$) quantum numbers. The Gell-Mann-Nishijima formula [7, 8] relates isospin and electric charge:

$$Q = I_3 + \frac{Y}{2}. \tag{1.1}$$

### 1.1.3 Gauge Bosons

According to the SM the three fundamental interactions: strong, weak, and electromagnetic are mediated by gauge bosons. There are three generators for $SU(2)$: $W_\mu^1, W_\mu^2, W_\mu^3$, that,

with the generators of $U(1)$, $B_\mu$, generate the combined $SU(2) \otimes U(1)$ electroweak gauge symmetry group. At low energies, the gauge symmetry is broken, and four physical boson fields appear as linear combinations of the generating fields:

$$W_\mu^\pm = \frac{1}{\sqrt{2}}(W_\mu^1 \mp iW_\mu^2) \tag{1.2}$$

$$Z_\mu = \cos\theta_W W_\mu^3 - \sin\theta_W B_\mu \tag{1.3}$$

$$A_\mu = \sin\theta_W W_\mu^3 + \cos\theta_W B_\mu \tag{1.4}$$

where, $\theta_W$ is the Weinberg angle (weak mixing), which also gives the relationship between the masses of the $W$ and $Z$ bosons to lowest order as:

$$\cos\theta_W = \frac{M_W}{M_Z}. \tag{1.5}$$

The $W_\mu^\pm$ and $Z_\mu$ fields are massive while the photon $(A_\mu)$ is the massless gauge field of the effective $U(1)_{EM}$ symmetry that remains at low energy. The photon field mediates the electromagnetic interaction between charged particles while $W_\mu^\pm$ and $Z_\mu$ bosons mediate the weak force. Gluons are the eight massless gauge fields that mediate the strong interaction between color charged fields. They carry two color charges and are the generators of $SU(3)$ color, which is unbroken at low energy.

### 1.1.4 Scalar Bosons

From experiments it was known that weak interactions are short range and therefore must be mediated by massive particles, but gauge theories naturally lead to massless gauge bosons. The Higgs mechanism was introduced to explain the masses of particles by "spontaneous symmetry breaking." A scalar field known as the Higgs field, which has degenerate vacuum states, occupies a state with a non-zero vacuum expectation value, breaking the symmetry between the degenerate states. All the massive elementary particles acquire mass by interacting with this vacuum Higgs field.

## 1.2 Leptons and Flavors

The muon was discovered in 1936 [9], and, at that time, it was called a meson, but later it was found that the mu meson differs significantly from other mesons, behaving like a "heavy electron". At this point, a natural question arose: is the muon an excited state of the electron, and does it decay back to a low energy electron state via gamma emission ($\mu \rightarrow e\gamma$) similar to that of an excited atom or nucleus? A search for this decay was conducted using cosmic muons. In 1948, Hincks and Pontecorvo [10] concluded that the branching ratio of this decay mode does not exceed a few percent. Similarly, it was found that muon-electron conversion in the field of an atomic nucleus, $\mu^-(A, Z) \rightarrow e^-(A, Z)$ ($A$ is the mass number and $Z$ is the nuclear charge) is also very rare. Both of these results show that the muon is not converting directly into an electron. Also, at this time, it was clear that muons decay by emitting an electron and two neutrinos or are captured by an atomic nucleus by a emitting a neutrino. Muon decay was theoretically studied [11], and, based on the electron energy spectrum, it was shown that the two neutrinos are not identical. The two neutrinos were identified as a neutrino and an anti-neutrino with lepton number ($L$) being conserved. Lepton number was defined as

- $L = +1$ for leptons ($\mu^-, e^-, \nu$)

- $L = $ -1 for anti-leptons ($\mu^+, e^+, \bar{\nu}$)

- $L = 0$ for non-leptons.
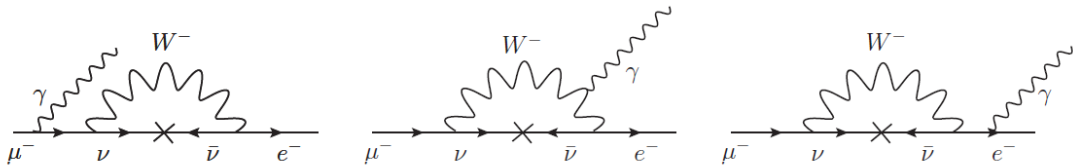


Figure 1.1: Feynman diagram of $\mu \rightarrow e\gamma$.

| | $e^-$ | $\nu_e$ | $\mu^-$ | $\nu_\mu$ | $\tau^-$ | $\nu_\tau$ | $e^+$ | $\bar{\nu}_e$ | $\mu^+$ | $\bar{\nu}_\mu$ | $\tau^+$ | $\bar{\nu}_\tau$ |
|---|---|---|---|---|---|---|---|---|---|---|---|---|
| $L_e$ | +1 | +1 | 0 | 0 | 0 | 0 | -1 | -1 | 0 | 0 | 0 | 0 |
| $L_\mu$ | 0 | 0 | +1 | +1 | 0 | 0 | 0 | 0 | -1 | -1 | 0 | 0 |
| $L_\tau$ | 0 | 0 | 0 | 0 | +1 | +1 | 0 | 0 | 0 | 0 | -1 | -1 |

Table 1.1: Lepton flavor of all known leptons.

At this time the main muon decay channel was $\mu^- \rightarrow e^- \bar{\nu}\nu$. If the two neutrinos were a particle-anti-particle pair, the decay shown in Figure 1.1 is also allowed. The theoretical prediction is $B(\mu \rightarrow e\gamma) \sim 10^{-4}$ [12], but the experimental upper limit was $< 2 \times 10^{-5}$ which was later tightened to $10^{-6}$ [13]. Pontecorvo [10] suggested that the neutrinos coupled to muons and electrons are different and put forward the two-neutrino hypothesis which would forbid the process in Figure 1.1. The two-neutrino hypothesis was experimentally verified at Brookhaven National Laboratory (BNL) by observing muon production without electron production from the scattering of neutrinos produced in pion decays [14]. This result led to the concept of lepton flavor conservation as an extension of lepton number conservation. With the discovery of the third generation of leptons, the tau in 1975 [15] and tau-neutrino in 2000 [16], the complete description of lepton flavor can be summarized as in the Table 1.1.

## 1.3 Charged Lepton Flavor Violation

Since lepton flavor conservation is not "protected" by any known symmetry, searches for Lepton Flavor Violation (LFV) will probe new physics (i.e. physics beyond the SM). The observation of neutrino oscillations is the first indication that the lepton flavor is not conserved [17]. In the case of charged leptons, searches for flavor violations have, so far, yielded null results. Nevertheless, the measured limits can be used to calculate constraints on many theoretical models [18, 19, 20]. A sample of limits on various charged LFV decays is listed in Table 1.2.

| Decay | Upper limit | Confidence level (%) | Experiment |
|-------|-------------|----------------------|------------|
| $\mu \to e\gamma$ | $1.2 \times 10^{-12}$ | 90 | LAMPF [21] & MEGA [22] |
| $\mu \to e\gamma\gamma$ | $7.2 \times 10^{-11}$ | 90 | LAMPF [23] |
| $\mu \to 3e$ | $1.0 \times 10^{-12}$ | 90 | SINDRUM [24] |
| $\tau \to \mu\gamma$ | $4.4 \times 10^{-8}$ | 90 | BABAR [25] |
| $\tau \to e\gamma$ | $3.3 \times 10^{-8}$ | 90 | BABAR [25] |
| $\tau \to 3\mu$ | $3.2 \times 10^{-8}$ | 90 | BELLE [26] |
| $\tau \to 3e$ | $3.6 \times 10^{-8}$ | 90 | BELLE [26] |
| $Z \to e\mu$ | $1.7 \times 10^{-6}$ | 95 | OPAL [27] |
| $Z \to e\tau$ | $9.8 \times 10^{-6}$ | 95 | OPAL [27] |
| $Z \to \mu\tau$ | $1.2 \times 10^{-5}$ | 95 | DELPHI [28] |
| $K_L^0 \to e\mu$ | $4.7 \times 10^{-12}$ | 90 | E391a [29] |
| $D^0 \to e\mu$ | $8.1 \times 10^{-7}$ | 90 | BABAR [30] |
| $B^0 \to e\mu$ | $6.4 \times 10^{-8}$ | 90 | CDF [31] |

Table 1.2: Current upper limits of some LFV decays.

### 1.3.1 Charged LFV in $Z$ Decays

As shown in Table 1.2 the direct upper limit on the branching ratios of the three LFV decays of the $Z$ boson have been obtained by the experiments at Large Electron Positron Collider (LEP). The upper limit on $B(Z \to e\mu)$ was obtained with a data sample of $5.0 \times 10^6$ $Z$ decays with $\sqrt{s} = 88$ - 94 GeV/c$^2$ [27]. For comparison, the Large Hadron Collider (LHC) will produce $3.0 \times 10^7$ $Z$ decays at $\sqrt{s} = 7$ TeV with integrated luminosity of 1 fb$^{-1}$. However with much greater energy and collision rates in a hadron collider, the LHC produces much more background. Cross sections for different physics processes at various energies are shown in Figure 1.2 [32]. Cross sections for the expected backgrounds at $\sqrt{s} = 7$ TeV will be discussed later.

By using the measured upper limit in the branching ratio for low energy process $\mu \to 3e$ and a theoretical model, it is possible to predict a upper limit in the branching ratio for LFV process $Z \to e\mu$ [33]. The most general form of the interaction Lagrangian of a non-SM LFV coupling between leptons $l_i^{\pm}$ and $l_j^{\pm}$ ($i \neq j$) and the $Z$ boson shown in Figure 1.3 (a),

6
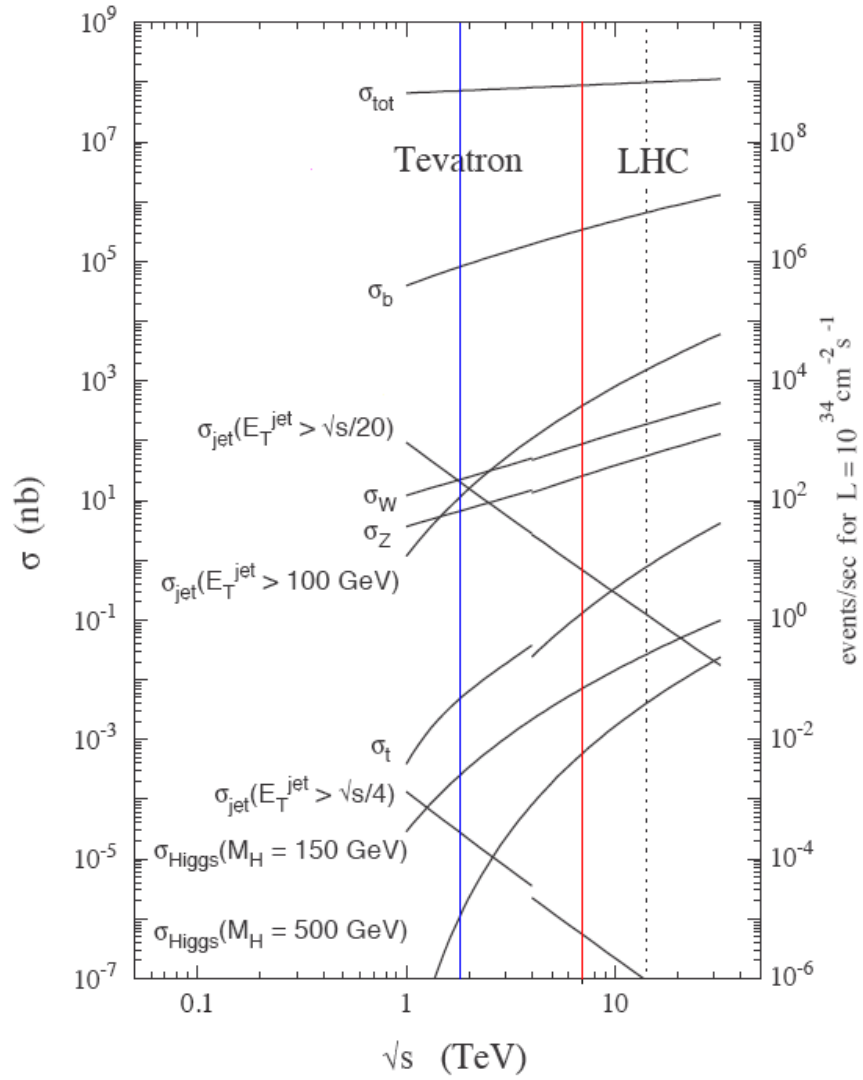
Figure 1.2: Cross sections for various physics processes at different center of mass energies. The blue line indicates the Tevatron energy while the red and dashed lines indicate the current and future LHC energies.
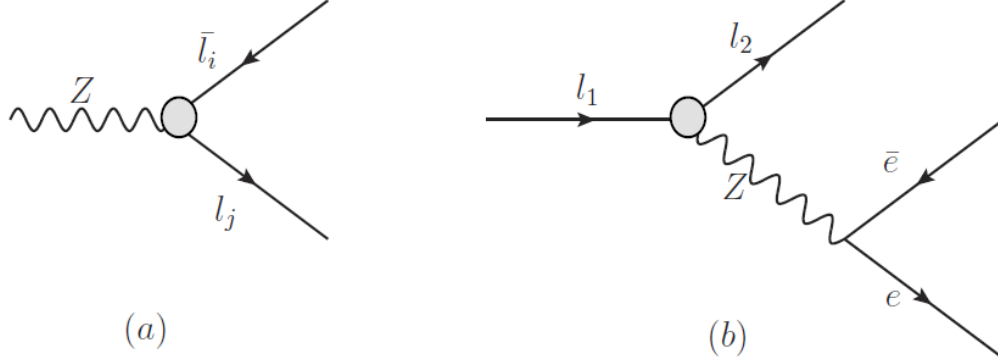
Figure 1.3: Feynman diagrams of $Z \to e\mu$ (a) and $l_1 \to l_2 ee$ (b).

can be written as [33]:

$$\mathcal{L}_{ij} = \quad -i g_Z \bar{l}_i \gamma^\mu \left[ a_L^{ij} \left( \tfrac{1-\gamma_5}{2} \right) + a_R^{ij} \left( \tfrac{1+\gamma_5}{2} \right) \right] Z_\mu l_j$$
$$+ g \bar{l}_i \sigma^{\mu\nu} \tfrac{k_\nu}{M} \left[ b_L^{ij} \left( \tfrac{1-\gamma_5}{2} \right) + b_R^{ij} \left( \tfrac{1+\gamma_5}{2} \right) \right] Z_\mu l_j + h.c. \tag{1.6}$$

where $g$ is the weak coupling constant, $k_\nu$ is the four momentum of the $Z$, $M$ is the high energy scale ($\Lambda \gtrsim \mathcal{O}(\text{TeV})$) associated with the LFVs, and $a_L^{ij}$, $a_R^{ij}$, $b_L^{ij}$, $b_R^{ij}$ are unknown couplings. Since the $\tfrac{k_\nu}{M}$ factor suppresses the effects of the constants $b_L^{ij}$ and $b_R^{ij}$, the branching ratio of the LFV process $Z \to l_i^\pm l_j^\mp$ relative to $Z \to \mu\mu$ can be written as [34]:

$$\frac{B \left( Z \to l_i^+ l_j^- + l_i^- l_j^+ \right)}{B \left( Z \to \mu^+ \mu^- \right)} = \frac{2 \left( \left( a_L^{ij} \right)^2 + \left( a_R^{ij} \right)^2 \right)}{(c_L)^2 + (c_R)^2}. \tag{1.7}$$

In the SM (tree level) $c_L$ and $c_R$ are [34]:

$$c_L = -\frac{1}{2} + \sin^2 \theta_W \approx -0.27$$
$$c_R = \sin^2 \theta_W \approx 0.23.$$

As shown in the Feynman diagram in Figure 1.3(b), the decay $\mu^\pm \to e^\pm e^+ e^-$ can be

considered as $\mu^\pm \to Ze^\pm$, with $Z \to e^+e^-$. Similar to Equation 1.7, we can obtain [34]:

$$\frac{B\left(\mu^\pm \to e^\pm e^+e^-\right)}{B\left(\mu^\pm \to e^\pm \nu\bar{\nu}\right)} = 2\left[3\left(\left(a_L^{e\mu}\right)^2 + \left(a_R^{e\mu}\right)^2\right)\left(c_L^2 + c_R^2\right) + \left(\left(a_L^{e\mu}\right)^2 - \left(a_R^{e\mu}\right)^2\right)\left(c_L^2 - c_R^2\right)\right].$$

(1.8)

Note that it is assumed that $\frac{k_\nu}{M}$ is very small and consequently, the $b^{ij}$ terms are suppressed. With the measured effective couplings $c_L$ and $c_R$, this can be written as,

$$\frac{B\left(\mu^\pm \to e^\pm e^+e^-\right)}{B\left(\mu^\pm \to e^\pm \nu\bar{\nu}\right)} = 0.80\left(\left(a_L^{e\mu}\right)^2 + 0.91\left(a_R^{e\mu}\right)^2\right).$$

(1.9)

The upper limit $B(\mu \to 3e) < 1.0 \times 10^{-12}$ yields the constraint,

$$\left(a_L^{e\mu}\right)^2 + 0.91\left(a_R^{e\mu}\right)^2 < 1.3 \times 10^{-12}.$$

(1.10)

This result can be combined with Equation 1.7 to get $B(Z \to e\mu) < 10^{-12}$. However, the calculation of $B(Z \to e\mu)$ using $B(\mu \to 3e)$ assumes that $\frac{k_\nu}{M}$ is very small. It is therefore important to search for LFV decay at high momentum transfer.

# Chapter 2
# ATLAS DETECTOR

## 2.1 Overview of the LHC and the ATLAS detector

The LHC is a proton-proton collider at the European Organization for Nuclear Research (CERN), Switzerland. It is designed to collide bunches of protons every 25 ns at the center of mass energy of 14 TeV. With $10^{11}$ protons per bunch, the design luminosity is $10^{34}$ $cm^{-2}s^{-1}$ [35]. When the proton beams from the LHC collide, a variety of particles with a broad range of energies are produced. To measure the broad range of particle signatures, A Toroidal LHC ApparatuS (ATLAS) is designed as a general purpose detector. ATLAS is the largest and the most complex high energy physics detector ever built due to the unique challenges of the LHC, the unprecedented energy and extremely high rate of collisions.

Figure 2.1 shows the general layout of the ATLAS detector. The inner part of the detector is used for particle tracking and consists of a combination of discrete, high-resolution semiconductor pixel and strip detectors in its inner most part and straw-tube tracking detectors in its outer most part.

Just outside the tracking region are the electromagnetic and hadronic calorimeters. The electromagnetic sampling calorimeters is designed to measure the energy and position of electromagnetic particles. The hadronic calorimeter is designed to measure the energy and position of hadrons and consist of scintillator-tiles in the barrel region and a liquid-argon calorimeter in the end-caps. The forward calorimeters provide both electromagnetic and hadronic energy measurements, and extend the pseudo-rapidity to $|\eta| = -ln\left[tan\frac{\theta}{2}\right] < 4.9$, where the polar angle, $\theta$, is measured with respect to the $z$-axis.
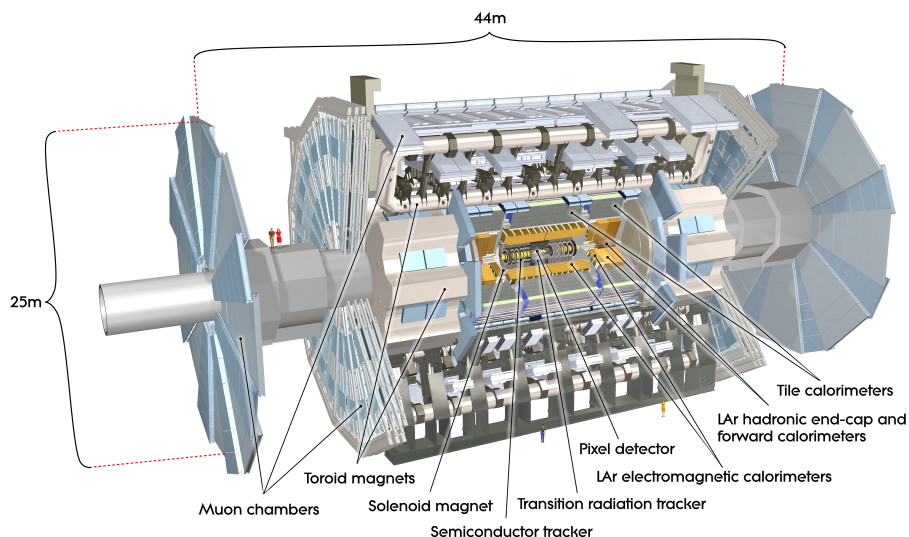
Figure 2.1: Main parts of the ATLAS detector.

The outer most section of the ATLAS detector is the muon spectrometer. A large magnetic field is generated by an air-core toroid system, with a long barrel and two end-cap magnets. Muons are bent in the magnetic field and their trajectory is determined by the tracking chambers.

The interaction rate at the design luminosity is approximately 1 GHz. However based on technology and resource limitations the event data recording is limited to 200 Hz [36]. This requires a very efficient multi level trigger system. The Level-1 (L1) trigger system is hardware based and decides whether to continue processing an event by using a subset of the available data in the harware level, reducing the data rate to approximately 75 kHz. The software based Level-2 (L2) trigger and the Event Filter (EF) provide the reduction to a final data rate of approximately 200 Hz [35].

## 2.2  Magnet System

ATLAS features a system of four large superconducting magnets, one solenoid, and three toroids (one barrel and two end-caps). The complete magnetic system is 22 m in diameter and 26 m in length. The barrel toroid provides a magnetic field of 4.0 T in the central

11

region and the end-cap toroids produce 3.9 T in the end-cap region. Since there are very large forces acting on the windings, those windings are mounted on substantial formers. The windings and formers, are together called the "cold mass" since both are kept at liquid Helium temperatures (4.5 K).

## 2.3 Inner Detector

The Inner Detector (ID) is contained within the central solenoidal magnet, with an outer radius of 1.150 m and a length of 7.024 m. The ID consists of three units, a barrel, and two end-caps. The ID is made up of three independent sub-detectors, the pixel detector, the Semiconductor Tracker (SCT), and Transition Radiation Tracker (TRT).
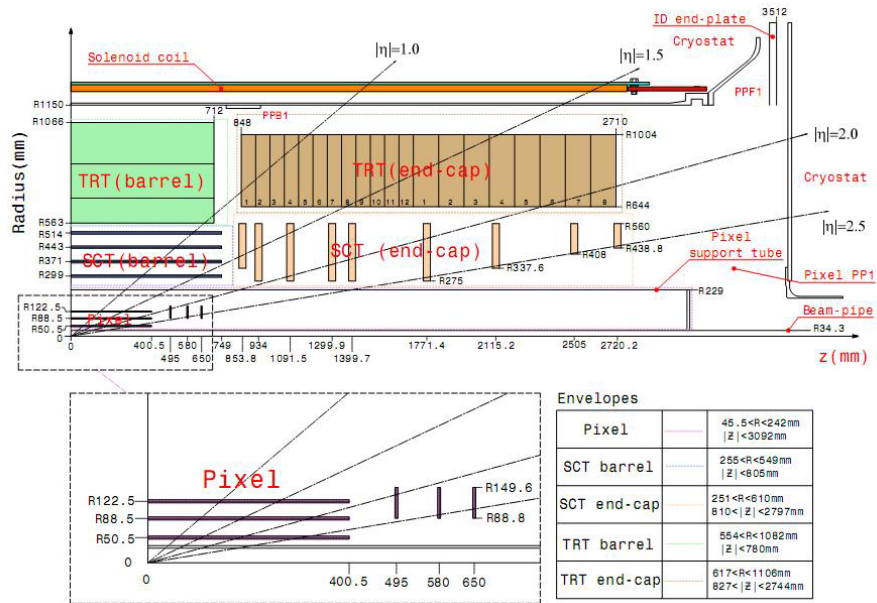


Figure 2.2: ID with sub detector elements in $z - r$ plane. Here PP1, PPB1 and PPF1 are patch-panels for electrical optical and cooling services.

Figure 2.2 shows the ID active envelops and the locations of sub-detectors. The barrel region is covered with high-precision detector layers that are arranged on concentric cylinders around the beam axis, while the end-cap detectors are located in planes perpendicular

to the beam axis as wheels.

The pixel layers and stereo pairs of SCT layers at inner radii provide high resolution pattern recognition capabilities using discrete space points. While the TRT is made of many layers of straw tube elements interleaved with transition radiation material and provides continuous tracking at larger radii. The TRT produce an average of 36 hits per track and it enhances the pattern recognition and improves the momentum resolution for $|\eta| < 2.0$. It also provides electron identification over a wide range of energies. The high radiation environment near the interaction point dictates the design of the sensors and electronics.

## 2.4 Pixel Detector

The pixel detector [37] is located closest to the collision point for precise measurement of vertices. It has a high granularity, provides three high precision measurements over the full acceptance, and primarily determines the impact parameter resolution. It is also used to find long lived particles via vertex location. The pixel detector contains three layers in the barrel region as well as three disks on each end-cap. The active material is 250 $\mu$m thick silicon. Each pixel is 50 $\times$ 400 $\mu$m$^2$. Each pixel module contains 47,268 pixel elements, which are read out by 16 chips. There is with a total of 1,744 modules corresponding to 80 million pixels and an area of 1.7 m$^2$. Since it is placed very close to the collision point, the detector will be exposed to a heavy dose of radiation and all components are required to be radiation hard. The pixel system is described in more detail in Chapter 3.

## 2.5 SCT

The middle component of the inner detector is the SCT which also has barrel and end-cap regions. There are four concentric barrel layers, each 1.53 m long. The two end-caps are formed by 9 disks each. The SCT provides at least four space points per track for coverage up to $|\eta| = 2.5$. This provides measurements to determine particle momentum and charge.

### 2.5.1   SCT Sensors

SCT sensors [38] are built with single sided p-strip on high resistivity n-bulk design (p+, n, n+) with AC-coupled readout strips for low cost and high reliability. The strips are about 80 $\mu$m in pitch and several centimeters in length. The operating voltage, the primary signal ionisation and the simplicity of fabrication determined the sensor thickness of $285 \pm 15$ $\mu$m, while the digitizing precision, granularity, particle occupancy and noise performance determined the strip pitch. All sensors for the barrel region of the SCT have identical rectangular geometry, with 768 readout strips per sensor, whereas the end-caps require four different sensor geometries.

Radiation hardness is one of the key features of these sensors. After several years of radiation exposure, the sensors will change due to "type inversion" (p+, p, n+). In this case the p-n junction moves from the top to the bottom of the wafer. Since the depletion starts at the bottom, it is important to be fully depleted by increasing the voltage. Initially these sensors will operate at about 150 V bias voltage, but after ten years of operation, depending on the sensor position and the integrated luminosity, 250-350 V will be required for good charge collection efficiency. Therefore, the sensors are designed to operate up to 500 V [39]. Also with the radiation dose, leakage currents and noise will also increase with radiation dose. Tracking performance of irradiated modules has been verified in a test-beam [40]. The SCT is kept at low temperature to minimize the reverse annealing since the radiation damage is strongly depend on the temperature of the silicon.

### 2.5.2   SCT Modules and FF Electronics

The SCT sensors are arranged in several configurations due to the geometric constraints. A module consists of 2 pairs of strip sensors glued at a stereo angle of 40 mrad or 20 mrad for barrel or end-cap modules, back-to-back onto thermal pyrolytic graphite baseboard [41].

Each module reads out with 128-channel ASICs called the ABDC3T chip [42]. This ASIC is fabricated using the radiation tolerant DMILL BiCMOS process and designed to work with the 40 MHz LHC bunch crossing rate.

The main functional blocks of the ASIC are Front-End (FE), input register, pipeline, de-randomizing buffer, command decoder, readout logic, and threshold and calibration control sections [42]. The FE section performs charge integration, pulse shaping, and amplitude discrimination. The DAC provides the threshold value for the amplitude discrimination. The outputs of the discriminators are latched to a pipeline. The 132-bit length binary pipeline keeps the data until the receipt of a L1 signal. If an event passes the trigger, the corresponding set of values, together with their neighbors in time, are copied into the readout buffer serving as a de-randomizing buffer. Finally the data is compressed and written into the readout buffer to be transmited off the chip optically, in a fashion similar to the pixel optical system [43] to be described in Chapter 4.

### 2.5.3   SCT performance

The spatial residual distributions of data with the current alignment are compared to the MC with perfect alignment for the barrel and end-cap in Figure 2.3 [44]. The hit efficiency is measured to be 99.7% [45].
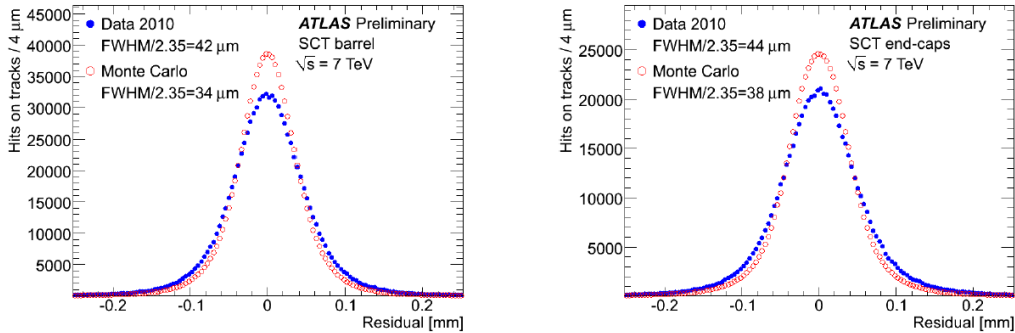


Figure 2.3: Residual distributions of 7 TeV data from 2010 and MC with perfect alignment (red) in the SCT barrel (left) and end-cap (right).

## 2.6 TRT

The TRT is the outermost part of the inner detector. The TRT measures at least 22 points per track for the pattern recognition [46]. The TRT itself comprises a barrel and two end-caps as shown in Figure 2.2.

### 2.6.1 TRT Drift Tubes

At larger radii it is too expensive to cover the large areas with silicon strip detectors, therefore, gaseous drift detectors, called "straw tubes", are used in the TRT. The tubes [46] are 4 mm in diameter and 40 - 150 cm long and hold a thin gold-plated tungsten wire (with a diameter of 30 $\mu$m) on their axis. The straw tubes are arranged axially in the central barrel and radially in the two end-caps.

The straw tube [46] wall is made out of two 35 $\mu$m thick multi-layer films bonded back-to-back. The bare material, a 25 $\mu$m thick Kapton 100VN film, is coated on one side with a 0.2 $\mu$m Al layer which is protected by a 6 $\mu$m thick graphite-polyimide layer. The back (other) side of the wall is coated with a 5 $\mu$m polyurethane layer to heat-seal the two films. Carbon fibers are used for mechanical stability and for reducing the effective resistance of the straws. The straws are cut to 144 cm for barrel and 37 cm for end-caps. The straw wall acts as the cathode and a gold plated tungsten wire acts as anode. The straw is filled with a gas mixture of Xe:$CO_2$:$O_2$ in 70:27:3. The Xe fraction of 70% was chosen for efficient of X-ray absorption, transition radiation performance, operational stability, and electron collection time. $CO_2$ provides a constant drift velocity, low longitudinal diffusion, and small electron deflection in magnetic fields. $O_2$ is added to increase the UV absorption capacity.

The anode wires are split at the middle of most barrel straws by a 6 mm glass capillary to make the active length of the wires 71.2 cm, which are connected to the readout in both ends of the straw. In the inner nine layers of barrel modules, wires are subdivided into three segments and only 31.2 cm long end-segments are connected to readout.

### 2.6.2 TRT Modules and FE Electronics

The barrel TRT is divided into three rings of 32 modules each, while the end-cap TRT has two types of wheels with either 12 or 8 modules. Each module is built with a carbon fiber laminate shell and an internal array of straws that form a uniform axial array with a mean spacing of 7 mm, embedded in a matrix of polypropylene fibers serving as the transition radiation material.

The FE electronics [47] of the TRT includes analogue signal processing and threshold discrimination to detect signals from both minimum ionising particles and transition radiation. These features are implemented in two on-detector ASICs called Amplifier Shaper Discriminator Base Line Restoration Integrated Circuit (ASDBLR) and Drift-Time Measuring ReadOut Chip (DTMROC). ASDBLR is a 8-channel analog ASIC while DTMROC is a 16-channel digital. The ASDBLR design is based on a differential circuit with base line restoration circuit. The DTMROC chip receives its input information from two ASDBLR chips, stores data in a memory pipeline of 3.2 ms long, until a L1 trigger. Following a L1 trigger, the data stored in the pipeline is read out by the back-end electronics.

### 2.6.3 TRT Performance

The unbiased spatial residual for the barrel and the end-caps are shown in Figure 2.4 [48]. The barrel resolution for data (142 $\mu$m) and MC (143 $\mu$m) are in good agreement, however the end-cap resolution for data is 161 $\mu$m, but for MC it is only 135 $\mu$m. Unlike the barrel, the rate of tracks in the end-cap from cosmic runs is very small due to geometric reasons. Hence the end-cap was not studied and calibrated as well as the barrel.

Hit reconstruction efficiency is another important parameter for TRT performance. Figure 2.5 [48] shows the hit reconstruction efficiency as a function of the track's distance of closest approach to the wire. There is good agreement between data and MC.
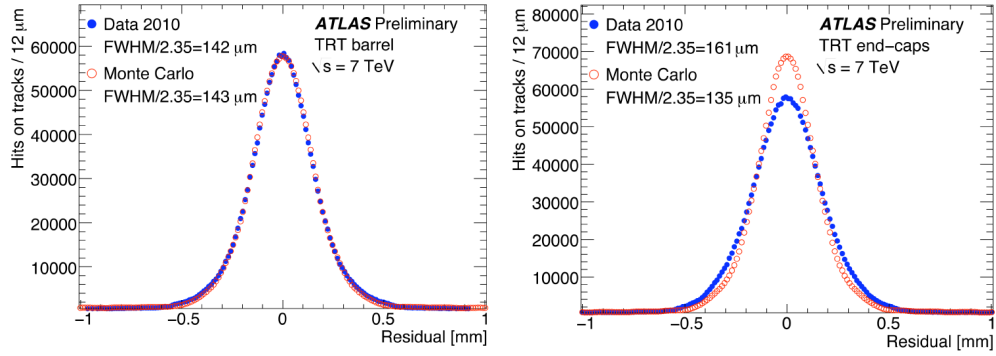
Figure 2.4: TRT spatial residual for barrel (a) and end-caps (b) with 7 TeV data.
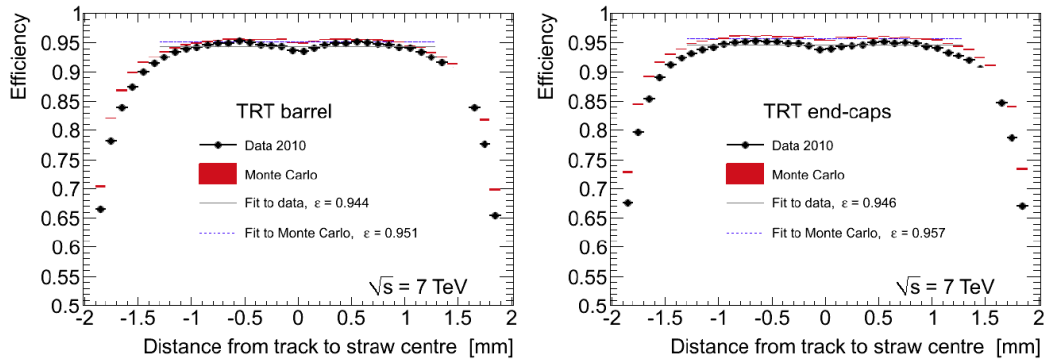


Figure 2.5: TRT barrel (left) and end-cap (right) hit reconstruction efficiency as a function of distance of closest approach of the track to the straw centre for 7 TeV data and MC.
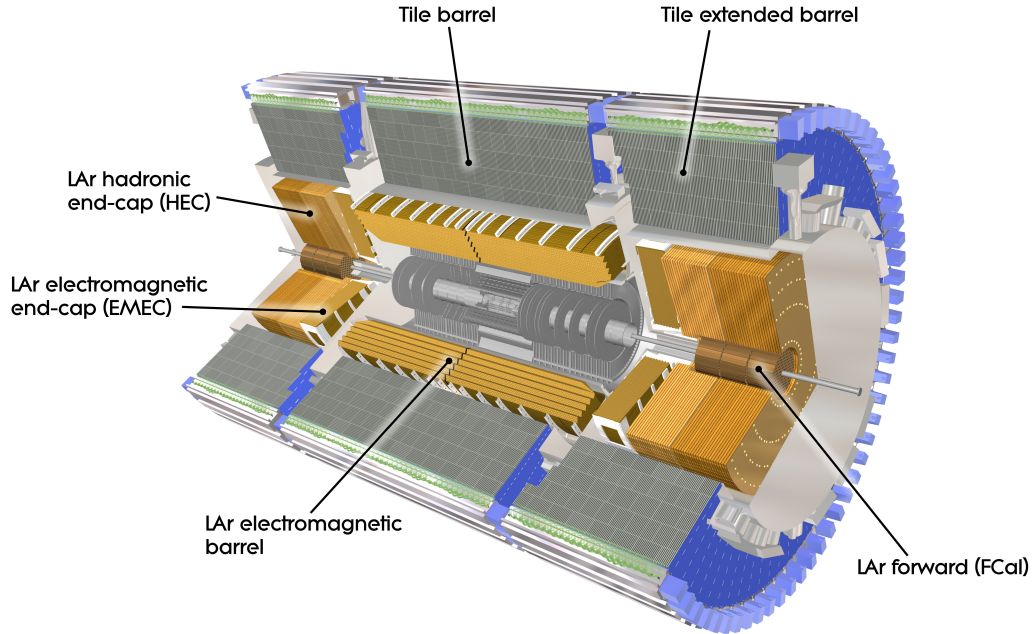
Figure 2.6: The ATLAS calorimeter.

## 2.7 Electromagnetic Calorimetry

The ATLAS electromagnetic calorimeter system [49] consists of a ElectroMagnetic Barrel Calorimeter (EMBC) and an ElectroMagnetic End-cap Calorimeter (EMEC) as shown in Figure 2.6. Liquid argon is used as the active medium due to it's intrinsic linear behavior, stability of response over time, and its intrinsic radiation-hardness. The precision electromagnetic calorimeters are built with lead accordion shape absorbers and electrodes. This geometry allows the calorimeters to have several active layers in depth, three in central region ($0 < |\eta| < 2.5$) and two in the forward region ($2.5 < |\eta| < 3.2$) and in the overlap region between the barrel and the EMEC.

### 2.7.1 EMBC

The EMBC [50] is made with two half barrels of 3.2 m long, with inner and outer diameters of 2.8 and 4.0 m, respectively. Each half barrel covers $|\eta| < 1.475$.

The main components of the EMBC are absorbers, G10 precision bars, electrodes, and spacers as shown in Figure 2.7. The absorbers are made of lead plates glued between two stainless steel sheets with resin impregnated glass fibre fabric. To provide space for the electrode connectors and to position each absorber precisely absorbers are enclosed in a groove of a G10 fiberglass epoxy composite bar. The readout electrodes are made with three conductive copper layers separated by insulating polyimide sheets. By keeping the two outer layers at the HV potential, the inner layer is used to read out the signal through capacitive coupling. With the operating voltage of 2000 V and a drift gap on each side of the electrode at 2.1 mm, the total drift time is about 450 ns. The spacers are used to keep the electrodes centered between two consecutive absorbers.
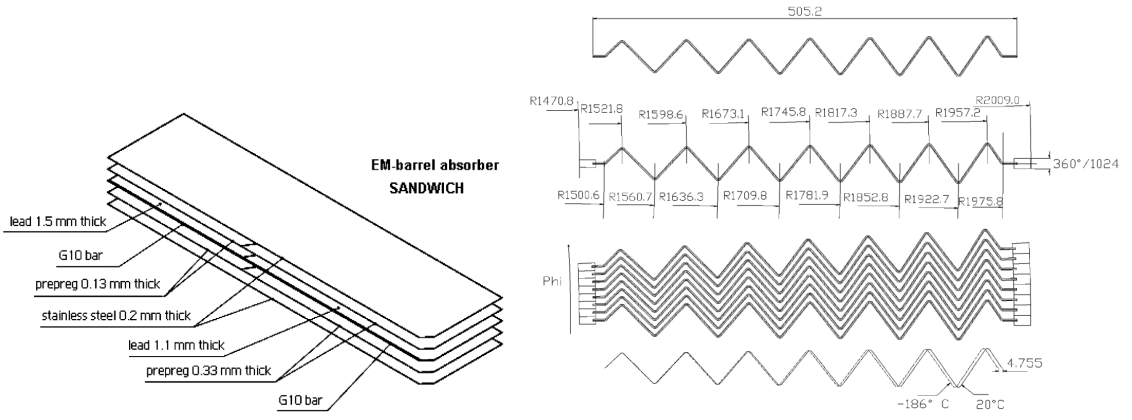


Figure 2.7: An absorber sandwich, before being folded into an accordion shape (left) and accordion shaped absorber profile (right).

Each half barrel is divided into 16 modules. The total thickness of a module varies from 22 to 30 radiation lengths ($X_0$) in the region $0 < |\eta| < 0.8$ and from 24 to 33 $X_0$ in 0.8 $< |\eta| < 1.3$.

Each module is constructed with 16 absorbers folded into accordion shape. Accordion shape geometry provides a full coverage in $\phi$ without any cracks. The folding angles of the waves vary with radius to keep the liquid argon gap constant as shown in Figure 2.7. All these features lead to a uniform performance in terms of linearity and resolution as a

function of $\phi$.

A module has four layers, presampler, front, middle, and back. A thin liquid argon layer of 11 mm in depth is used as a presampler to read the shower in front of the calorimeter (material in front of the calorimeter is about 1.5 $X_0$). The front layer is very fine grained to identify $\gamma/\pi^0$. The middle layer is optimized to contain photon showers up to 50 GeV. The main purpose of the final compartment or the back layer is differentiation of hadronic and electromagnetic showers.

### 2.7.2 EMEC

The EMEC [49, 51, 52] consist of two wheels, one on each side of the the EMBC, to cover the region $1.375 < |\eta| < 3.2$. The EMEC is also a lead liquid argon sampling calorimeter with interleaved accordion shaped absorbers and electrodes. Unlike the EMBC, the absorber plates are arranged radially, so the accordion waves are parallel to the front and back edges of the detector as shown in Figure 2.8 (left).
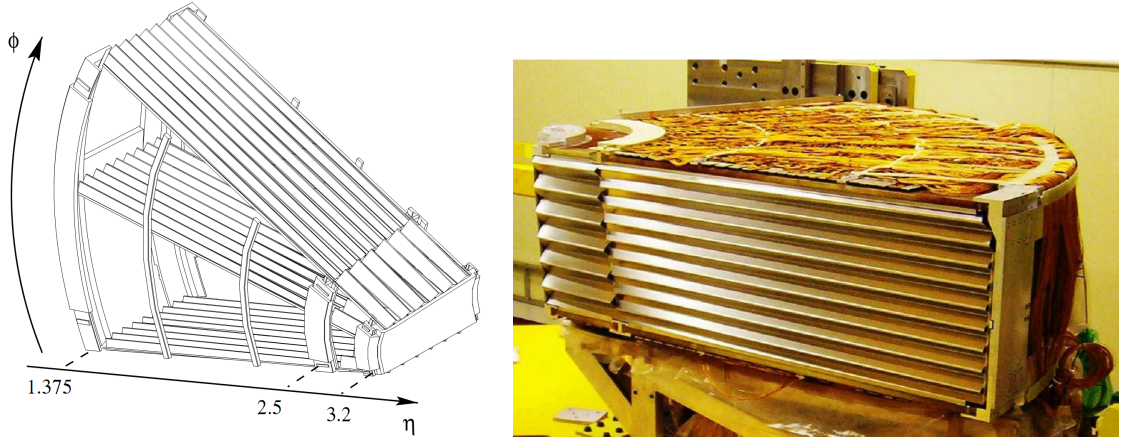


Figure 2.8: Schematic view (left) and side view (right) of an EMEC module.

To keep the uniformity in $\phi$ the liquid argon gap needs to be increased with the radius. It is therefore necessary to change the wave height and the folding angle with radius. Due to technical reasons the folding angle can not be set outside the region 60°−120°. Each

end-cap calorimeter is therefore builds with two coaxial wheels. The boundary between these two wheels is located at $|\eta| = 2.5$, with a crack of 3 mm wide, which is filled with low density material. Each end-cap wheel is divided into eight wedge-shaped modules for handling during construction.

Similar to the EMBC, the absorbers in end-caps are made of lead plates of 1.7 (2.2) mm thick for the outer (inner) wheel, reinforced with two layers of 0.2 mm thick stainless steel and glued using a 0.15 mm thick glass fiber adhesive. Outer wheel absorbers have nine waves while inner wheel absorbers have six waves. The readout electrodes are made with three copper layers insulated by two Kapton polyimide sheets. Two external layers provide the high voltage to the gaps with liquid argon, while the middle layer reads signal by capacitive coupling. The electrodes are kept centered in the liquid argon gap between the absorbers with the spacers.

The detector signal is inversely proportional to the liquid argon gap thickness. Since the liquid argon gap change with the radius, the sampling fraction along the radius partially compensate each other. To make $z$ independent signal the electric field strength needs to change continuously. However, due to technical reasons the high voltage was varied in steps.

## 2.8  Hadronic Calorimeters

The ATLAS hadronic calorimeter system consists of a scintillator-tile hadronic Calorimeter (TileCal), a liquid-argon Hadronic End-Cap Calorimeter (HEC), and a liquid-argon Forward Calorimeter (FCal).

### 2.8.1  TileCal

The TileCal [53] is a sampling calorimeter built with steel as the absorber and scintillator as the active detecting medium. The scintillation light is read out using wavelength-shifting fibers coupled to photomultiplier tubes. It covers the region $|\eta| < 1.7$ and is constructed in three sections: a central barrel 5.640 m long and two extended barrels 2.900 m long, each having an inner radius of 2.288 m and an outer radius of 4.230 m.
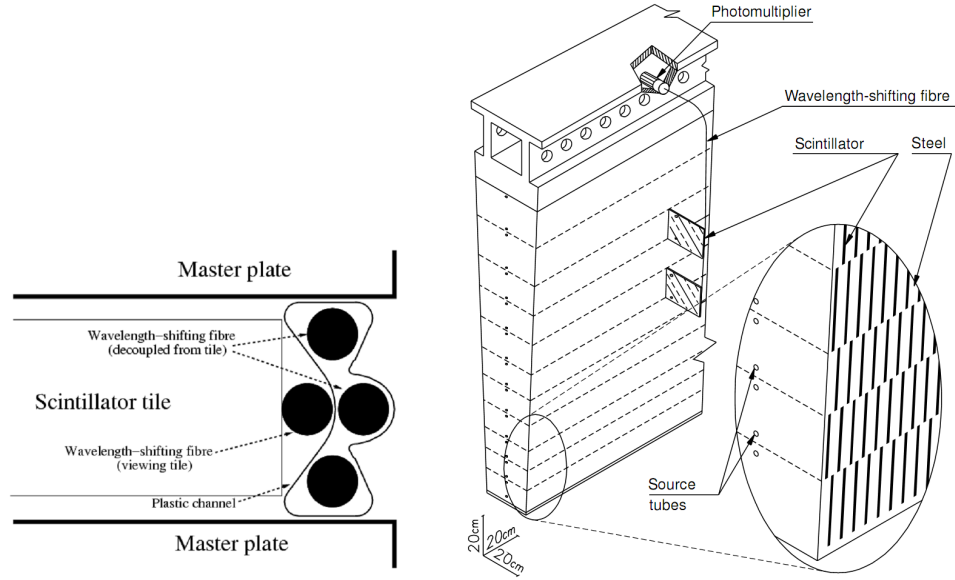
Figure 2.9: A schematic of the integration between the TileCal module absorber structure and the optical components (left). A schematic of the TileCal module including the optical readout, tiles, fibers, and photo-multipliers (right).

For easy construction, each barrel is built with 64 modules or wedges. The orientation of the scintillator tiles are kept radially and normal to the beam line for seamless azimuthal coverage as shown in Figure 2.9 (right). The module structure was made with 5 mm thick master plates and 4 mm thick spacer plates glued in a zigzag fashion to form the pockets in which the scintillator tiles are located. As illustrated in Figure 2.9 (left), wavelength shifting fibers are inserted in channels located between each of the pairs of full-length plates. A plastic channel is used to decouple the fibers from other scintillator tiles. The photo-multiplier tubes and all the FE electronics are highly integrated in 1.4 m long aluminium units, called drawers. A $^{137}$Cs radioactive source, a laser, and a charge injection circuit are integrated into the module for calibration. The longitudinal and transverse readout granularity of first two layers are $\Delta\eta \times \Delta\phi = 0.1 \times 0.1$ and for the last layer $0.2 \times 0.1$ [49].

## 2.8.2 HEC

The HEC [54] covers the range $1.5 < |\eta| < 3.2$ for the hadronic showers. Copper is chosen as the absorber as having the required radiation length to fully contain hadronic showers in the available space. Liquid argon is the chosen as the active detecting medium, due to its radiation tolerance and intrinsic linear behavior. The HEC shares the liquid argon end-cap cryostats with the EMEC and FCal as illustrated in Figure 2.10. The HEC consists of two front wheels (HEC1) and two rear wheels (HEC2). Each HEC wheel is made with 32
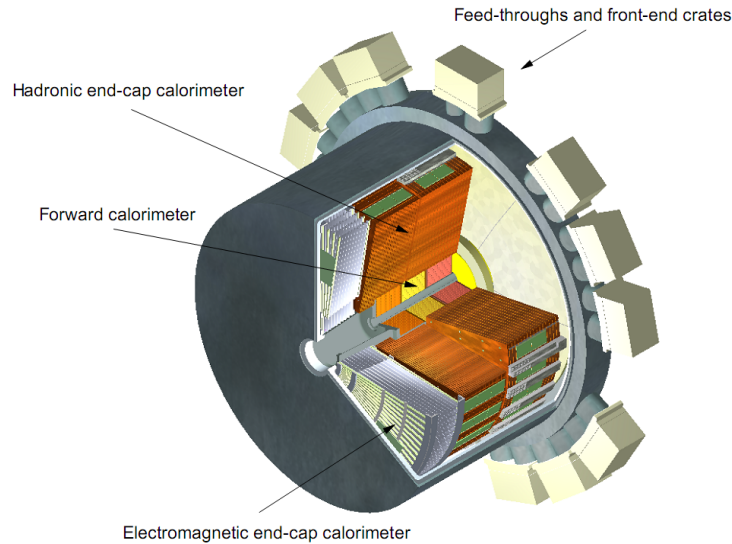


Figure 2.10: Locations of the three end-cap calorimeters inside the end-cap cryostat.

identical wedge-shaped modules, as shown in Figure 2.11 (right). The modules of HEC1 are constructed using 24 copper plates with a thickness of 25 mm and a 12.5 mm thick front plate. The HEC2 modules are constructed using 16 copper plates with 50 mm thickness and a 25 mm thick front plate. The sampling fractions for minimum ionizing particles in HEC1 and HEC2 are 4.4% and 2.2% respectively. The first nine plates of HEC1 have an inner radius of 372 mm. The remaining plates of HEC1 and all plates of HEC2 are 475 mm. Seven stainless-steel tie-rods provide the structural strength of the modules and maintain

the 8.5 mm gap between the plates.
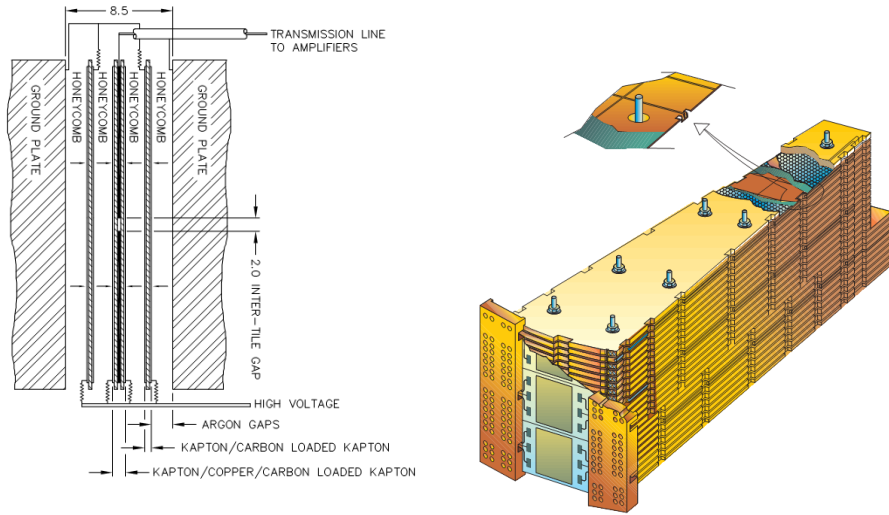


Figure 2.11: A schematic of the HEC module (left) and HEC readout structure (right).

To increase the reliability, each LAr gap is divided by three parallel electrodes into four drift spaces of about 1.8 mm as shown in Figure 2.11 (right). The central electrode is connected to read out, while the side electrodes only provide high voltages. This high voltage planes form an Electro-Static Transformer (EST), which is equivalent to a 3.6 mm gap with 3600 V. This prevents the greater ion build-up associated with high voltages specially in high $|\eta|$. For the nominal high voltage, the typical drift time for electrons in the drift zone is 430 ns.

### 2.8.3 FCal

The FCal [55] system of ATLAS consists of three parts: one electromagnetic module (FCal1) and two hadronic modules (FCal2 and FCal3). These FCal's are located in the end-cap cryostats and cover the range $3.1 < |\eta| < 4.9$. LAr was chosen as the active detecting material due to its radiation tolerance and intrinsic linear behavior. Copper was chosen

as the absorber of FCal1 to optimize the energy resolution and the heat removal, while tungsten was chosen as the absorber for FCal2 and FCal3, to minimise the lateral spread of hadronic showers. To reduce the background in the muon end-cap a shielding plug made of a copper alloy has been mounted behind FCal3.

Since the FCal modules are located at high $\eta$ and approximately 4.7 m from the IP, they are exposed to high particle flux. To reduce the ion buildup and to increase the absorption length, FCals are designed with very small LAr gaps. This also provides a faster response. In order to achieve this, a structure of small-diameter rods (anode) is placed at the center of tubes (cathodes) separated with radiation hard fiber which is wound around the rod as illustrated in Figure 2.12.
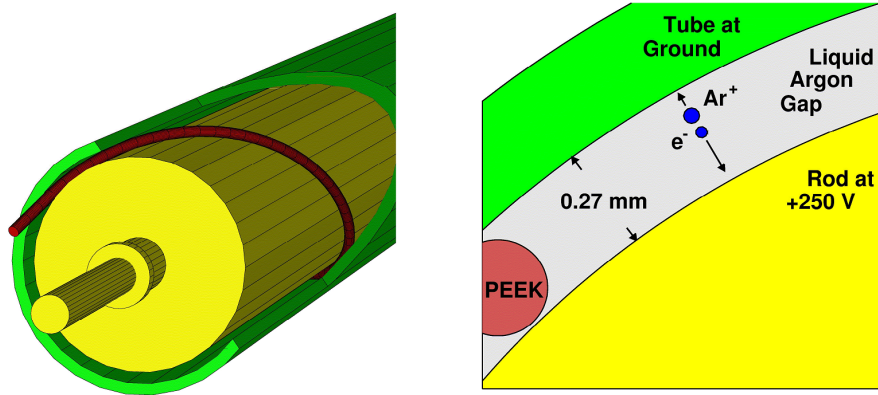


Figure 2.12: Cut-away and cross-section view of an FCal electrode.

FCal1 absorber is made of stacked copper plates and holes drilled in them to insert the electrode structures (copper rods on copper tubes). Electrode structure of FCal2 and FCal3 is the same as in FCal1 but with tungsten rods. The absorber in FCal2 and FCal3 is made with tungsten slugs arranged in a honeycomb structure. The depths of FCal1, FCal2, and FCal3 are 27, 91.3, and 89.2 $X_0$ respectively.

As shown in Figure 2.12 (right), the rod is held at positive high voltage with respect to the tube of the electrode to make an electric field inside the gap of $\sim$1.0 kV/mm. A

current pulse is generated when the showering particles ionize the liquid argon. Read out electronics are connected to interconnect boards placed on the faces of the modules. These interconnect boards are then connected to summing boards which are mounted on the back of the the HEC. Summing boards can sum 4 inputs using transmission-line transformers.

The signal then feeds into the FE electronics mounted at the downstream outer layer of the cryostat. The current signal is converted to voltage, amplified by the pre-amplifier and feed into a CR-RC$^2$ (one differentiation and two integration stages) shaper. The output of the shaper is connected to an analog pipeline which samples the shaper pulse at 25 ns. The pipeline is 128 samples deep, so that it can keep pulses until a L1 trigger. If the event passes the L1 trigger the pulse is digitized with 12-bit ADCs and sent to the counting room.

## 2.9  Muon Spectrometer

The muon spectrometer [49] is the outermost part of the ATLAS detector. It is designed to measure the momentum of charged particles in $|\eta| < 2.7$. The muon spectrometer also has a barrel and two end-caps. There are three barrels around the beam axis at radii of 5.0 m, 7.5 m, and 10.0 m and eight end-cap wheels at $|z| = 7.4$ m, 10.8 m, 14.0 m, and 21.5 m. To allow services to the solenoid magnet, a gap is kept between the chambers, but by overlapping chambers the gap in the coverage is minimized.

### 2.9.1  MDT

The momentum of a muon is measured precisely using the Monitored Drift Tube Chambers (MDT). MDT's are pressurized aluminum drift tubes with 29.97 mm in diameter and filled with $Ar/CO_2$ (93:7) at a pressure of 3 bar. Electrons resulting from ionisation are collected from an anode wire of 50 $\mu$m in diameter at a potential of 3080 V. On each MDT chamber, three or four layers of tubes are arranged in two layers as shown in Figure 2.13. These chambers are equipped with RASNIK optical straightness monitors to control in-plane alignment. In order to adjust for the thermal expansion of the tubes and the temperature of the gas, temperature monitors are also installed. To predict the E×B effect on drift time,
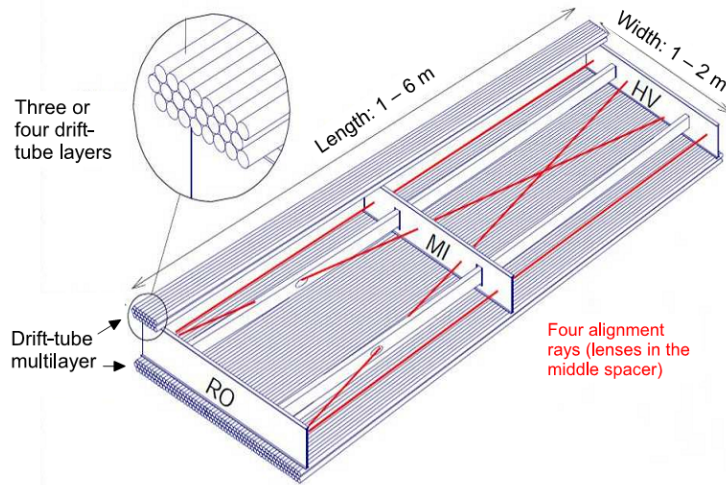
Figure 2.13: Mechanical structure of a MDT chamber, showing frame, two multi-layers of drift tubes, and optical alignment rays. RO and HV are designated the location of the readout electronics and high voltage supplies.

magnetic filed sensors are also installed in MDT chambers.

As a result of tight tolerances maintained during the construction and continued monitoring of deformations, the positions of MDT wires in a tube layers are known with high accuracy, which is only limited by the single tube resolution of 80 $\mu$m. With two multi-layers of 3 (4) tubes, the resolution of the central point of the track segment is 35 (30) $\mu$m. MDTs are designed and tested to tolerate a high radiation dose [56].

The readout system [57] of the MDT consists of a on-chamber mezzanine cards, Chamber Service Modules (CSM), and MDT ReadOut Drivers (ROD) in the USA15 cavern. The mezzanine card reads the signals from the Amplifer/Shaper/Discriminator (ASD) chip and routes to Time-to-Digital Converter (TDC). The output of this stage consists of arrival times of leading and trailing edges with an identification code to track the origin. One mezzanine card, with a TDC and 3 ASDs, serves 24 tubes. One MDT chamber contains a CSM which controls up to 18 mezzanine cards. The CSM collects the outputs from TDC and send them to ROD in the USA15 service cavern.

### 2.9.2 CSC

Cathode-Strip Chambers (CSC) are multiwire proportional chambers in the high particle density regions, $2.0 < |\eta| < 2.7$. The detector has high granularity, providing good two-track and timing resolution and low neutron sensitivity.

CSCs anode wires are (30 $\mu$m diameter) oriented in the radial direction. Cathodes strips in one layer are oriented perpendicular to the wires to read the longitudinal coordinate and the other layer parallel to the wires providing the transverse coordinate. CSC chambers are filled with Ar:$CO_2$ (80:20) and operate at 1900 V.

The CSCs are built with large and small chambers in two planes so that they cover the full $\phi$ without cracks. There are two disks with 8 big and 8 small chambers in each disk. Each chamber has four CSC planes generating four independent measurements along each track.

The readout system [49] consists of an Amplifier and Shaping Module (ASM-I), a Switched Capacitor Array (SCA), Analog to Digital Converter (ADC), multiplexer, and a optical link. First the input from the cathode is sampled and held at ASM-I and then stored in SCA until an L1 Trigger occurs. If the event passed the L1 trigger, the stored data are digitised, multiplexed and transferred to the ROD.

### 2.9.3 Trigger Chambers

Muon trigger chambers are designed to deliver fast and coarse tracking and energy information for the L1 trigger, identify bunch-crossing and discriminate on muon transverse momentum. Resistive Plate Chambers (RPC) are used for barrel ($|\eta| \leq 1.05$) and Thin Gap Chambers (TGC) are for the end-cap ($1.05 \leq |\eta| \leq 2.4$). The placements of trigger chambers are shown in Figure 2.14.

### 2.9.4 RPC

An RPC is a gaseous parallel electrode-plate detector. Each chamber contains four resistive plates, with a 2 mm spacing, in a 4.9 kV/mm electric field. Ionizing tracks produce
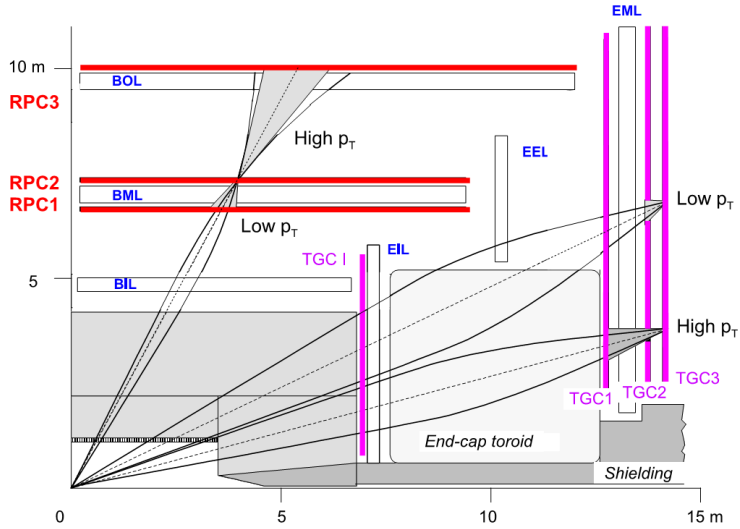
Figure 2.14: Schematics of the muon hardware trigger systems.

avalanches which are read from metallic strips mounted on the resistive plates. The gas mixture used is $C_2H_2F_4$:Iso-$C_4H_{10}$:$SF_6$ (94.7:5:0.3) chosen for its relatively low operating voltage, non-flammability, and low cost. The RPC system consists of RPC1, RPC2, and RPC3 at different radii as shown in Figure 2.14.

### 2.9.5 TGC

TGC's are multiwire chambers, with wire spacing of 1.8 mm and wire to cathode distance of 1.4 mm. The chambers are filled with a highly quenching gas mixture of $CO_2$:n-$C_5H_{12}$ (55:45). This allows TGCs to operate in a quasi-saturated mode for good timing resolution. Since n-$C_5H_{12}$ is a flammable gas, all TGC units are sealed in a gas-tight envelop. The envelop is continuously flushed with $CO_2$ to keep the chambers dry and to dilute any potential leaks.

### 2.9.6 Readout System of RPC and TGC

The readout system [58] receives the signals from the wires (TGC) and strips (RPC). First, the signals are amplified and then synchronized with the beam crossing signal. After a simple coincidence filter (using layers) tracks are sent to a coincidence matrix, to quickly

30

search for coincidences corresponding to muon tracks in a momentum range. Low $P_T$ triggers are defined from coincidences between strips in RPC1 and RPC2. If a hit is also found in the RPC3 then it is defind as a high $p_T$ trigger.

## 2.10 Trigger System

The ATLAS trigger system consists of three levels; L1, L2, and EF. L2 and EF form the High-Level Trigger (HLT). The L1 trigger is built with custom hardware, while the HLT is based on software. A block diagram of the ATLAS trigger and data acquisition system is shown in Figure 2.15.
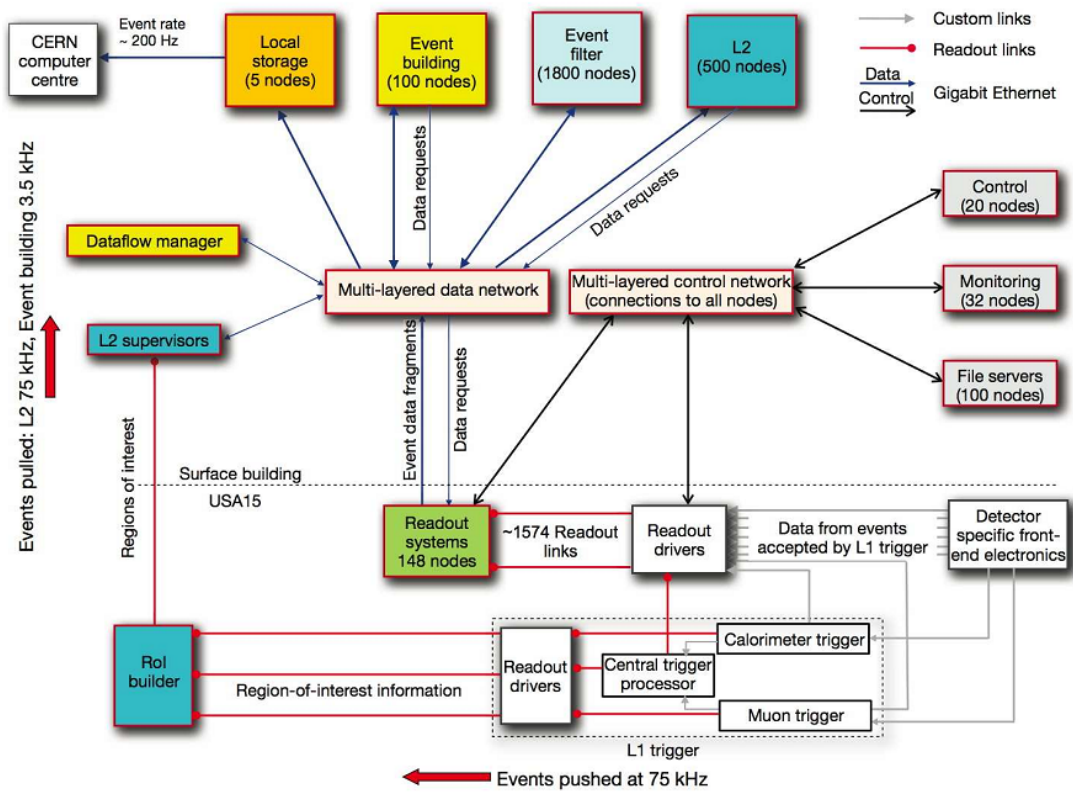


Figure 2.15: Block diagram of the ATLAS trigger and data acquisition system.

### 2.10.1 The L1 Trigger

Based on the information from all the calorimeters and a subset of muon detectors (RPC and TGC), the L1 trigger searches for signatures of high-$p_T$ muons, electrons/photons, jets, $\tau$ decays, missing transverse energy, and large total transverse energy for the initial event selection. The detector is designed to handle a maximum rate of 75 KHz, starting from a collision rate of 40 MHz (every 25 ns). The final L1 trigger decision is made by the Central Trigger Processor (CTP), which compares the information from L1 Calorimeter Trigger (L1Calo) and L1 muon trigger, with the trigger menu. The trigger menu has 256 items, and each item has a combination of requirements. The decision from the CTP is finally sent to the FE and readout system through the Trigger Timing and Control (TTC) system.

### 2.10.2 L1Calo

L1Calo [59] processes the analog information from the trigger towers located in the electro-magnetic and hadronic calorimeters and sends the results to the CTP. L1Calo has three main subsystems; preprocessor, Jet/Energy-sum Processor (JEP), and Cluster Processor (CP). The analog signals are converted to digital and processed with a digital filer to associate them with the correct bunch crossing at the preprocessor. Both CP and JEP subsystems receive the data in parallel. The CP subsystem mainly identifies electrons, photons, and $\tau$ leptons with transverse energy above the programmed thresholds. It also checks the isolations and the multiplicities of those objects. At the same time, JEP subsystem identifies jets and calculates the total transverse energy in order to find the missing transverse energy. Finally the CTP issues a L1 Accept (L1A) decision based on the data from CP and JEP. In the event of a L1A, the L1Calo subsystem transfer the input data, intermediate calculations and trigger results to the RODs and to the Region of Interest (RoI) builder.

### 2.10.3 Muon Trigger

The L1 muon trigger uses the information collected from dedicated detectors installed in the barrel (RPC) and end-cap (TGC). These detectors also provide the identification informa-

tion of the bunch-crossing of the muon candidate. Three RPC and four TGC trigger stations are installed in the muon trigger system as shown in the Figure 2.14. Each trigger station is built with multiple layers, and the trigger algorithm requires coincidence of hits in different layers and several trigger stations for different triggers. A programmable coincidence logic system operates with six thresholds, three associated with both low and high-$p_T$ trigger to generate muon triggers. In barrel region, a 3-out-of-4 coincidence of the four layers of the RPC1 and RPC2 is required in low-$p_T$ trigger. For high-$p_T$ trigger, additional 1-out-of-2 coincidence of RPC3 is required. In end-cap, for low-$p_T$ trigger, a 3-out-of-4 coincidence of doublet pairs (TGC2 and TGC3) is required. For high-$p_T$ trigger, additionally, a 2-out-of-3 coincidence of wire planes, and 1-out-of-2 coincidence of strip planes is required. In both TPG and RPC systems latency is about 2.1 $\mu$s, which is within the allowed limit.

The Central Trigger Processor (CTP) [60] receives the trigger information from L1Calo and muon trigger system. These input signals are connected to the input boards of the CTP. Up to 160 of the input signals can be selected (programmable), to use for look-up tables to form the trigger conditions. These trigger conditions are combined to form trigger items, where every trigger condition may contribute to every trigger item, which has a mask, a priority, and a pre-scaling factor. CTP generates the L1A signal by taking a logical OR of all trigger items. Each L1A signal consists of information about the type of trigger and can be used to select the event in the FE electronics and readout chain. CTP also initiates the luminosity block transition, by momentarily pausing the generation of triggers and incrementing the luminosity block number in a register at the CTP decision module. The CTP also provides the clock signal synchronized to the LHC beams. The clock signal is distributed with the L1A to all other sub-systems.

## 2.11  DAQ/HLT

The movement of data from detector to mass storage starts with selection of events by the L1 trigger as shown in the Figure 2.15. During the latency of L1 trigger, the data is buffered in memory located in the FE electronics. On a L1A signal, the event data is

transfered to Data Acquisition System/High-Level Trigger (DAQ/HLT) system from FE in the following data path. The data from FE are transferred to ROD and then to Read Out Buffers (ROB) through Read Out Links (ROL). There are 1,574 ROL's and ROB's in the Read Out System (ROS). The event data are buffered in ROB's to be read by the DAQ/HLT system. The event data consists of RoI information sent over eight ROLs on a dedicated data path. RoI builder uses this information to construct a single data structure which it sends to the L2 supervisor (L2SV). The L2SV forwards the data to one of the L2 trigger processing units (L2PU's) to analyze. The L2PU requests appropriate event data using the RoI information and L2 trigger configuration and sends the analysis to the Data Flow Manager (DFM) through L2SV. If an event does not pass any L2 trigger, the DFM sends a signal to clear the ROB for that event. If the event passes L2 trigger the data is forwarded to the Sub-Farm Input (SFI) for event building. SFI receives the event data through DFM from ROSs and builds the event. The DFM keeps the data rate under the maximum input bandwidth of the SFI, though the SFI can build more than one event at a time.

The SFI forwards the complete event to the EF for further processing and notifies the DFM, which sends a signal to all ROS's to clear the buffers for that event. The EF selects events based on the trigger menu and assigns the events to different streams according to pre-defined criteria.

Selected events are forwarded to the sub-farm output and stored in its local file system according to the classification from the EF. Finally, the events are transferred to CERN's central data-recording facility called Tier 0.

# Chapter 3
# PIXEL DETECTOR AND OPTO-LINKS

## 3.1 Pixel Package Overview

The pixel detector is the innermost element of the ID and is designed to provide at least three space points on a charged track in the range $|\eta| < 2.5$. The pixel system consists of three barrel layers and two identical end-caps, each with three disks. The basic unit of the pixel detector is a module built with silicon sensors, FE electronics, and flex hybrids with control circuits. In general the pixel size is 50 $\mu$m in the $\phi$ direction and 400 $\mu$m in $z/r$ (barrel/disk region), except for a few special pixels. Modules are mounted on mechanical/cooling supports, called staves (sectors), in the barrel (end-cap) regions. The staves are mounted in half-shells manufactured from a carbon fiber composite material. Two half-shells are joined to form a barrel layer. Each disk is built with eight identical sectors.

The barrel shells and the end-cap disks are supported by a space frame also manufactured from a carbon fiber composite material. Electrical, optical, and cooling services are connected and routed within service panels on each end of the pixel detector to the end of the pixel support tube. Electrical, optical and cooling connections are made at the end of the pixel support tube at Patch Panel 1 (PP1). The pixel package, which is built with pixel detector and eight service panels were assembled and tested and then installed as a unit in the ID.

## 3.2  Pixel System Architecture
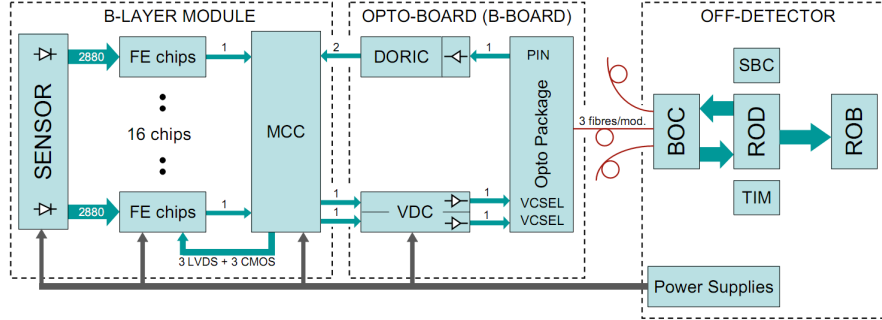


Figure 3.1: Block diagram of the pixel detector system.

As illustrated in the Figure 3.1, pixel sensors are connected to 16 FE chips and those FEs are read out by a Module Control Chip (MCC). Data is transmitted from the FE to the MCC by Low Voltage Differential Signaling (LVDS) serial links, configured in a star topology to get the maximum bandwidth and reliability while keeping the number of data lines to a minimum. Each module is linked to the RODs through optical-fiber links (opto-links), which handle the communication to and from the detector. Basically, the opto-links convert the electrical signals of the module into optical signals and vice versa. The optical-interface card (Back of Crate or BOC) receives/sends signals from/to the opto-links. A combination of commercial and custom components are used for the high and low voltage power supplies. Regulator boards are used to regulate the voltages in the long cables ($\sim 10$ m).

### 3.2.1  Sensors

The pixel sensors have n bulk and n+ implants on the readout side, with the p-n junction on the backside as shown in Figure 3.2 [61]. Pixels are isolated using a moderated p-spray technique [62]. The bulk forms a p-n diode with a backside p+ implant. A multiple guard

36
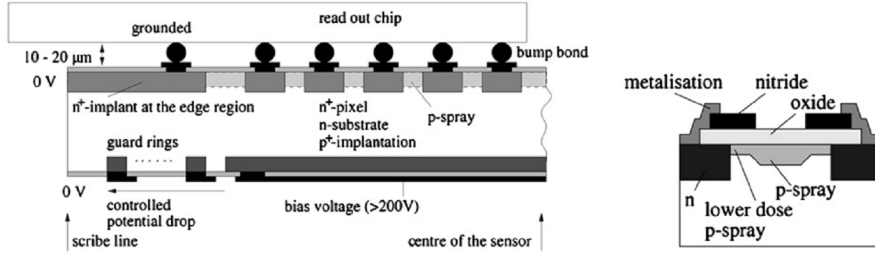
Figure 3.2: Cross-section views of the pixel sensor.

ring structure on the backside of the sensors is designed to withstand a bias voltage in excess of 600 V without breaking down. Oxygenated silicon is used to curb the increase in the depletion voltage due to bulk damage induced by charged particles [63]. Each pixel is DC coupled to the readout electronics on the front side. A bias grid structure using a punch-through connection to each pixel is built to bias the sensor without any electronics to FE chips.

The sensor has an active region of $16.4 \times 60.8$ mm$^2$ and is 250 $\mu$m thick. It contains 41,984 pixels of $50 \times 400$ $\mu$m$^2$ and 5,248 special pixels of $50 \times 600$ $\mu$m$^2$, called long or ganged (two sensor pixels connected to one electronics channel) to cover the inter-chip regions. Two long pixels close the 400 $\mu$m gap between two adjacent FE chips.

### 3.2.2  Pixel FE Chips

A FE chip contains the readout for 2,880 pixels, organized in 18 columns and 160 rows. Each pixel is connected via a bump bond to a charge-sensitive amplifier with leakage current subtraction, signal shaping, programmable threshold discriminator, and Time over Threshold (ToT) output [64]. The ToT provides an 8 bit measurement for the charge amplitude. The ToT response can be adjusted via a DAC controlling the feedback current for each pixel. When a pixel fires, the timestamp and its identifier are stored in a buffer. End of Column (EoC) buffers extract the hit information at a speed of 20 MHz. These timestamps are compared with the trigger timestamp and only hits that match the trigger timestamp plus an adjustable offset are readout.

### 3.2.3  Pixel Modules
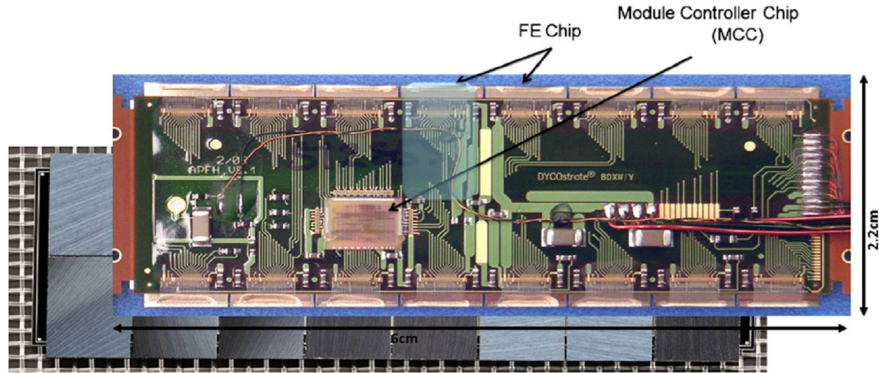


Figure 3.3: A pixel module with its components.

A sensor tile, 16 FE chips and a MCC [37] assembled with a polyimide flex hybrid circuit form a module. A flex cable ("pigtail") attached to the flex hybrid circuit brings signals and power into and out of the module. The module anatomy is illustrated in Figure 3.3. The module temperature is monitored using a 10 k$\Omega$ NTC thermistor on the flex hybrid circuit. The FE chips and MCC are connected to the flex hybrid circuit via 25 $\mu$m Al wire bonds.

The MCC reads data from 16 FE chips simultaneously. First stage event building and basic error handling is performed and communicated to an optical module via LVDS links: clock and one or two data outputs. Data is transferred with respect to the 40 MHz clock. Three different readout speeds are possible: 40, 80, and 160 Mbit/s, dictated by the module occupancy.

### 3.2.4  Pixel Barrels and End-Caps

Pixel modules are mounted in two different configurations; staves built for the barrels and sectors built for the end-caps. Each stave supports 13 modules. Two staves are connected by a cooling U-link to form a bi-stave. The bi-staves were mounted in half-shells. Finally,
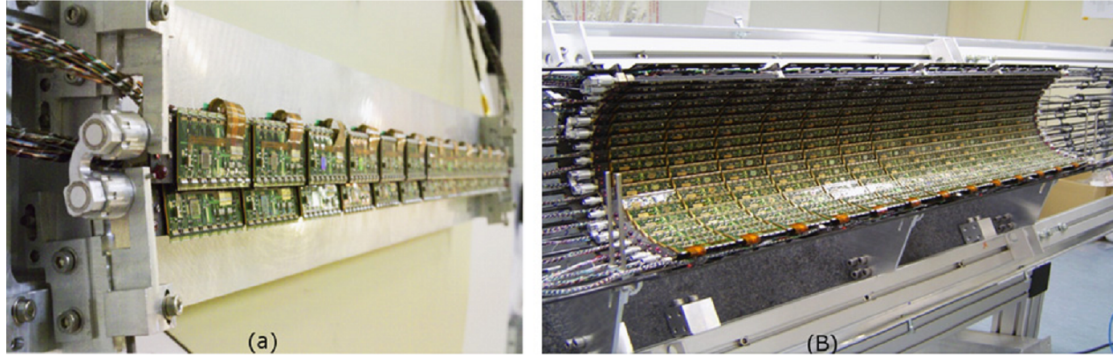
Figure 3.4: A bi-stave instrumented with a cooling U-loop (a) and a half-shell built with bi-staves (b).

two half-shells are clamped to make a barrel as illustrated in Figure 3.4. The end-cap is
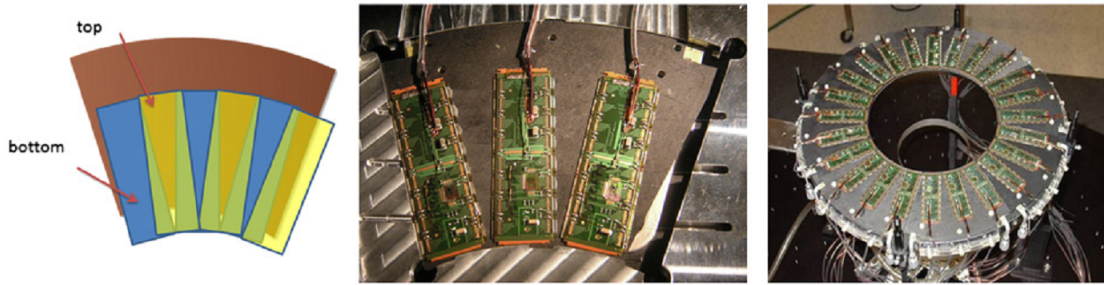


Figure 3.5: The arrangement of modules to built the sectors and finally end-caps.

built from sectors containing 6 modules, 3 glued to each side sandwiching the cooling pipes as shown in Figure 3.5. The barrels use 1,456 modules while the disks are comprised of 288 modules.

### 3.2.5  Pixel Services

The pixel detector needs services such as communication, cooling, and power from the counting room, located ∼100 m away. These services are distributed to each module through

the Service Quarter Panel (SQP), located on both sides of the detector. The only active device on the SQP is the opto-boards, which handles the communication to and from the detector. Basically, the opto-board converts the electrical signals of the module into optical signals to be sent to the control room and vice versa. Optical signals are better suited for transmission over long distances with low noise and little attenuation. Optical transmission also prohibits ground loops. Each opto-board serves 6 or 7 modules, yielding a total of 36 opto-boards per SQP.

### 3.2.6 Opto-boards
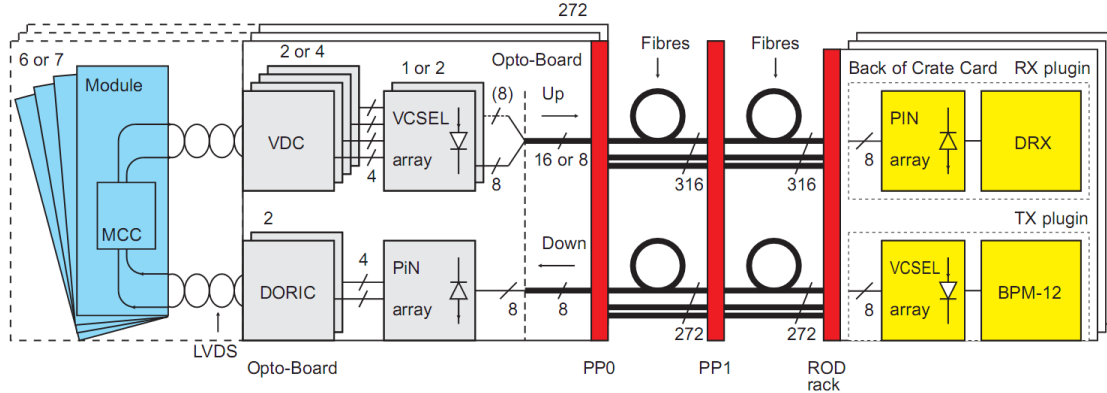


Figure 3.6: Schematic representation of the optical links.

Opto-boards [65] are the electrical-optical converters located at SQP. The communication between a pixel module and an opto-board uses micro-twisted-pair wires. Vertical Cavity Surface Emitting Lasers (VCSEL) controlled by the VCSEL Driver Chip (VDC) on an opto-board convert the data signals to optical signals. The optical signals are transmitted to an RX plug-in mounted on the BOC card. Similarly Bi-Phase Modulated (BPM) clock and data to the module are received by an array of PIN diodes on the opto-board and decoded by a Digital Optical Receiver IC (DORIC). This process is illustrated in Figure 3.6. Opto-boards are fabricated with BeO hybrid for heat management. There are two types

of opto-boards; 228 boards with seven data link per board, serving modules of L1, L2 and disks, and 44 boards with fourteen data links per board for the B layer to accommodate the high hit occupancy.

### 3.2.7  Pixel Readout

The optical fibers from the opto-boards terminate at the RX plug-in mounted on the BOC in the DAQ crate. The RX plug-in converts incoming optical signals back into electrical signals and de-multiplexes the data into 40 Mbit/s streams. The ROD then de-serializes and formats the bit streams. Formatted data is combined with trigger information to form an event fragment. The ROD is equipped with four identical Digital Signal Processors (DSP), each with 256 MB memory to sample and process the event data. During calibration a $5^{th}$ DSP is used to scan parameters and issue calibration.

## 3.3  Major Opto-board Issues

All opto-boards that passed the QA process during the production were required to pass the reception test at CERN before the installation on the service panels. Each opto-board was required to produce good optical power, similar to those observed during the production QA, and a reasonable DAC operating range. After installed on QSP these tests were performed again. The three major problems encountered during these tests are discussed below.

### 3.3.1  Common Serial Resistance

During the reception test it was discovered that some of the VCSELs on the opto-boards produced very little or no optical power on all channels. The optical power on one channel was found to depend on the current on other channels as shown in Figure 3.7 (a). This problem can be modeled with a common resistance as shown in Figure 3.7 (b). The voltage drop on the series resistor results in an inadequate voltage to drive the VCSELs. The only fault that could be identified in the production process of the optical packages was that the thickness of the conductive epoxy under each VCSEL array was $\sim 5~\mu$m, as opposed to the
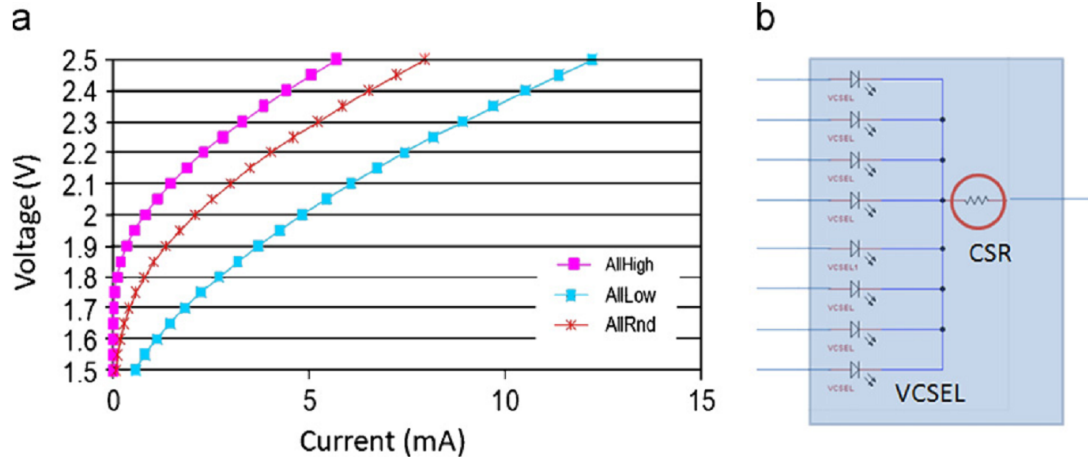
Figure 3.7: Dependence of the IV curve of one VCSEL channel on the currents on the other channels (all low, high, or pseudorandom data) (a) and a model for the CSR in a VCSEL array (b).

$\sim 15~\mu$m as recommended by the manufacturer.

A procedure was formulated to estimate the Common Serial Resistance (CSR) by measuring the current vs. voltage (IV) characteristics of one VCSEL channel with and without current in the other channels. Opto-boards with $> 2.25~\Omega$ of CSR in the VCSELs were rejected, corresponding to $\sim 7~\%$ of total production.

### 3.3.2  Slow Turn On



Figure 3.8: STO behaviors of an VCSEL: no STO (a), mild STO (b), and severe STO (c).

The SCT group discovered that some of their VCSEL arrays took a few ms to produce full optical power after a few ms of inactivity as shown in Figure 3.8. A random sample of opto-boards were tested for Slow Turn On (STO) at the production sites and it was found that there was no indication of the problem until the test was performed on a prototype service panel with the production readout chain. It turned out that this subtle STO behavior depended on the distance between the VCSEL surface and the fiber in a polished MT ferrule. The production fiber with beveled edges on the MT ferrule allowed the fiber to be pushed closer to the VCSEL, picking up transverse modes that might be time dependent. This could explain the STO problem but there is no conclusive proof. Approximately 7 % of the opto-boards with severe STO problem were rejected.

### 3.3.3  Fluctuations in the Optical Power

During the opto-board testing on the QSP, it was discovered that the optical signal had more noise than was observed during the production testing, because of the long electrical cables. These cables allow noise to enter into the VCSEL bias voltage via the VCSEL current control circuitry in the VDC. A bypass capacitor on the bias voltage was purposely not mounted due to the concern that the capacitor might leak after exposure to radiation, rendering the opto-board inoperable. There was no data to support the above concern but the decision was taken because the production test system had no issues with noise without the bypass capacitor. Fortunately, the capacitors could be readily retrofitted and this greatly reduced the fluctuations in the optical power.

## 3.4  Current Status

The fully integrated pixel package was tested for connectivity, before inserting it into the final location at the ATLAS cavern. During the connectivity test, downlinks to the modules were tested by configuring modules and monitoring the increase in current. Uplinks were tested by checking the data lines while opto-board sent back clocks to the BOC. The opto-boards were tuned for RX DAC as a function of timing delay, threshold, and VCSEL control

current. During the connectivity test, no opto-board was found to have high common serial resistance, severe STO or high noise. There was only one dead VCSEL channel out of the 1,788 data links. The most likely cause of this fatality is Electro Static Discharge damage. The link was replaced by moving the (Type 0) cable to a spare channel on another opto-board. There was also one dead PIN channel out of the 1,744 TTC links. The most likely cause of this problem is a cold solder joint on the PIN array. This problem was overcome by moving the cable to an unused channel on another opto-board. Major software changes were needed to use this link. During the connectivity test it was found that one module had a short circuit between VDD and clock, leading to communication problems. Another module had a broken high-voltage wire that was inaccessible for repair. There was one module with a short circuit on one FE chip. The wire bonds of this chip was pulled. So the module now works with 15 FE chips. Most of the faults during the ATLAS data-taking period in 2010 are due to failures of the optical transmitter on the off-detector readout electronics, these can be promptly replaced, and do not result in significant loss of data. Currently 97.2% of the modules are working.

## 3.5  Detector Calibration and Performance

FE electronics thresholds were calibrated by injecting signals of known amplitude into the electronics input. Figure 3.9 shows nominal working point with a threshold of 4000 e [66]. The intrinsic hit efficiency was measured [67] in cosmic-ray events by extrapolating tracks through the detector and counting the number of measurements on a track. The measured hit efficiency was (99.974 ± 0.004 (stat.) ± 0.003 (syst.))% for the barrel, after the non-operational modules are excluded.

The residuals with respect to the track extrapolation for the $x-y$ position of the clusters provides a good measurement of detector resolution. Figure 3.10 [68] shows the values of RMS of the residuals as a function of the track incident angle and pseudo-rapidity. The spatial resolution is improved by using a charge sharing algorithm as expected.
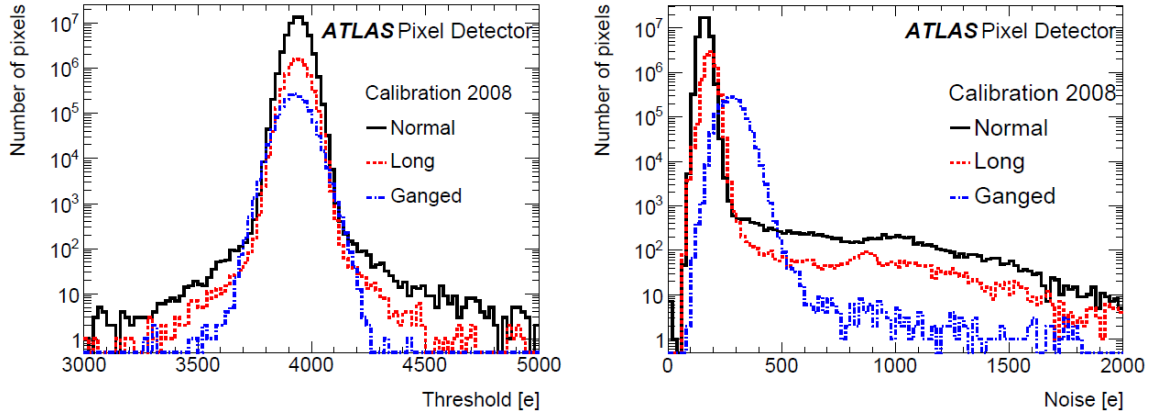
Figure 3.9: Pixel Detector threshold (left) and noise (right) distributions from calibrations based on charge injection.
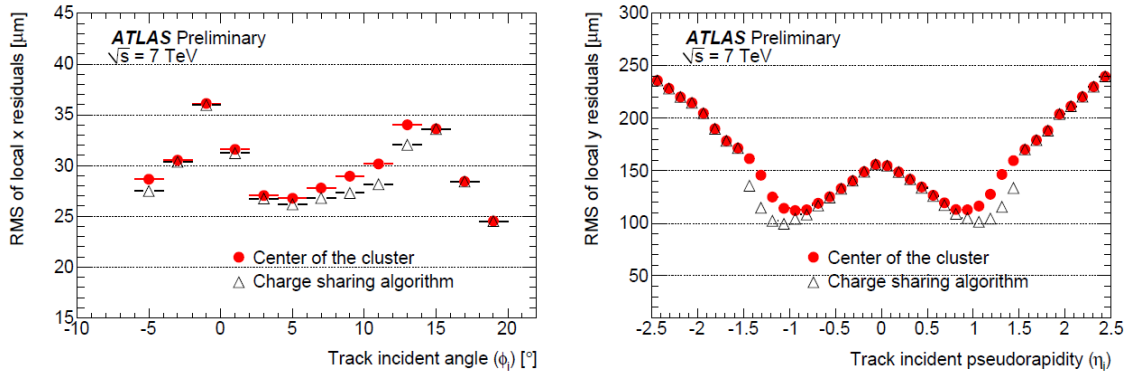


Figure 3.10: Distributions of RMS of the residuals as a function of the track incident angle (left) and pseudo-rapidity (right).

# Chapter 4

# EVENT SIMULATION WITH MONTE CARLO EVENT GENERATORS

## 4.1  Introduction

Particle interactions are described by probability distributions. As a result Monte Carlo (MC) methods are useful in simulating process occurring in high energy physics experiments. There are two main types of simulations used in particle physics: event generators and detector simulations. The event generators are used to simulate the physics of the collisions. They generate the 4-momenta of initial, intermediate, and final state particles. Detector simulations are used to simulate the interactions of the particles with the detector. A model of the full detector with all material (including inactive material) is used in this simulation and detector parameters such as vertex resolution and acceptance are derived from the detector model.

Since event generators can be programmed to simulate any theory of particle interactions, this method is used to predict the rate and topology of a given theoretical process which, after being passed through the detector simulations, can be compared with real data. As such, detector simulations are very useful in tuning analysis algorithms.

## 4.2  Event Generators

There are 40 different MC event generators used in ATLAS analysis [69]; some of them are versatile and some are specialized. Simulation of an event can be categorized into three

steps as illustrated in the Figure 4.1:
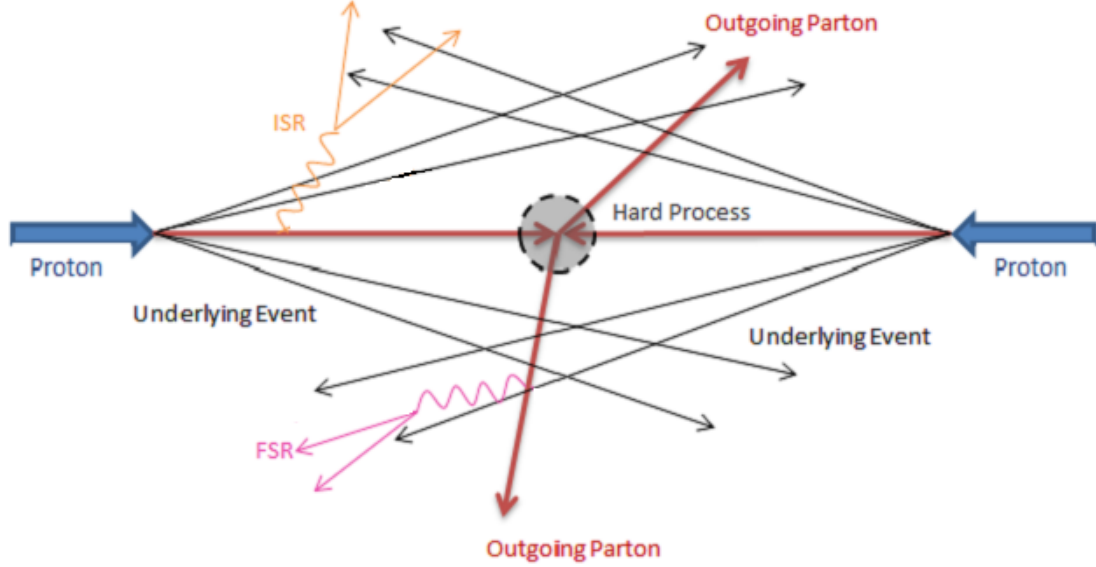


Figure 4.1: Steps of simulation process.

- the elementary hard process, where the hard partons of the incoming protons interact and produce the outgoing particles,

- the Initial State Radiation (ISR) and Final State Radiation (FSR), and

- the underlying event (non-scattering fragments of the two incoming protons) and the hardronization of final state partons.

Generators can be grouped into four categories according to which steps they handle. The first group consists of full generators such as Pythia [70], Herwig [71], and Sherpa [72] that handle all three steps. The second group is composed of add-on packages, mainly used for FSR, such as Tauola [73], Phojet [74], and Photos [75]. The third group includes add-on packages specialized for modeling the underlying event such as Jimmy [76]. The final group of generators is composed of add-on packages specially designed to handle the elementary hard process, such as MC@NLO [77], Alpgen [78], and MadGraph [79].

## 4.3 Event Simulation at ATLAS

### 4.3.1 Athena, the ATLAS Framework

Athena is a control framework consisting of an application manager, services, and algorithms
as shown in the Figure 4.2. The input data is manipulated by the user defined algorithm,
while services provide facilities, such as printing, massaging, and histogramming, for the
algorithm. For example, the configurations for the event generation algorithm are defined
through the Job Options (JO) service.
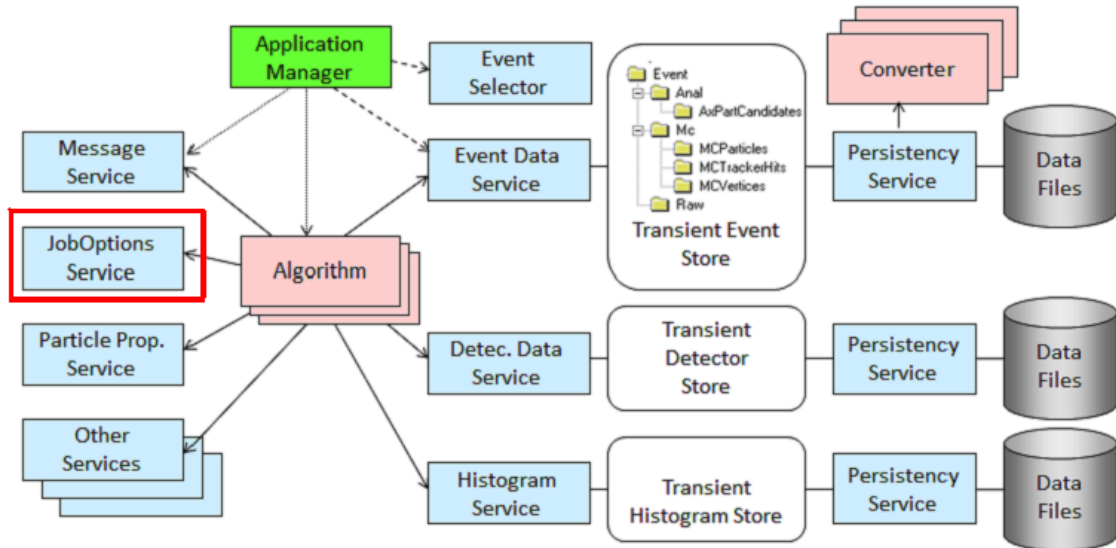


Figure 4.2: Athena architecture.

### 4.3.2 Integrations of External Generators in Athena

The different MC generators used by ATLAS are developed independently elsewhere and the
generator support group [80] at the LHC provides a validated unified interface to ATLAS
software. The interface workflow is illustrated in Figure 4.3.

Users pass Athena parameters, such as output location, and generator specific settings,
such as decay channels, through JO scripts. The generators, which are also specified in the
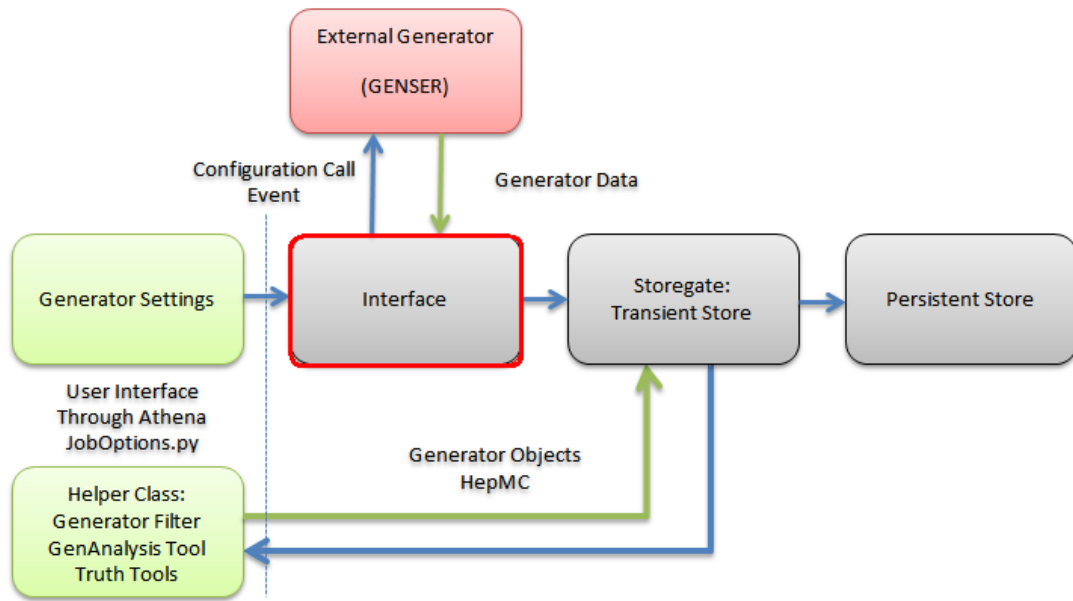
Figure 4.3: Workflow of MC generation in Athena.

JO, are configured during the initialization of the job; during the event loop (when the list of algorithms run sequentially on each event) the generators send each generated event back to the interface. The event is then saved in the Storegate, where the C++ objects are stored, in HepMC [81] format. The helper services, such as Generator Filters and Truth Tools, get the event from the Storegate, modify it and return it to the Storegate. For example, one can filter events based on the number of leptons in the event and write them back to the Storegate. Finally, the events in the Storegate are saved to a ROOT file on a physical disk.

### 4.3.3   ATLAS Simulation with GEANT4

A detailed simulation of the detector has been implemented to study detector response for a wide range of physics processes using the GEANT4 simulation tool kit [82] within the Athena framework. The simulation takes the generated events, simulates passing them through the detector, and outputs a ROOT file identical to the real detector output. There are two main steps in the detector simulation process: simulation of the interactions of particles within

the detector, and digitization of the interactions into currents and voltages. After both steps are complete, the digitized output will go through the same trigger reconstruction algorithms as real data.

The stable particles in the event generation output are read into GEANT4 and propagated through the ATLAS detector. Detector elements get energy depositions that are recorded in hits files. The hits file entries include information such as energy deposited, position, and time. The digitization takes the hits file, adds random noise, simulates triggers, and sends digital output to a simulated ROD, which writes the simulated event to a Raw Data Output (RDO) ROOT file.

The physical description of the detector and the conditions of the environment used by GEANT4 are read from the geometry and conditions databases. This allows users to test detector misalignments.

### 4.3.4  Job Transformations

To keep the simulation process well defined and reproducible, a set of Python scripts are maintained by Computer System Commissioning (CSC) to take conditions globally and construct the events, one for generation of events and another for simulation.

## 4.4  Generation of $Z \to e\mu$ Signal MC

Since the decay of a $Z$ boson directly to one electron and one muon violates electron and muon flavor conservations, it is not one of the standard decay channels defined in the Pythia generator [70] and prior to this analysis was not in the ATLAS MC central production list. To perform this analysis it was essential to get a signal MC dataset. The $Z$ is generated in the standard process, but after decaying to a lepton pair, the flavor of one lepton is switched to the other flavor. To increase the efficiency, a generator level filter was implemented requiring at least two leptons, inside the detector ($|\eta| < 2.8$), with at least 5 GeV/c of transverse momentum. Pythia's native QED FSR and tau decay simulations are disabled and replaced with those of Photos and Tauola, for greater accuracy. This

production process has been validated and included in the ATLAS standard MC generation
pool from beginning 2010.

## 4.5  Validation of $Z \to e\mu$ Dataset

To validate this MC dataset, a comparison was done with the standard $Z \to ee$ and $Z \to \mu\mu$
datasets produced by ATLAS official MC production. The distributions of $p_T$, $\eta$, $\phi$, and
the invariant mass of leptons from the $Z$ bosons were compared before being sent through
the detector simulation (i.e. using truth level information) in Figure 4.4. All distributions
of $Z \to e\mu$ agree with $Z \to \mu\mu$ and $Z \to ee$.
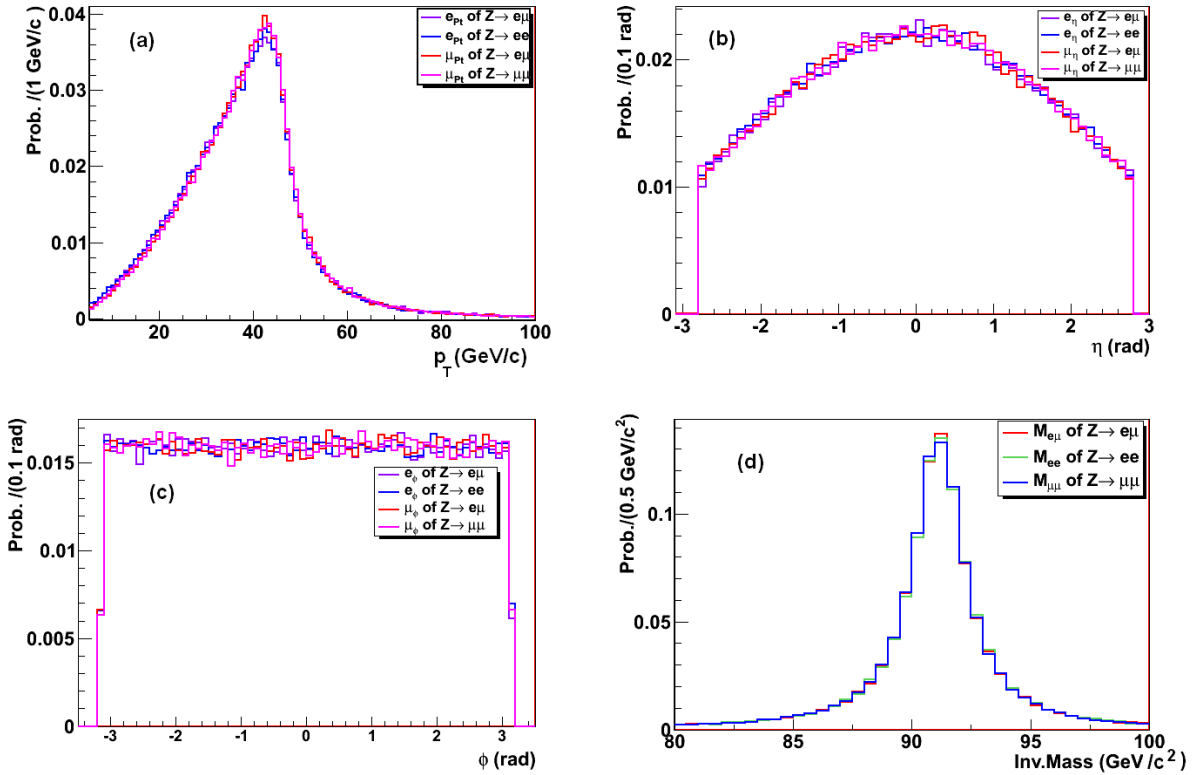


Figure 4.4: Comparison of various kinematic distributions, $p_T$ (a), $\eta$ (b), $\phi$ (c), and invariant
mass spectra of the lepton pair (d) in $Z \to ee$, $\mu\mu$, and $e\mu$. The area of all distributions
has been normalized to one.

# Chapter 5

# Event Reconstruction and Particle Identification

## 5.1 Introduction

Raw data from various subsystems of the ATLAS detector (Chapter 3) are recorded at CERN's central data-recording facility (tier 0) in the RDO format. However, the RDO data format is not convenient for analysis, because it is very large. In addition to data it stores status of each detector elements (i.e. voltages, currents, etc.). This data has to be processed with special reconstruction software within Athena to ensure that the same code is being executed during development, validation, and production. This software reconstructs physics objects such as tracks, vertices, photons, electrons, muons, jets, and missing transverse energy, and saves them in Analysis Object Data (AOD) format.

## 5.2 Track Reconstruction

The ATLAS ID track reconstruction software is designed to use data from both the ID and the muon spectrometer to reconstruct tracks [83]. The software has a modular and flexible design, following the common event data model [84] and detector description. This design creates standard interfaces to all reconstruction tools, such as track extrapolation, track and vertex fitting, and material corrections.

ATLAS track reconstruction can be divided into three stages: pre-processing, track finding, and post-processing [85]. During the pre-processing stage, clusters are constructed

from the pixel and SCT detectors and calibrated drift circles are built from the TRT data. At the track finding stage, by using a combination of space-points in the three pixel layers and the first SCT layer, the track seeds are built. These seeds are then extended throughout the SCT to form track candidates. Next, these candidates are fitted with the other SCT layer hits. Outlying clusters and fake tracks are rejected by applying quality cuts. The selected track candidates are then extended into the TRT and associated with drift-circle information. These extended track candidates are then refitted using the hits in all three tracking subsystems to get the tracks. The refitted track quality is compared to the silicon-only track candidates and hits on track extensions. The outlying hits are labelled and kept as part of the track but are removed from the fit. To improve the tracking efficiency for the tracks from the decays of long-lived particles, unused track segments in the TRT are extended into the SCT and pixel detectors. During the post-processing stage, the primary/secondary vertices and photon conversions are reconstructed.

### 5.2.1  Track parameter resolutions

In a magnetic field a track can be described by five track parameters; inverse transverse momentum $(q/p_T)$, azimuthal angle $(\phi)$, polar angle $(\cot\theta)$, transverse impact parameter $(d_0)$, and longitudinal impact parameter $(z_0 \times \sin\theta)$. The expected resolution of the track parameters was originally measured using reconstructed and split tracks from cosmic ray data [86]. Since cosmic showers mostly go through the detector from top to bottom, any track parameter associated from top split $(X_{top})$ and bottom split $(X_{bottom})$ can be compared. Since both of those from the same particle, the variance of the difference $\sigma^2(X_{\tau,top} - X_{\tau,bottom})$ should be twice the $\sigma^2(X_\tau)$ of each track. This method is used [86] to measure the track parameter resolution. Track selection was made by requiring minimum transverse momentum of 1 GeV/c and have at least 2, 6, and 25 hits in the pixel, SCT, and TRT with impact parameter less than 40 mm. The measured resolution was compared with the MC expectation of a perfectly aligned detector. Figures 5.1 shows the transverse and longitudinal impact parameter resolution measured from cosmic data as a function of transverse momentum. The difference in the performance is due to the remaining misalignments. Table 5.1 [86]
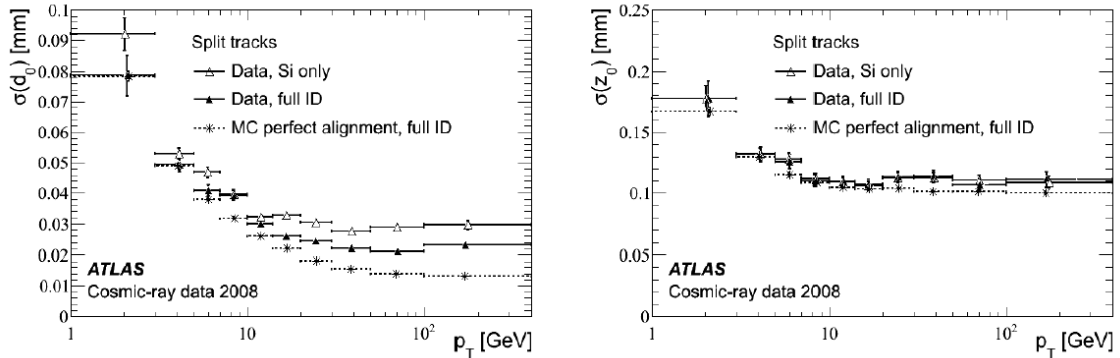
Figure 5.1: Transverse (left) and longitudinal(right) impact parameter resolution measured from cosmic data as a function of transverse momentum.

| Parameter | Cosmic-ray | MC |
|:---:|:---:|:---:|
| $d_0$ ($\mu$m) | $22.1 \pm 0.9$ | $14.3 \pm 0.2$ |
| $z_0$ ($\mu$m) | $112 \pm 4$ | $101 \pm 1$ |
| $\phi_0$ (mrad) | $0.147 \pm 0.006$ | $0.115 \pm 0.001$ |
| $\theta$ (mrad) | $0.88 \pm 0.03$ | $0.794 \pm 0.006$ |

Table 5.1: Comparison of track parameter resolution between cosmic-ray data and MC.

shows a summary of the track-parameter resolutions for tracks with $p_T > 30$ GeV/c, where the multiple-scattering contribution is negligible.

## 5.3  Muon Reconstruction and Identification

### 5.3.1  Introduction

Muon identification and reconstruction in ATLAS is performed using three methods. The first method is finding tracks from the muon spectrometer and extrapolating to the beam line; these are called standalone muons. The second method is matching spectrometer tracks with ID tracks and combining the measurements of the two systems. Muons identified by this method are called combined muons. The third method is finding muons by extrapolating ID tracks to the muon spectrometer and searching for nearby hits. The muons found by this method are called tagged. There are two families of algorithms called Statistical

54

Correlations (StaCo) and Muon Identification (MuId). One algorithm from each method is included in each family in the current ATLAS standard reconstruction system. The current default for physics analysis is the StaCo family of algorithms.

### 5.3.2 Standalone Muons

The standalone algorithms start building track segments in muon stations and then link the segments to form tracks without using the inner tracker information. As noted above the two algorithms implemented with this method are called Muonboy (StaCo family) and Moore (MuId family). The main advantage of a standalone algorithm is the slightly greater pseudo-rapidity coverage ($|\eta| < 2.7$ compared to 2.5). This is due to limitation of the ID coverage needed for the other algorithms. The former algorithm allows the reconstruction of a muon produced in the decay of a particle as it passes through the ID (as in a $K^+$ decay).

### 5.3.3 Combined Muons

Combined muon algorithms match muon-spectrometer tracks with ID tracks to identify muons. The match $\chi^2$, defined as the difference between outer and inner track momentum vectors weighted by their combined covariance matrix, is used to measure the quality of this match [85]. A statistical combination of the inner and outer track vectors are used by the StaCo algorithm to obtain the combined track vector. In contrast, the MuId algorithm starts from the inner track vector and adds the measurements from the outer track to obtain the combined track vector.

### 5.3.4 Tagged Muons

MuTag (StaCo family) and MuGirl (MuId family) are the two algorithms implemented for finding the tagged muons. In both algorithms, all ID tracks with a momentum of 1 GeV/c or higher are extrapolated to the first station of the muon spectrometer where nearby hits are located. MuTag uses the $\chi^2$ value calculated from the difference between the nearby hit and extrapolated track to identify the muons. MuGirl uses an artificial neural network

for this purpose. Both algorithms use the ID only for the measurements (in contrast with combined muon algorithms).

### 5.3.5 Muon Reconstruction Performance

The performance of the muon reconstruction was studied [87, 88] using early $\sqrt{s} = 7$ TeV data. Position of the track in the bending plane in the muon spectrometer is calculated using the MDT and CSC hits. The distributions of the number of MDT and CSC hits are shown in Figure 5.2. MC simulation and data are in a reasonable agreement except tracks with large number of CSC hits, which is expected to be resolved with better alignment. Figure
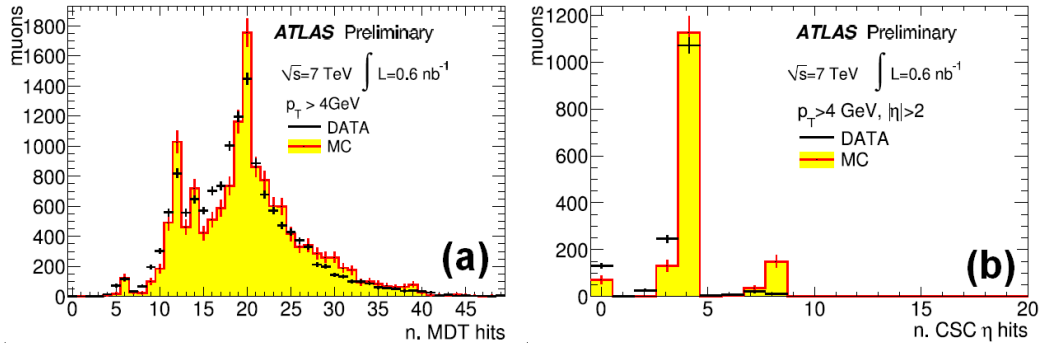


Figure 5.2: Comparison of the measured distributions of the number of MDT (a) and CSC hits (b) in the bending plane on the combined muon tracks with early $\sqrt{s} = 7$ TeV ATLAS data to the MC predictions.

5.3 shows the expected muon $p_T$ resolutions as functions of $\eta$ and $p_T$ [85]. Momentum resolution of $\lesssim 2$ (3.5)% is expected for the barrel (end-cap) [85].

## 5.4 Electron and Photon Reconstruction and Identification

### 5.4.1 Introduction

The first step in electron and photon reconstruction [85] is forming clusters. In ATLAS this is performed by a sliding window algorithm [89]. The algorithm forms fixed size rectangular
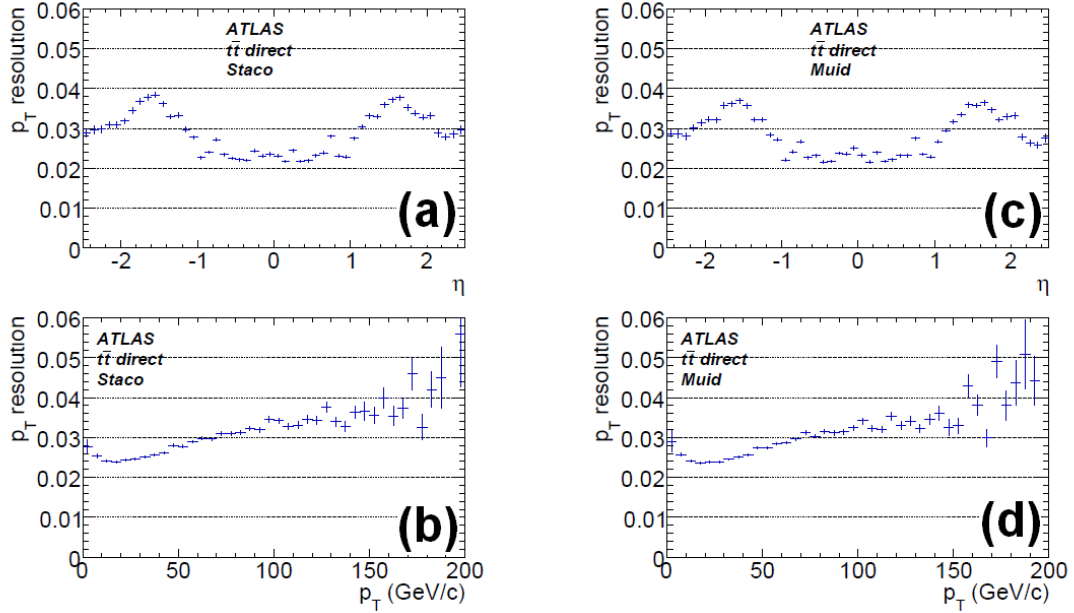
Figure 5.3: MC prediction for the fractional momentum resolution for StaCo muons as a function of $\eta$ (a) and p$_T$ (b). (c) and (d) shows the corresponding distributions for MuId muons.

clusters, positioned to maximize the amount of energy within the cluster. The reconstruction tries to find a matching track within a $\Delta\eta \times \Delta\phi$ window of $0.05 \times 0.10$ around the center of the cluster with $E/p < 10$. If a track is found, the algorithm checks for the presence of any photon conversions. If no conversion is found, an electron candidate is created; otherwise, a photon candidate is created. After this classification, $\eta$ and $\phi$ parameters are corrected (due to finite granularity and energy sharing between cells) and the identification refined based on shower shapes. Finally, five levels of electron/photon quality are defined (loose, medium, medium isolated, tight, and tight isolated) for use in physics analysis.

### 5.4.2 Algorithms

There are two electron reconstruction algorithms implemented in ATLAS offline software. The standard algorithm starts from clusters reconstructed in the calorimeters and builds the electron object based on the data from the ID and the calorimeters. This algorithm is optimized for high energy electrons ($E_T \gtrsim 20$ GeV). The second algorithm starts from the

| Particle | Source |
|---|---|
| Prompt Electron | $Z, W$ |
| Non-prompt Electron | Heavy flavor quark |
| Non-Electron | $\gamma,\ \pi^{\pm},\ k^{\pm},\ \rho^{\pm}$ |

Table 5.2: Origins of electron candidates.

ID tracks and matches the isolated energy depositions in the electromagnetic calorimeters. This algorithm is optimized for low energy electrons with quality tracks ($E_T \approx 2$ GeV). If an electron is found with the first algorithm, the author of that is set to 1. If it is found from the second, the author is set to 2. If both algorithms found it, the author is set to 3.

### 5.4.3  Electron Candidates

The set of reconstructed electron candidates usually consists of a wide range of particles, but is dominated by charged particles from heavy quark decays as summarized in Table 5.2.

### 5.4.4  Electron Quality

Standard identification of electrons from electron candidates is based on 28 tests, which can be applied independently. These tests are defined based on electromagnetic shower shapes, track quality, and isolation. They are divided into seven bins in $\eta$ and six bins in $p_T$. The results of these tests are combined into a 28-bit variable called IsEM. The highest quality electrons (i.e. those that pass all tests) have IsEM $= 0$. In order to simplify the use of this variable, five reference sets of results have been defined: loose, medium, medium isolated, tight, and tight isolated. This provides flexibility in defining an analysis algorithm, or desired cleanness of the signal.

### 5.4.5  Loose Electrons

The selection criteria are designed to have high identification efficiency, without robust background rejection. It is based on limited information from the calorimeters such as lateral shower shape, lateral shower width, and hadronic leakage. The selection criteria are summarized in Table 5.3.

| Variable | Description |
|---|---|
| Acceptance | $|\eta|$ |
| Hadronic leakage | Ratio of $E_T$ in the first sampling of the hadronic calorimeter to $E_T$ in the EM cluster |
| Shower shape in second layer of EM calorimeter | Ratio in $\eta$ of cell energies in $3 \times 7$ versus $7 \times 7$ cells |
|  | Ratio in $\phi$ of cell energies in $3 \times 3$ versus $3 \times 7$ cells |
|  | Lateral width of the shower |

Table 5.3: Selection criteria for a low quality electron ("Loose").

| Type | Description |
|---|---|
| Shower shape in the first layer of EM calorimeter | Difference between energy associated with the second largest energy deposit and the minimal of first and second maxima |
|  | Second largest energy deposit normalised to the cluster energy |
|  | Total shower width |
|  | Shower width for three strips around maximum strip |
|  | Fraction of energy outside core of three central strips but within seven strips |
| Track quality | Number of hits in the pixel detector ($> 1$) |
|  | Number of hits in the pixel and SCT ($> 1$) |
|  | Transverse impact parameter ($< 1$ mm) |

Table 5.4: Additional selection criteria for a medium quality electron ("Medium").

## 5.4.6 Medium Electrons

Additional selection criteria are imposed to improve the electron quality using the information from strips in the first layer of the EM calorimeter and from the tracking system as summarized in Table 5.4. Strip-based cuts are designed to reject photons from $\pi^0$ decays. The tracking variables include the number of hits in the pixel detector, the number of silicon hits (pixel plus SCT), and the tranverse impact parameter. These selection criteria have significantly higher jet/photon rejection efficiency compared to the "loose" electrons. Two different versions are available within this category, optimized for isolated and non-isolated electrons.

| Type | Description |
|---|---|
| Vertexing-layer | Number of hits in the vertexing-layer ($> 1$) |
| Track matching | $\Delta\eta$ between the cluster and track |
| | $\Delta\phi$ between the cluster and track |
| | Ratio of the cluster energy to the track momentum |
| TRT | Total number of hits in the TRT |
| | Ratio of the number of high-threshold hits to the total number of hits in the TRT |
| Isolation | Ratio of transverse energy in a cone $\Delta R < 0.2$ to the total cluster transverse energy |

Table 5.5: Additional selection criteria for a high quality electron ("tight").

## 5.4.7  Tight Electrons

Further selection criteria are imposed by using all available information to identify electrons as summarized in Table 5.5. To reject electrons from conversions, the number of hits in the vertexing layer and TRT is used. To reject charged hadrons, the ratio of high threshold hits to the number of hits in the TRT is used. Two different versions are also available within this category, optimised for isolated and non-isolated electrons.

## 5.4.8  Electron Identification Performance

Although there are some performance measurements related to identifying electrons using cosmic ray and early 7 TeV data, the official performance studies based on 7 TeV data are not yet released. Hence, initial ATLAS electron identification performance results are based on MC simulated events [85]. Performance of the electron quality selection criteria in terms of efficiency and QCD jet rejection is shown in Tables 5.6 and 5.7 for electrons with $E_T$ > 17 GeV and 8 GeV respectively [85]. In this study electrons from both reconstruction algorithms (see Section 5.4.2) were used. It is evident that an exceptionally clean inclusive electron sample can be obtained with tight selection criteria.

| Quality | Prompt (%) | $b, c \rightarrow e$ (%) | Jet rejection |
|---|---|---|---|
| Loose | $87.96 \pm 0.07$ | $50.8 \pm 0.5$ | $567 \pm 1$ |
| Medium | $77.29 \pm 0.06$ | $30.7 \pm 0.5$ | $2184 \pm 13$ |
| Tight (TRT) | $61.66 \pm 0.07$ | $22.5 \pm 0.4$ | $(8.9 \pm 0.3) \times 10^4$ |
| Tight (isol.) | $64.22 \pm 0.07$ | $13.7 \pm 0.4$ | $(9.8 \pm 0.4) \times 10^4$ |

Table 5.6: Efficiencies and jet background rejections for four standard electron qualities with $E_T > 17$ GeV. These values were estimated using simulated di-jet and minimum-bias samples.

| Quality | Prompt (%) | $b, c \rightarrow e$ (%) | Jet rejection |
|---|---|---|---|
| Loose | $75.8 \pm 0.1$ | $55.8 \pm 0.7$ | $513 \pm 2$ |
| Medium | $64.8 \pm 0.1$ | $41.9 \pm 0.7$ | $1288 \pm 10$ |
| Tight (TRT) | $46.2 \pm 0.1$ | $29.2 \pm 0.6$ | $(6.5 \pm 0.3) \times 10^4$ |
| Tight (isol.) | $48.5 \pm 0.1$ | $28.0 \pm 0.6$ | $(5.8 \pm 0.4) \times 10^4$ |

Table 5.7: Efficiencies and jet background rejections for four standard electron qualities when $E_T > 8$ GeV. These values were estimated using simulated di-jet and minimum-bias samples.

## 5.5 Jets and Missing Transverse Energy

### 5.5.1 Introduction

Jet and Missing Transverse Energy ($E_T^{miss}$) reconstruction are important for most physics analyses being performed in the ATLAS experiment. This is because high quality and highly efficient jet reconstruction is necessary for a complete understanding in the physics of the hadronic final states.

### 5.5.2 Jet Algorithms

As shown in Figure 5.4, a jet is a collection of hadrons and other particles produced in the hadronization of a quark or gluon, due to QCD confinement. The kinematic properties of these jets $(p_T, \eta, \phi)$ are correlated with the kinematic properties of the original partons. A jet algorithm defines how particles in the detector are grouped into jets.

There is no universal jet reconstruction algorithm for the hadronic final state in all possible interesting topologies. Since ATLAS is built to reconstruct a wide range of different
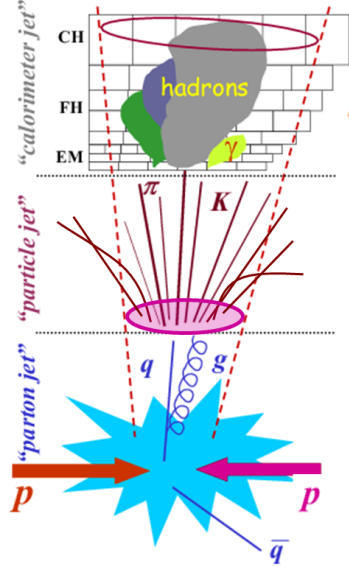
Figure 5.4: Evolution of a jet.

types of physical signatures, all of the relevant jet reconstruction algorithms are implemented in ATLAS offline reconstruction. There are three main types of jet reconstruction algorithms: fixed sized cone algorithms, sequential recombination algorithms, and event shape analysis algorithms.

Cone Algorithms begin by making a list of proto-jets from the hits in calorimeters (usually above some seed energy): starting with the highest energy seed they draw a cone of radius $R$ around the seed, then calculate the $E_T$ weighted centroid of the cone. Next, the algorithm draws a new cone of radius $R$ around the calculated centroid. This process iterates until the centroid of the cone converges to a fixed point; at this point the cone is considered a jet candidate. This procedure repeats for all of the proto-jets that are not in a existing jet. Finally, the jets that overlap are split or merged depending on the final structure.

There are two sequential recombination jet finder algorithms implemented in ATLAS: $k_T$ and anti-$k_T$. The $k_T$ algorithms start with a list of pre-clusters. For each pre-cluster $i$, they define $d_i = P_{T,i}^2$. Then, for each pair $(i, j)$ of pre-clusters they analyze the relative transverse momentum squared, defined by: $d_{i,j} = min(P_{T,i}^2, P_{T,j}^2)\frac{\Delta R_{i,j}^2}{R^2}$. Here, $\Delta R_{i,j}^2 = \Delta\eta_{i,j}^2 + \Delta\phi_{i,j}^2$

62

and $R$ is a free parameter. For each pre-clusters pair $(i, j)$, the minimum of $d_{ij}$ and $d_i$ is found. If the minimum is a $d_{i,j}$, the cluster pair $(i, j)$ combined into a new object by adding their four-momenta. Both pre-clusters are removed from the list, and the new combined pre-cluster is added to the list. If the minimum is from a $d_i$, the pre-cluster is considered as a jet candidate and removed from the list. This procedure is repeated until all objects are removed from the list. At this point all pre-clusters are either part or all of a jet candidate. The free distance parameter, $R$, allows some control on the size of the jets. ATLAS reconstruction is performed with two values: $R = 0.4$ for narrow jets and $R = 0.6$ for wide jets. The only difference in anti-$k_T$ algorithms is that the pre-clusters are analyzed with respect to the *inverse* of the relative transverse momentum squared, i.e. $d_i = \frac{1}{P_{T,i}^2}$ and $d_{i,j} = min\{\frac{1}{P_{T,i}^2}, \frac{1}{P_{T,j}^2}\}\frac{\Delta R_{i,j}^2}{D^2}$.

ATLAS uses two primary inputs for jet reconstruction algorithms: topological clusters and towers. To form topological clusters, a group of calorimeter cells is topologically inter-connected and selected by energy significance. To form reconstructed cluster towers, thin radial sections of the calorimeters of fixed geometry $0.1 \times 0.1$ in $\eta \times \phi$, containing only cells with significant signal are identified.

ATLAS uses anti-$k_T$, recombination scheme, with $R = 0.4$ or $0.6$ algorithms. It should be noted that $R = 0.4$ is required to resolve jets from top decays [85].

### 5.5.3 $E_T^{miss}$ Reconstruction Algorithms

Missing transverse energy ($E_T^{miss}$) indicates the presence of neutrinos or other non inter-acting particles carrying off energy. Reconstruction of $E_T^{miss}$ is a real challenge for ATLAS since underlying events, multiple interactions, pile-up, and coherent electronics noise pro-duce imbalanced transverse energy in the calorimeters and muon spectrometer, which are the main detector elements used for $E_T^{miss}$ reconstruction. The loss of energy in dead re-gions and readout channels cause further imbalances. There are two $E_T^{miss}$ reconstruction algorithms in ATLAS, built with different methods of energy classification and calibration. One of them is based on cells and the other is based on reconstructed objects.

The cell based method starts from the energy deposits in calorimeter cells that survive

a noise suppression procedure [90]. All calorimeter cells are calibrated based on the cell energy density and position. Corrections are applied for the muon energy and energy lost in the cryostat i.e.

$$-E_T^{miss} = \sum E_{T(x,y)}^{cell} + \sum E_{T(x,y)}^{muon} + \sum E_{T(x,y)}^{cryo}. \qquad (5.1)$$

The object-based algorithm starts from the reconstructed and calibrated objects in the event (i.e. electrons, muons, jets, etc.). Corrections are applied for the energy outside these objects, which is classified as low $p_T$ deposit from charged and neutral pions. In this approach the $E_T^{miss}$ is obtained from:

$$-E_T^{miss} = \sum E_{T(x,y)}^{high\,E_T\,objects} + \sum E_{T(x,y)}^{low\,E_T\,objects}. \qquad (5.2)$$

# Chapter 6

# ATLAS Data Analysis Model and Tools

## 6.1 Introduction

The ATLAS experiment is designed to record, reconstruct, and analyze more than $10^9$ events per year. For this purpose, the computing structure is built based on a multi-level, hierarchically distributed computing and storage model similar to the Open Science Grid (OSG) [91]. Initial event reconstruction and detector calibration takes place at the tier 0 facility at CERN using raw data. Reconstruction jobs produce datasets in the AOD format, suitable for physics analysis. These datasets are distributed to 11 tier 1 facilities throughout the world. There are several smaller tier 2 sites, associated with each tier 1. Tier 3 centers, built at many universities, are designed primarily for end-user analysis. For physics analysis, AOD files are converted to Derived Physics Data (DPD). DPDs contain only the objects and events needed for a particular type of physics analysis to reduce storage requirements and increase processing speed.

## 6.2 Signature Based ntuples

There are different types of DPD, distinguished by the degree of change in the format. The first two levels can not be read without a full Athena installation. The third level of ATLAS analysis output, D3PD, is readable through a standalone ROOT installation (without additional libraries). This is ideally suited for physics analysis at the end user

65

level. In D3PDs almost all of the objects (electron, jet, truth, track, etc.) are stored as collections, called containers. When an analysis program is run on these datasets, it needs to read all of the objects in the container, including objects not needed for the specific analysis. Unfortunately, some of the important add-on packages like the Tool Kit for Multivariate Analysis (TMVA) [92] does not support this data structure. Furthermore, in a typical ATLAS data analysis, large MC background samples are needed, which is resource intensive. To solve these issues, another level of DPD was created called the D4PD. The initial code that was written to make D4PDs used in this analysis are being converted for general use.

D4PD maker has three major functions. First D4PD maker algorithm checks the trigger for particular data streams and signatures. Then it checks for the presence of different signatures (e.g. di-electron or electron-muon) using only objects that satisfy some pre-selection criteria (e.g. "tight" electron identification). During this process, D4PD algorithm checks for any overlaps between the objects and removes the overlapping objects. Finally selected events are saved in different root trees by signature with all the information associated with the objects that compose the signature. During this process, the properties of the combined object, such as the invariant mass and the angle between the objects is calculated. This method replaces containers in each event (one per event) with several entries in the tree, one for each possible instance of the signature in the event which can be further analyzed. Since ROOT loads only the trees that the analysis algorithm requests, having many trees improves the performance because only the relevant signature are loaded saving memory. D4PDs are being made at The Ohio State University (OSU) for use in many diverse analyses and may be used by the other groups in the future.

## 6.3 Performance

The average file size and speed of processing the AODs, D3PDs, and D4PDs has been tested for many different MC and 7 TeV ATLAS datasets. For this test, the same analysis built on both Athena and ROOT as well as the same computer were used to analyzed them. The results are summarized in Table 6.1. The performance of the Athena based analysis using

| File Type | Event size (kB/event) | Processing speed (events/sec) |
|-----------|-----------------------|-------------------------------|
| AOD       | 180                   | 6                             |
| D3PD      | 45                    | 800                           |
| D4PD      | 0.7                   | 20000                         |

Table 6.1: Processing speed and file size for different data types.

computers with multiple processing cores are summarized in Figure 6.1.
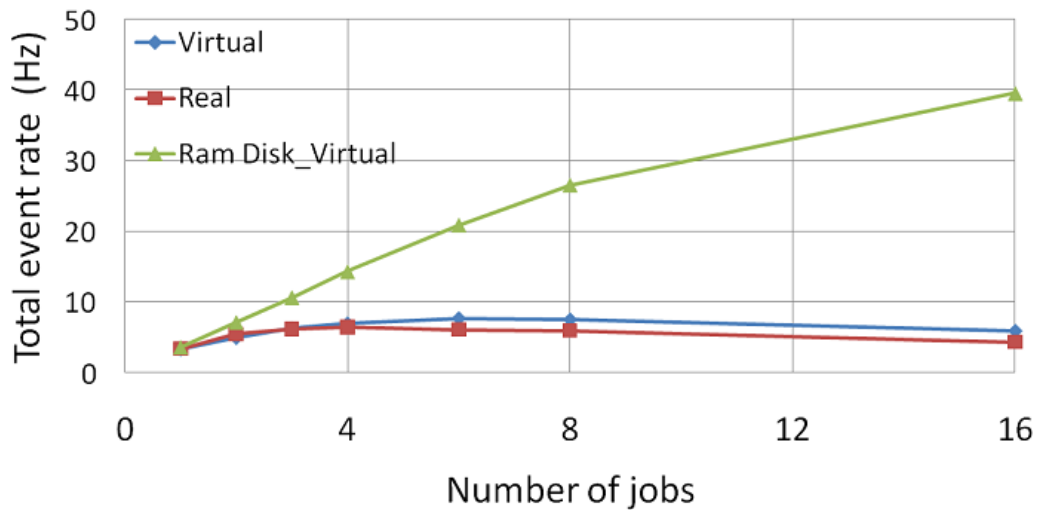


Figure 6.1: Athena performance with different number of nodes.

## 6.4  OSU Data Analysis Facility

At OSU an ATLAS tier 3 computing facility has been developed based on Virtual Machine (VM) technology. All worker nodes in the system are CERN-VM [93] based virtual machines running on a SUSE Xen hypervisor. The utilization of VM technology in a tier 3 computing farm was pioneered at OSU and allows simplification not only of system configuration and management, but also of experiment specific software installation and configuration. This in turn reduces the manpower required to run such a facility, which is an important factor

in the tier 3 context. Performance of a virtualized tier 3 facility has been explored with a variety of workloads typical for the ATLAS Collaboration, including MC event generation using the ATLAS software framework Athena, Athena based production of DPD datasets, and DPD based data analysis using Parallel ROOT (PROOF). The performance of typical ATLAS workloads in the virtualized environment is adequate, with an acceptably small performance penalty from virtualization in most scenarios. It is interesting to note that there are ATLAS scenarios where the virtual system outperformed the physical system (e.g. Figure 6.1). This is the first and only Virtual tier 3 ATLAS analysis center. A system design diagram of the OSU tier 3 is shown in Figure 6.2.
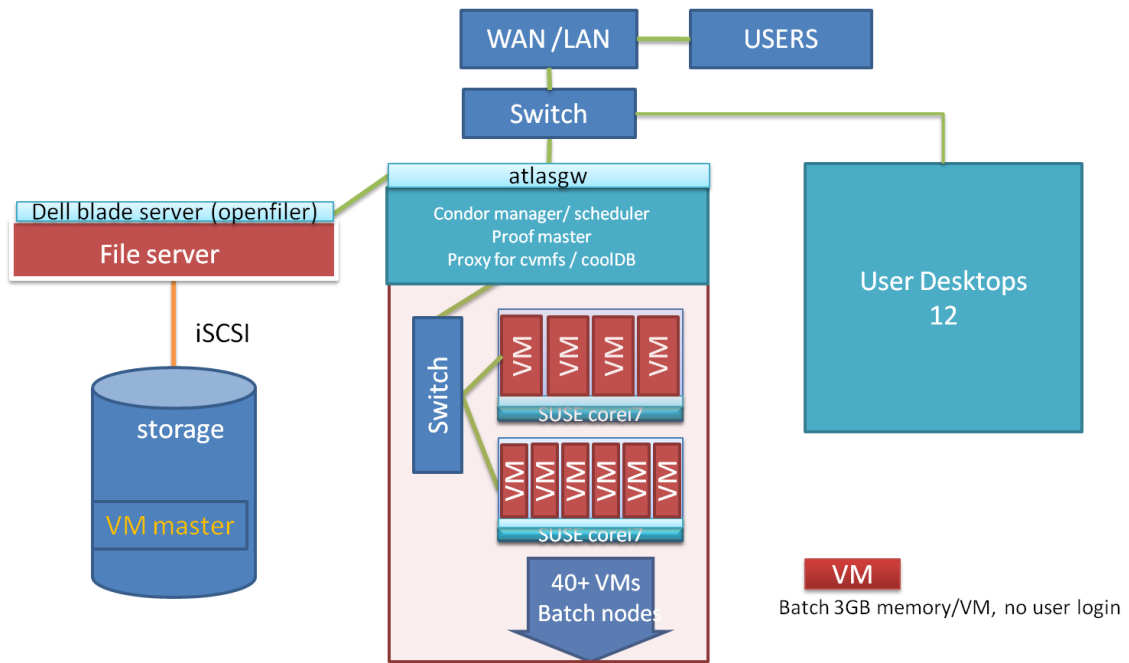


Figure 6.2: Schematic of the OSU ATLAS analysis center.

# Chapter 7

## EVENT SELECTION

## 7.1  Introduction

This analysis searches for LFV decay $Z \to e\mu$ in $pp$ collisions using the ATLAS detector at the LHC. The center of mass energy of the collision is $\sqrt{s} = 7$ TeV. Due to delays of the startup of the accelerator, at the time of writing only $\sim 3.4$ pb$^{-1}$ of data have been collected. Hence, the analysis presented here was performed with the available data as a proof of the concept and later it is shown with the simulated MC data to demonstrate the possible upper limit which can be achieved once $600$ pb$^{-1}$ of data has been collected. In this chapter, the criteria used for selecting potential signal events from the data are described. Also the signal yields and expected contributions from the backgrounds to the $ee$, $\mu\mu$, and $e\mu$ channels are estimated.

## 7.2  Data Set Pre-selection in D4PD Production

### 7.2.1  Introduction

Raw data are written out in physics streams based on trigger signatures at the CERN tier 0 facility. These data are subscribed to the Grid and during this process, the data is distributed to tier 1 facilities. At tier 1 facilities the reconstruction jobs are run on the datasets to produce Event Summary Data (ESD), AOD, and D3PD. The D3PDs are finally transfered to The Ohio State University tier 3 facility and converted to signature based D4PD's as described in Section 6.2 to increase the computational efficiency.

### 7.2.2 Event Based Pre-selection

During the pre-selection each event should pass either the hardware based L1 trigger chain with $E_T$ threshold of 10 GeV based on EM calorimeter or $p_T$ threshold of 6 GeV/c based on the muon spectrometer. If an event passes either of the chains, its electron and muon collections are scanned to find the signatures ($ee$, $e\mu$, $\mu\mu$) using electrons and muons that satisfied the relevant particle selection criteria. Next the overlap removal function checks whether the muons overlap with an electron. If there is an overlap (i.e. $\Delta R < 0.2$), the combination is rejected. If not all the information about the leptons is saved in the corresponding ROOT data tree for further analysis. Event related information, such as detector flags and $E_T^{miss}$ as well as non-overlapping jets are also saved. For counting the jets, the anti-$k_T$ with $R = 0.4$ jet reconstruction algorithm was used (Section 5.5.2).

### 7.2.3 Electron Pre-selection

Particles are considered electrons if reconstructed by the standard algorithm (Section 5.4.2) with minimum $P_T$ of 1 GeV/c, inside the detector ($|\eta| < 2.47$), excluding the transition gap region between the barrel and the end-cap of the calorimeter ($1.37 < |\eta| < 1.52$), and with "tight" electron quality (Section 5.4.4). For data this electron quality requirement is lowered to "medium" since the D4PDs are shared with other analyses. In the final stage of this analysis "tight" electrons are used. To reduce the number of fake candidates from beam-halo events, the electron track is also required to originate from a vertex position, within 15 cm along the beam axis and 0.2 cm radially from reconstructed primary vertex.

### 7.2.4 Muon Pre-selection

Particles are considered muons if reconstructed by the StaCo algorithm (Section 5.3) with minimum $P_T$ of 1 GeV/c. Also the muon should be inside the region $|\eta| < 2.4$. To reduce the number of fake candidates from cosmic-ray or beam-halo events, the muon track is also required to satisfy the same vertex requirements as the electron candidate.

| Physics process | Cross section $\times B$ (nb) | Sample size (nb$^{-1}$) |
|---|---|---|
| $Z \to \mu\mu$ ($m_{\mu\mu} > 60$ GeV/c$^2$) | 0.99 | $4.8 \times 10^6$ |
| $Z \to ee$ ($m_{ee} > 60$ GeV/c$^2$) | 0.99 | $5.1 \times 10^6$ |
| $Z \to \tau\tau$ ($m_{\tau\tau} > 60$ GeV/c$^2$) | 0.99 | $2.0 \times 10^6$ |
| $W \to e\nu$ | 10.46 | $6.7 \times 10^5$ |
| $W \to \mu\nu$ | 10.46 | $6.7 \times 10^5$ |
| $W \to \tau\nu$ | 10.46 | $1.1 \times 10^5$ |
| $b\bar{b}$ ($p_T^e > 7$ GeV/c) | $1.76 \times 10^3$ | $2.3 \times 10^3$ |
| $b\bar{b}$ ($p_T^\mu > 4$ GeV/c) | $1.17 \times 10^4$ | $1.7 \times 10^3$ |
| $c\bar{c}$ ($p_T^e > 7$ GeV/c) | $8.98 \times 10^2$ | $4.4 \times 10^3$ |
| $c\bar{c}$ ($p_T^\mu > 4$ GeV/c) | $8.42 \times 10^3$ | $1.2 \times 10^3$ |
| $t\bar{t}$ | 0.16 | $1.1 \times 10^7$ |
| $WW \to e + X$ or $\mu + X$ | $2.96 \times 10^{-2}$ | $1.4 \times 10^7$ |
| $WZ \to e + X$ or $\mu + X$ | $1.12 \times 10^{-2}$ | $4.7 \times 10^7$ |
| $ZZ \to e + X$ or $\mu + X$ | $4.59 \times 10^{-3}$ | $2.0 \times 10^8$ |

Table 7.1: MC samples used to calculate the 95% confidence level upper limit on $B(Z \to e\mu)$.

## 7.3 Data Sets

### 7.3.1 MC Data Sets

Since we are measuring the $B(Z \to e\mu)$ relative to $B(Z \to ee)$ and $B(Z \to \mu\mu)$, it is necessary to observe a $Z$ signal from $ee$ and $\mu\mu$ channels. The primary backgrounds to $Z \to ee$ and $\mu\mu$ decays are expected to be from decays of $Z \to \tau\tau$ and $W \to l\nu$ decays. For $Z \to e\mu$ decays, the primary backgrounds are expected to be from decays of $Z \to \tau\tau$ (where one $\tau$ decay to $\mu$ and the other to e), $Z \to ee$, $Z \to \mu\mu$, $W \to \mu\nu$ + fake $e$, and $W \to e\nu$ + fake $\mu$. In addition to those backgrounds all three channels are expected to have backgrounds from diboson productions (i.e. $WW$, $WZ$, $ZZ$) and heavy flavor decays (i.e. $c$, $b$, $t$). Background are estimated from MC simulations. All the simulated datasets except the heavy flavor samples are generated using PYTHIA [70], then simulated with GEANT4 [82] and fully reconstructed. PythiaB was used for the $b\bar{b}$ and $c\bar{c}$ datasets; MC@NLO was used for $t\bar{t}$ [77]. The full list of MC data sets used is shown in the Table 7.1.

## 7.3.2 Data Collected at $\sqrt{s} = 7$ TeV

The data used in this study was collected over a five month period from March through September 2010. All data were taken at $\sqrt{s} = 7$ TeV. Events used in this analysis must satisfy the L1 triggers: $E_T > 10$ GeV in the EM calorimeter (L1_EM10) or $p_T > 6$ GeV/c in the muon spectrometer (L1_MU6). The integrated luminosity is $3.15$ pb$^{-1}$ for the sample containing an electron and $3.12$ pb$^{-1}$ for the sample containing a muon. The invariant mass distributions of leptons after the pre-election are shown in Figures 7.1 - 7.3. In the $\mu\mu$ channel the $Z$, $\Upsilon$, and $J/\psi$ invariant mass peaks are clearly visible. In the $ee$ channel, most of the $\Upsilon$ and $J/\psi$ are excluded since we rejected electrons constructed from the "low-$p_T$" algorithm (Section 5.4.2). In the $e\mu$ channel, there are a few events near the $Z$ invariant mass since there is no $E_T^{miss}$ requirement in the pre-selection.
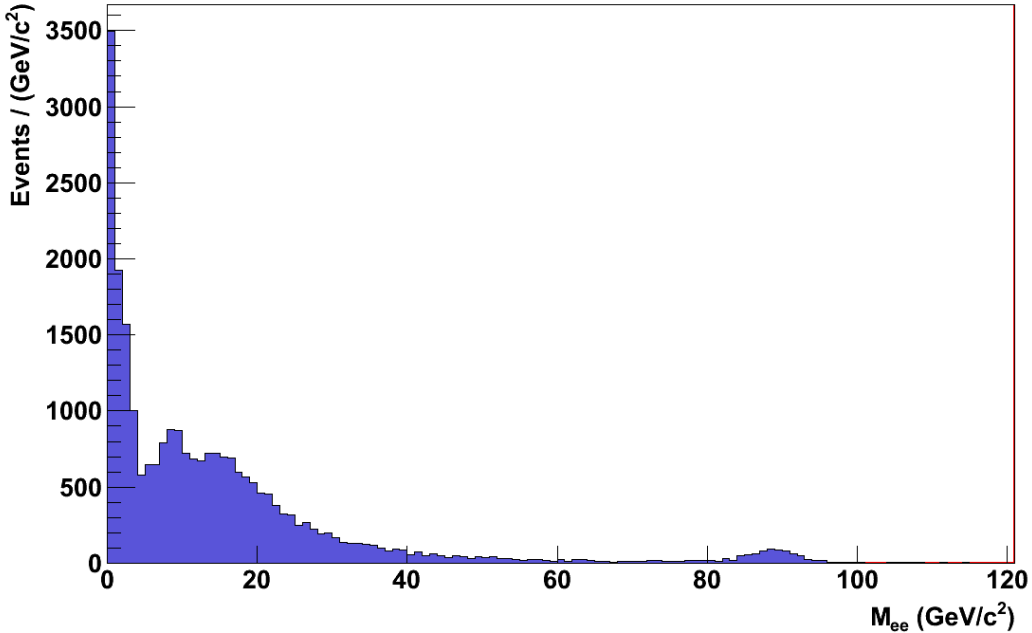


Figure 7.1: *ee* invariant mass distribution of the pre-selected events in the D4PD.
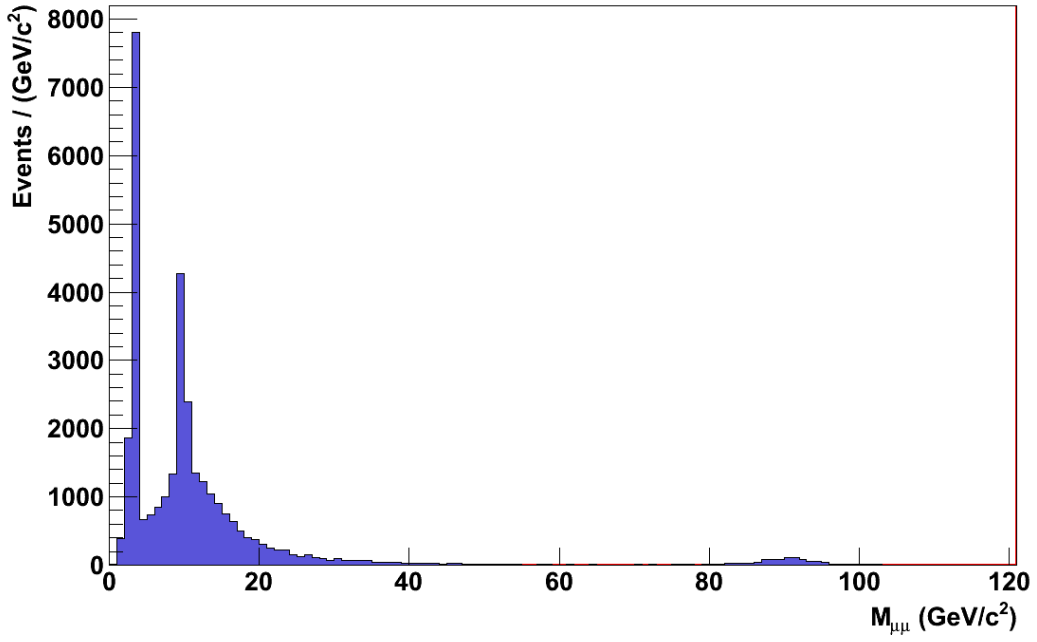
Figure 7.2: $\mu\mu$ invariant mass distribution of the pre-selected events in the D4PD.
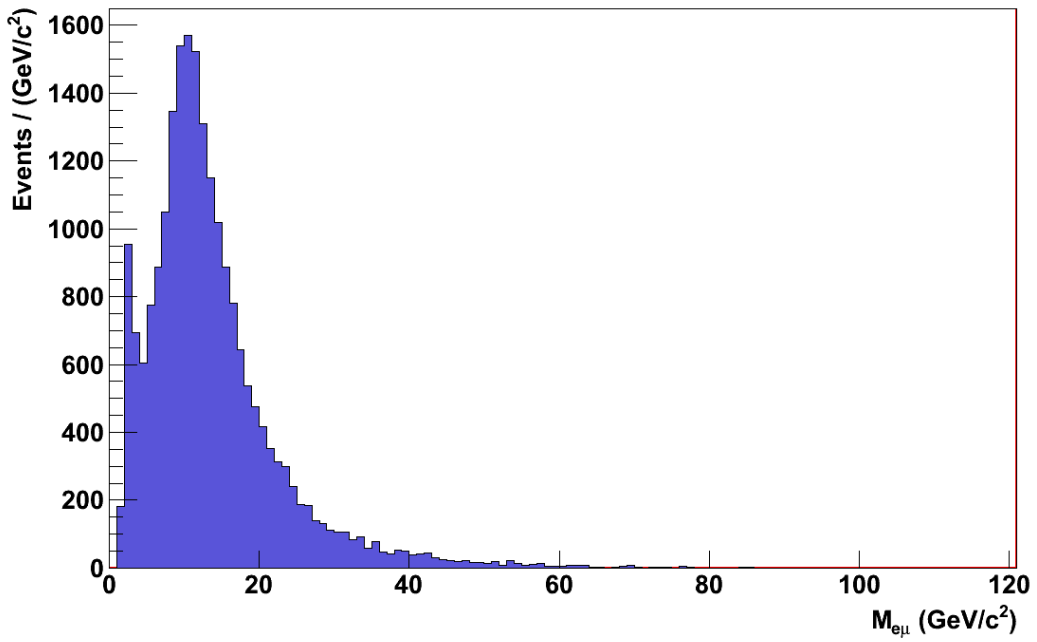


Figure 7.3: $e\mu$ invariant mass distribution of the pre-selected events in the D4PD.

| Object | Requirement |
|---|---|
| Event | $E_T^{miss} < 10$ GeV |
| | No jets with $p_T > 20$ GeV/c |
| Electron | "tight" quality |
| | $p_T > 15$ GeV/c |
| | isolation likelihood $> 1.0$ |
| Muon | $p_T > 15$ GeV/c |

Table 7.2: Final selection criteria for selecting events, electrons, and muons.

## 7.4  Selection of $Z$ Candidates

### 7.4.1  $e\mu$ channel

The D4PDs listed in 7.1 are scaled to the equivalent luminosity of data used for this analysis. With the pre-selection and "tight" criterion we expect 10.6 events from MC in the invariant mass range of 50 - 130 GeV/c$^2$ and observe 15 events in the data. The invariant mass distribution is shown in Figure 7.4 (a). The final selection requirements for this analysis are listed in Table 7.2. Since most of the background processes producing the $e\mu$ signature also produce neutrinos, the $E_T^{miss}$ is required to be low and a jet multiplicity requirement is added to reduce the jet background. The isolation likelihood is a measure of the isolation of electrons [94]. With the final selection criteria, 1.07 events are expected from MC (Table 7.3) for $60 < m_{ll} < 120$ GeV/c$^2$, and 0 events are observed in data. The final invariant mass distribution is shown in Figure 7.4 (b).

### 7.4.2  $ee$ and $\mu\mu$ channels

The selection criteria described in Section 7.4.1 is for both $ee$ and $\mu\mu$ channels. The background expectations for $60 < m_{ll} < 120$ GeV/c$^2$ are listed in Table 7.3. Note that the only significant background to all three channels are from $Z \rightarrow \tau\tau$. The $p_T$ spectra of the electrons and muons are shown in the Figure 7.5 and the $p_T$ distributions of the $Z$ candidates are shown in Figures 7.6 and 7.7. Misalignments in the barrel region of the muon spectrometer is the main reason for the disagreement between data and MC in the low $p_T$ region of the muon $p_T$ spectra and high $p_T$ region of the $Z$ candidates $p_T$ spectra [95].
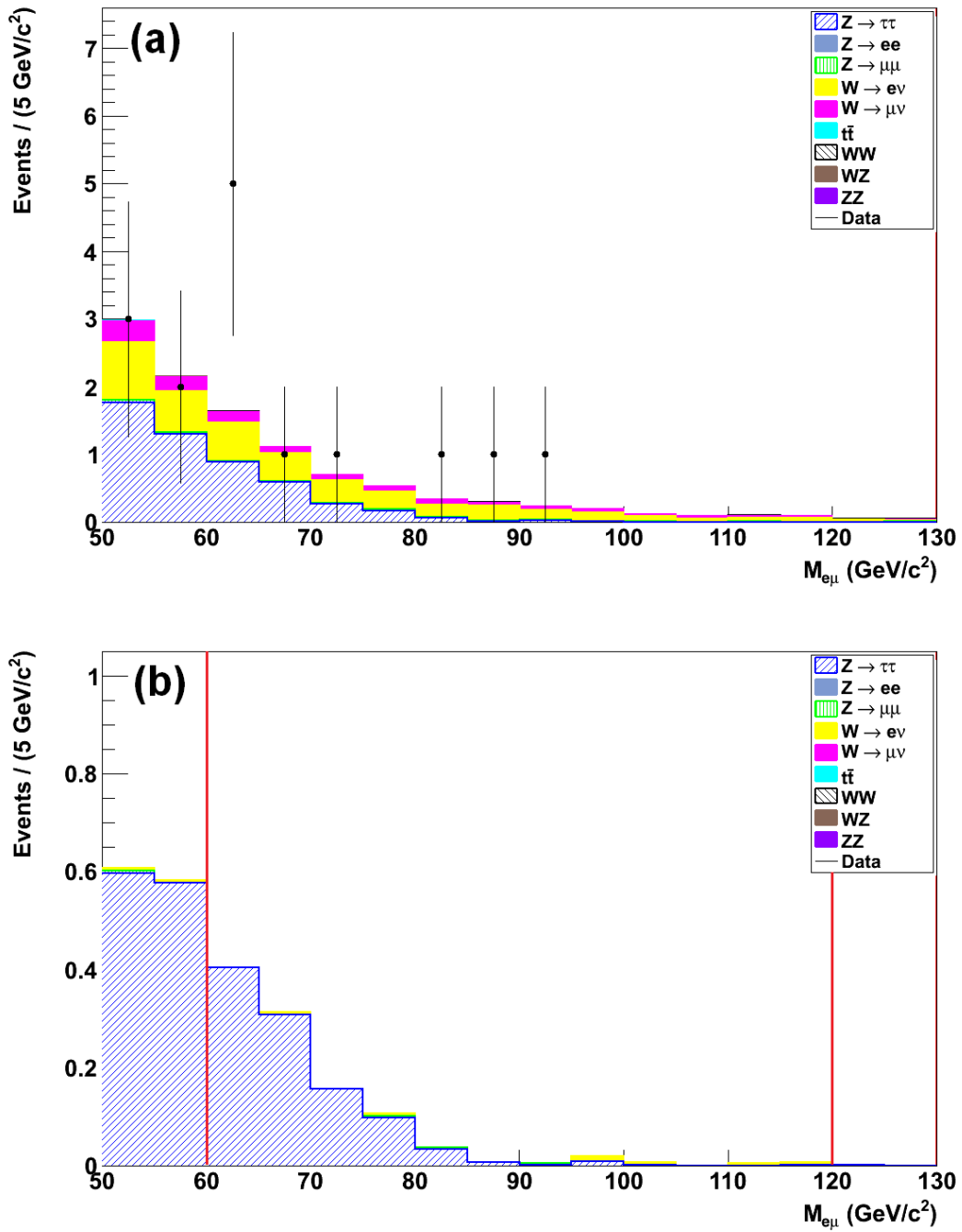
Figure 7.4: Invariant mass distribution of $e\mu$ candidates; before (a) and after (b) the final selection criteria, together with the background expectations.

| Process | $e\mu$ channel | $ee$ channel | $\mu\mu$ channel |
|---------|----------------|--------------|------------------|
| $Z \to \tau\tau$ | $1.02 \pm 0.27$ | $0.27 \pm 0.02$ | $0.88 \pm 0.06$ |
| $Z \to \mu\mu$ | $0.0085 \pm 0.0006$ | - | - |
| $W \to e\nu$ | $0.036 \pm 0.001$ | - | - |
| $W \to \mu\nu$ | - | - | $0.32 \pm 0.01$ |
| $WW \to e\mu + X$ | $0.0023 \pm 0.0003$ | $0.0008 \pm 0.0001$ | $0.0017 \pm 0.0004$ |
| $WZ \to e\mu + X$ | $0.0026 \pm 0.0004$ | $0.029 \pm 0.001$ | $0.090 \pm 0.0024$ |

Table 7.3: Expected number of background events for all three channels with invariant mass $60 < m_{ll} < 120$ GeV/c$^2$ at $\sim 3.1$ pb$^{-1}$. Background datasets with no background events in all channels are not shown.

| Parameter | $ee$ | $\mu\mu$ |
|-----------|------|----------|
| Events | $218.0 \pm 15.1$ | $510.0 \pm 23.0$ |
| Mass (GeV/c$^2$) | $88.31 \pm 0.29$ | $90.47 \pm 0.22$ |
| Width (GeV/c$^2$) | $2.83 \pm 0.53$ | $2.79 \pm 0.39$ |
| Resolution (GeV/c$^2$) | $2.90 \pm 0.88$ | $4.28 \pm 0.66$ |

Table 7.4: Summary of fit results for $ee$ and $\mu\mu$ channels.

The data are modeled[1] using Breit-Wigner convoluted with a Gaussian resolution function. The fit results are summarized in Table 7.4. These results are within the expected $Z$ mass and detector resolution of the electromagnetic calorimeter based on test-beam and early measurements [95, 96, 97]. Misalignments in the muon spectrometer and inner detector are the main reasons for the worse resolution of the muon channel. Additionally, the model used for fitting was tested further by fixing the $Z$ mass and natural width ($\Gamma$) to the known values [98]. The fit parameters obtained are listed in the Table 7.5. In all cases the number of events in $ee$ and $\mu\mu$ channels was found as same as in Table 7.4.

## 7.5 Efficiencies and Uncertainties

The efficiencies of three channels ($ee$, $e\mu$, and $\mu\mu$) is estimated using MC simulated datasets. The efficiency of any channel is defined as:

$$\epsilon_{ll} = \frac{N_{ll}^{selected}}{N_{ll}^{generated}} \tag{7.1}$$

[1]See Appendix A for detailed description of fitting procedure.
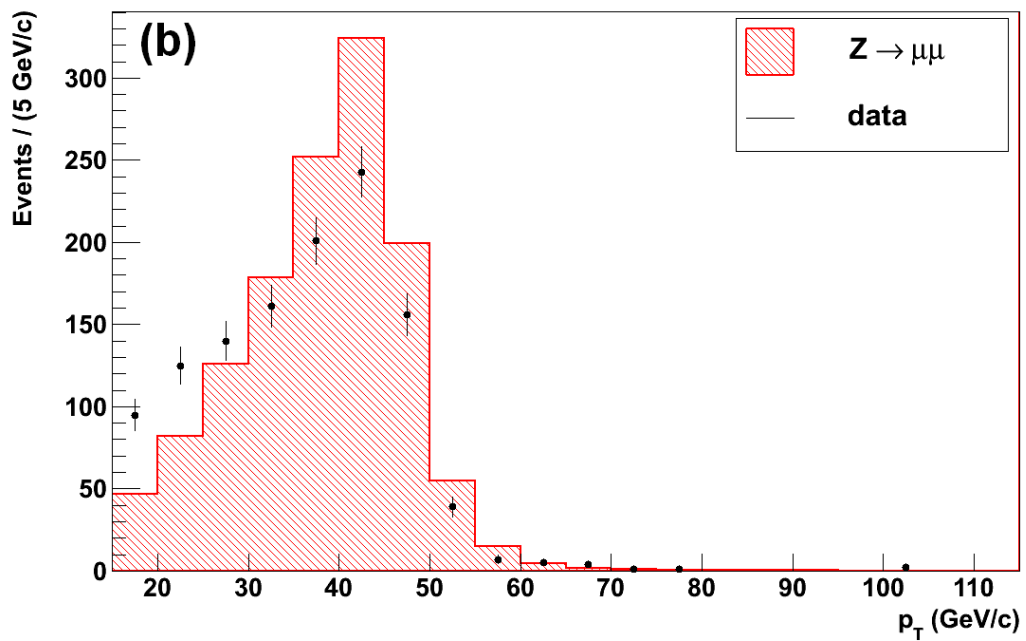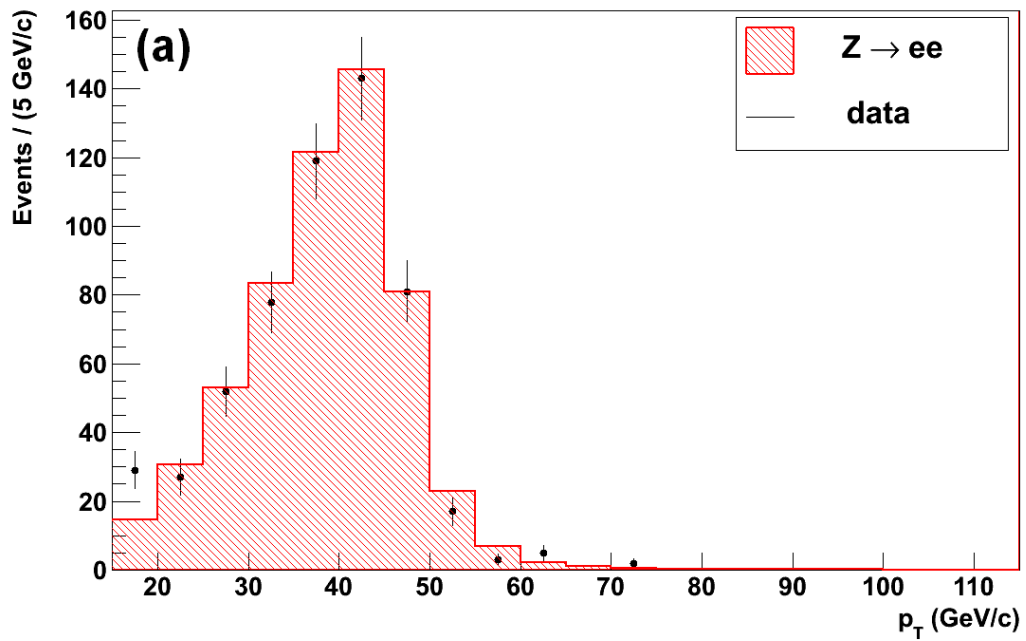
Figure 7.5: $p_T$ spectrum of electrons in the *ee* channel (a) and muons in the $\mu\mu$ channel (b) after the final selection criteria.

77
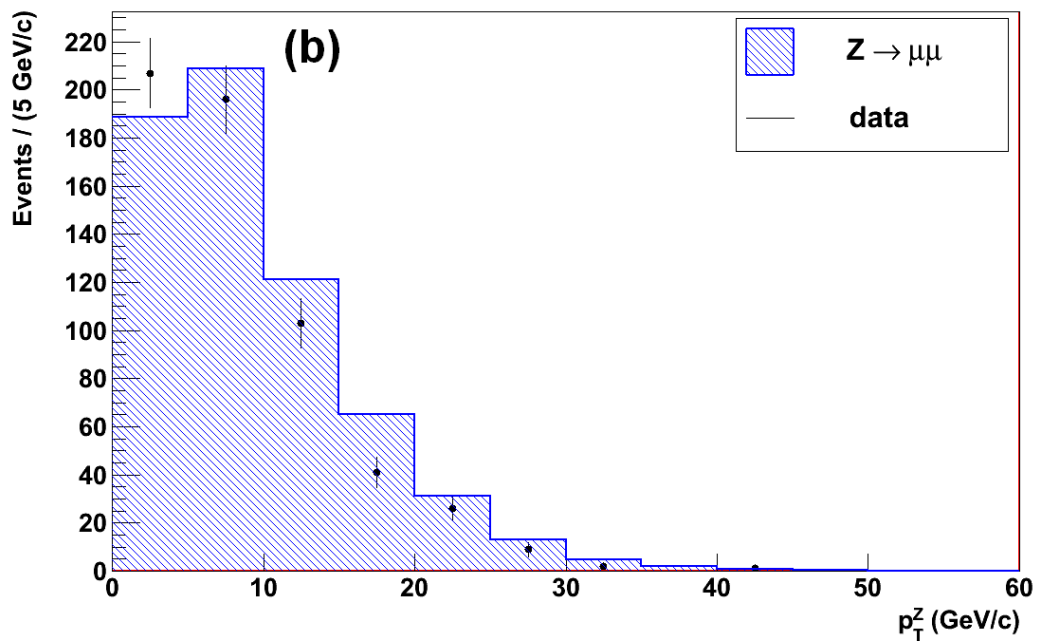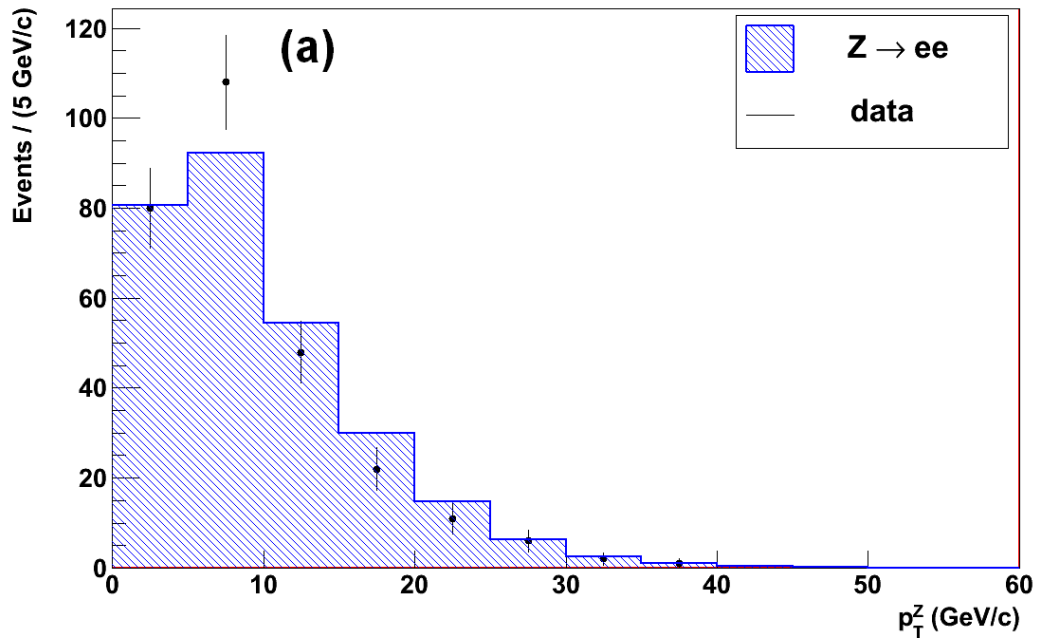
Figure 7.6: $p_T$ spectrum of $Z$ candidates of $Z \to ee$ (a) and $Z \to \mu\mu$ (b) after the final selection criteria.
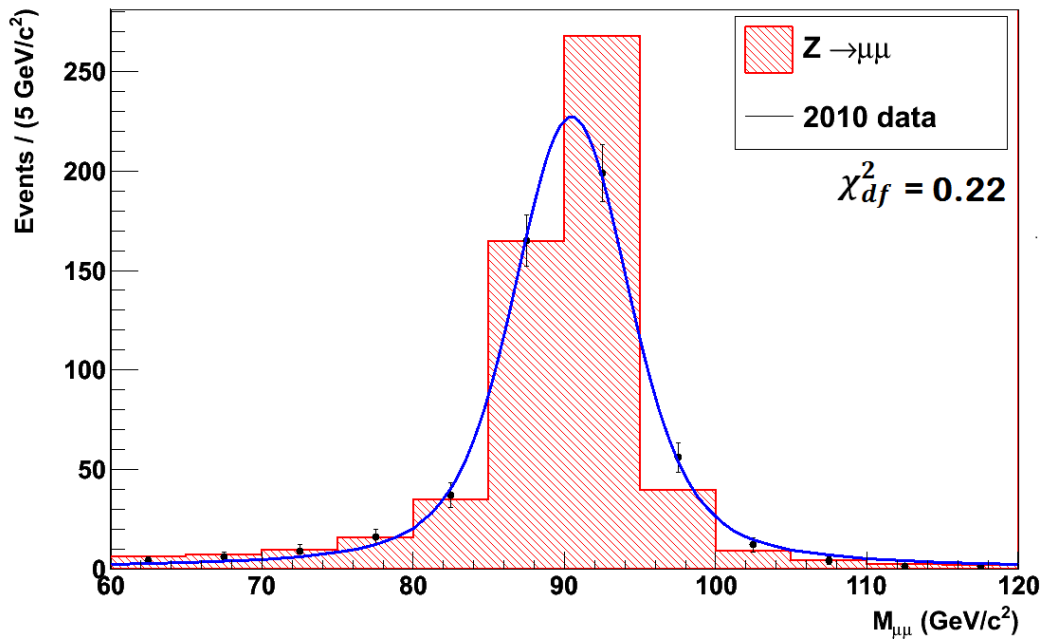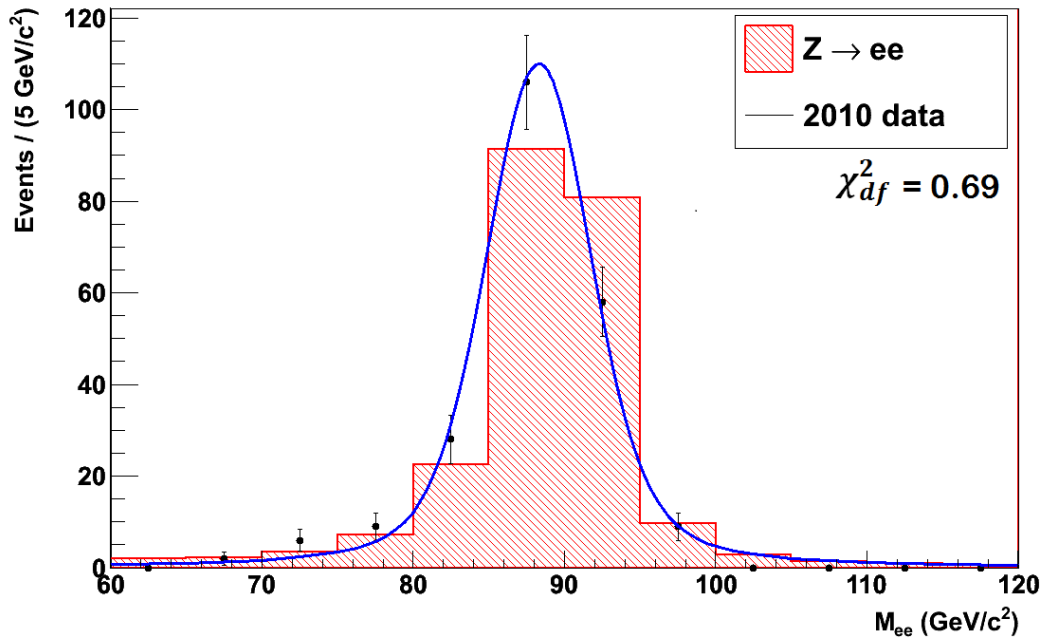
Figure 7.7: Invariant mass distribution of *ee* (a) and $\mu\mu$ (b) channels after the final selection criteria. The curve shows a fit to the data (see text).

| Channel | Events | Mass (GeV/c$^2$) | Width (GeV/c$^2$) | Resolution (GeV/c$^2$) |
|---|---|---|---|---|
| $ee$ | $218.0 \pm 15.1$ | 91.1876 (fixed to [98]) | $3.77 \pm 0.53$ | $3.28 \pm 1.03$ |
| $ee$ | $218.0 \pm 15.1$ | $88.33 \pm 0.29$ | 2.4952 (fixed to [98]) | $3.33 \pm 0.55$ |
| $\mu\mu$ | $510.0 \pm 22.9$ | 91.1876 (fixed to [98]) | $2.83 \pm 0.38$ | $4.32 \pm 0.67$ |
| $\mu\mu$ | $510.0 \pm 22.9$ | $90.47 \pm 0.22$ | 2.4952 (fixed to [98]) | $4.65 \pm 0.44$ |

Table 7.5: Summary of fit results for $ee$ and $\mu\mu$ channels when some parameters are fixed to known values from [98].

where $N_{ll}^{generated}$ is the number of MC events generated and $N_{ll}^{selected}$ is the number of events that passes the final selection criteria. The systematic uncertainties for each channel are discussed below:

## 7.5.1 Common Systematic Uncertainties

**PDF:** The main uncertainties on the acceptance is the limited knowledge of the parton distribution functions of the proton and the modeling of the $Z$ production at the LHC. This uncertainty is estimated as $\pm$ 3% per electron or muon by studying MC@NLO simulations [96].

**E$_T^{miss}$ scale and resolution:** Possible sources of uncertainties are the effects of pile-up, problematic regions in the detector, and energy scale on the algorithm used in calculation of $E_T^{miss}$. The uncertainty is estimated to be $\pm$ 2% per event [99].

**Trigger efficiency:** Estimated uncertainties from RPC and TGC triggers are $\pm$ 5% [100] for a muon and negligible for an electron [96].

## 7.5.2 Electron Systematic Uncertainties

**Electron identification:** The electron candidate is required to be well identified ("tight"). The uncertainty for this selection criteria is estimated as $\pm$ 8% [96] per electron. The sources of uncertainty are: material interaction effects upstream of the calorimeter, pile-up in the detector, and discrepancies in the IsEM variables (see Section 5.4.4).

**Energy scale and resolution:** A systematic uncertainty of $\pm$ 3% is assigned for EM

| Channel | Efficiency (%) |
|---------|----------------|
| $ee$    | $10.2 \pm 1.3$ |
| $e\mu$  | $17.7 \pm 2.4$ |
| $\mu\mu$ | $20.3 \pm 2.7$ |

Table 7.6: Summary of efficiencies for $ee$, $e\mu$, and $\mu\mu$ channels.

calorimeter energy scale and resolution for an electron based on test-beam studies and first in-situ measurements of $\pi^0 \rightarrow \gamma\gamma$ [97].

### 7.5.3  Muon Systematic Uncertainties

**Muon reconstruction:** The systematic uncertainty in muon reconstruction is estimated as $\pm 7\%$ [96] per muon. The main source of this uncertainty is the $\pi/K$ contamination.

**Energy scale and resolution:** A systematic uncertainty of $\pm 4\%$ is estimated for muon momentum scale and resolution of a muon [100].

### 7.5.4  Efficiencies and Uncertainties

We define the mass window shown in Figure 7.8 to calculate the efficiency for the signal. The total systematic uncertainties are the quadratic sum of the applicable effects. The results are listed in Table 7.6.
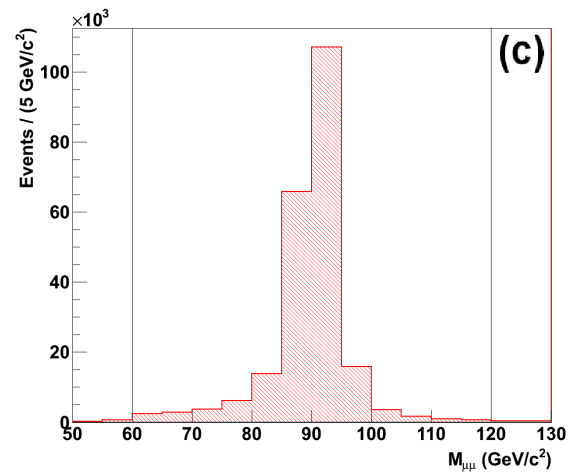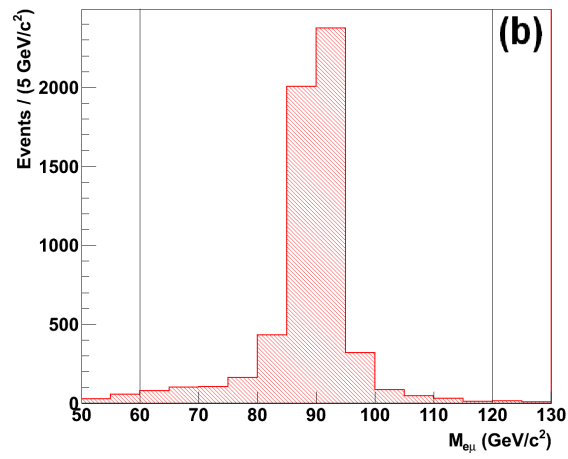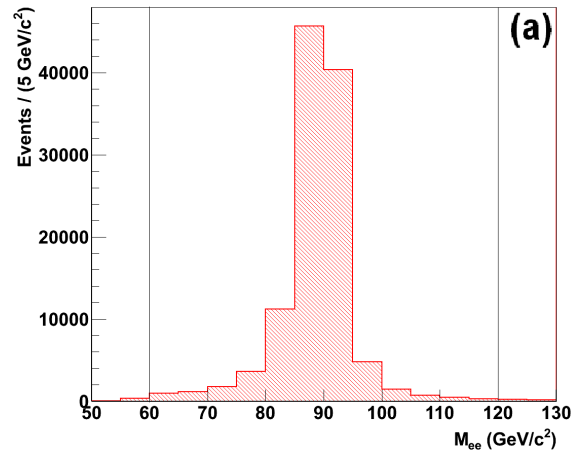
Figure 7.8: Invariant mass distributions of $Z \to ee$ (a), $Z \to e\mu$ (b), and $Z \to \mu\mu$ (c) from MC after the final selection criteria. The invariant mass range of 60 - 120 GeV/c$^2$ was used for the calculation of efficiencies.

# Chapter 8

# ANALYSIS TECHNIQUES AND RESULTS

## 8.1 Introduction

This analysis present the results of a search for evidence of LFV decays of $Z$ bosons to $e\mu$ pairs in $pp$ collisions at $\sqrt{s} = 7$ TeV using the ATLAS detector. Selection criteria for the data and MC sample are described in the previous chapter and summarized in Table 8.1. In this chapter, the expected signal yields and background contributions to each channel ($ee$, $\mu\mu$, and $e\mu$) are determined and the 95% confidence level upper limit is calculated for the $Z \to e\mu$ channel.

## 8.2 Branching Ratio

The $Z \to e\mu$ branching ratio is calculated as follows:

$$B(Z \to e\mu) = \frac{N^0_{e\mu}}{N^0_Z} \tag{8.1}$$

$$= \frac{N_{e\mu}}{\epsilon_{e\mu} N^0_Z}, \tag{8.2}$$

where $N^0_Z$ is the total number of $Z$'s produced, $N^0_{e\mu}$ is the number of $Z \to e\mu$ produced, $N_{e\mu}$ is the number of $Z \to e\mu$ events observed, and $\epsilon_{e\mu}$ is the detecting efficiency. $N^0_Z$ can be calculated from two independent measurements, $N^0_{Z_{ee}}$ from $Z \to ee$, and $N^0_{Z_{\mu\mu}}$ from $Z \to \mu\mu$ :

$$N^0_{Z_{ee}} = \frac{N_{ee}}{\epsilon_{ee} B(Z \to ee)} \tag{8.3}$$

| Object | Requirement |
|---|---|
| Event | $E_T^{miss} < 10$ GeV |
| | Number of non-overlapping jets with $p_T > 20$ GeV/c $= 0$ |
| Electron | "tight" quality |
| | $p_T > 15$ GeV/c |
| | isolationlikelihood $> 1.0$ |
| Muon | $p_T > 15$ GeV/c |

Table 8.1: Final selection criteria for selecting events, electrons, and muons.

$$N_{Z_{\mu\mu}}^0 = \frac{N_{\mu\mu}}{\epsilon_{\mu\mu}B(Z \to \mu\mu)}, \tag{8.4}$$

where $\epsilon_{ee}$ and $\epsilon_{\mu\mu}$ are efficiencies for selecting $Z \to ee$ and $Z \to \mu\mu$ events respectively and $N_{ee}$ ($N_{\mu\mu}$) is the number of observed $Z \to ee$ ($Z \to \mu\mu$) signal events after background subtraction. For this analysis we used the weighted average $\overline{N}_Z^0$ for the number of $Z$s produced:

$$\overline{N}_Z^0 = \frac{\left(\frac{N_{ee}}{\epsilon_{ee}B(Z \to ee)\sigma_{ee}^2} + \frac{N_{\mu\mu}}{\epsilon_{\mu\mu}B(Z \to \mu\mu)\sigma_{\mu\mu}^2}\right)}{\left(\frac{1}{\sigma_{ee}^2} + \frac{1}{\sigma_{\mu\mu}^2}\right)} \tag{8.5}$$

and therefore

$$B(Z \to e\mu) = \frac{N_{e\mu}}{\overline{N}_Z^0 \epsilon_{e\mu}}. \tag{8.6}$$

Here $\sigma_{ee}$ ($\sigma_{\mu\mu}$) is the uncertainties in $N_{Z\to ee}$ ($N_{Z\to\mu\mu}$). To calculate the upper limit for $B(Z \to e\mu)$, we used the unified approach of Feldman and Cousins [101]:

$$B(Z \to e\mu) < \frac{N_{95\%}}{\epsilon_{e\mu}\overline{N}_Z^0}. \tag{8.7}$$

$N_{95\%}$ is taken from the Table VI in [101], a small portion of which is reproduced in Table 8.2.

## 8.3 Results

The invariant mass spectrum of selected $e\mu$ events satisfying all selection criteria as shown in Figure 7.4 is reproduced in Figure 8.1. There is no $e\mu$ events above invariant mass of 50

| $n_0 \backslash b$ | 0.0 | 0.5 | 1.0 |
|---|---|---|---|
| 0 | 0.00, 3.09 | 0.00, 2.63 | 0.00, 2.33 |
| 1 | 0.05, 5.14 | 0.00, 4.64 | 0.00, 4.14 |
| 2 | 0.36, 6.72 | 0.00, 6.22 | 0.00, 5.72 |
| 3 | 0.82, 8.25 | 0.32, 7.75 | 0.00, 7.25 |

Table 8.2: 95% confidence level intervals for the signal for $n_0$ observed events with known background $b$.

| Component | Events |
|---|---|
| Signal for $Z \to ee$ | $218.0 \pm 15.1$ |
| Signal for $Z \to \mu\mu$ | $510.0 \pm 22.9$ |
| Background for $Z \to ee$ | $0.30 \pm 0.02$ |
| Background for $Z \to \mu\mu$ | $1.29 \pm 0.05$ |
| Background subtracted signal for $Z \to ee$ | $217.7 \pm 15.1$ |
| Background subtracted signal for $Z \to \mu\mu$ | $508.7 \pm 22.9$ |
| $B(Z \to ee)$ | $(3.363 \pm 0.004)$ % [98] |
| $B(Z \to \mu\mu)$ | $(3.366 \pm 0.004)$ % [98] |
| $\epsilon_{ee}$ | $(10.2 \pm 1.3)\%$ |
| $\epsilon_{\mu\mu}$ | $(20.3 \pm 2.7)\%$ |
| $\epsilon_{e\mu}$ | $(17.7 \pm 2.4)\%$ |
| $N_{95\%}$ | 2.33 |

Table 8.3: All the components used to calculate the 95% confidence upper limit on $B(Z \to e\mu)$, with invariant mass range 60-120 GeV/c$^2$.

GeV/c$^2$. Using the unified approach of Feldman and Cousins, this corresponds to an 95% upper limit of 2.63 events (Table 8.2). All the necessary elements to calculate the upper limit for the $B(Z \to e\mu)$ are summarized in the Table 8.3. By using the Equations 8.3 and 8.4, we obtained $N^0_{Z_{ee}}$ and $N^0_{Z_{\mu\mu}}$ as $(6.3 \pm 0.9) \times 10^4$ and $(7.5 \pm 0.9) \times 10^4$ respectively, where the error include all uncertainties. The weighted average is $\overline{N}^0_Z = (6.7 \pm 0.5) \times 10^4$. From Equation 8.7, we obtain $B(Z \to e\mu) < 2.0 \times 10^{-4}$ with 95% confidence level. In this upper limit both the statistical and systematic uncertainties are incorporated using the prescription of Highland and Cousins [102].
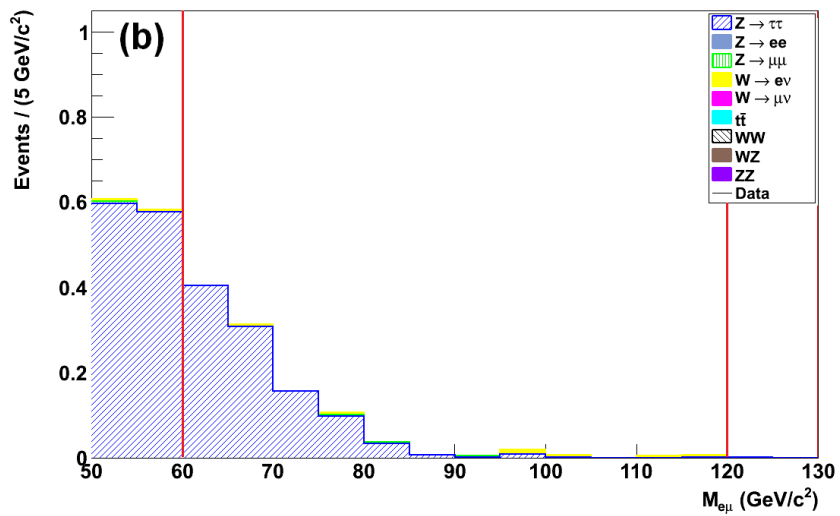
Figure 8.1: Invariant mass distribution of data and MC for the $e\mu$ channel after the final selection. MC files listed in Table 7.1 are scaled to the equivalent luminosity of data.

# Chapter 9

## EXPECTATIONS WITH ADDITIONAL DATA

### 9.1 Introduction

In this chapter the sensitivity with 650 pb$^{-1}$ of data is discussed. The ATLAS experiment will collect 1 fb$^{-1}$ of $pp$ collision at $\sqrt{s} = 7$ TeV by the end of 2011. The same MC simulated datasets discussed in Section 7.3.1 are used for this study.

### 9.2 Determination of Selection Criteria

We have studied several methods to determine selection criteria that reduce the background. First by applying rectangular selection criteria and maximizing significance[2] and later using sophisticated multivariate methods such as Fisher discriminants, Artificial Neural Networks (ANN), and Boosted Decision Trees (BDT) through the TMVA package in ROOT. One major advantage of the multivariate analysis technique is its ability to rank a set of variables by their discriminating power between signal and background. The understanding of the ATLAS experiment is at an early stage, hence the MC simulations are not yet well calibrated and, with only a small number of background events, multivariate techniques have the potential to over-train the criteria. For these reasons, this analysis uses rectangular cuts. However, TMVA is used to find the variables with the most discriminating power and to tune the rectangular criteria to be used.

---

[2]significant is the $\frac{s}{\sqrt{s+b}}$, where $s$ ($b$) = number of expected signal (background) events.

| Rank | Variable | Separation |
|------|----------|------------|
| 1 | $E_T^{miss}$ | 0.753 |
| 2 | $P_T^{\mu}$ | 0.333 |
| 3 | $P_T^{\mu}$ (cone $< 30$)$/P_T^{\mu}$ | 0.230 |
| 4 | $P_T^e$ | 0.214 |
| 5 | $N_{jet}$ ($E_{jet} > 20$ GeV) | 0.194 |
| 6 | $\mathcal{L}_{isolation}^e$ | 0.082 |
| 7 | $f_1^e$ | 0.053 |
| 8 | $W_{shower}^e$ | 0.049 |

Table 9.1: Ranking of variables through TMVA.

### 9.2.1 Variables

The discriminating power of all available variables was tested using TMVA. For this purpose, the simulated signal and the combined simulated background datasets were used. Variables were selected to have the most discriminating power with the Fisher method [103]. The TMVA output with the list of variables ranked by discriminating power is shown in Table 9.1:

* $E_T^{miss}$ is the final refitted and calibrated $E_T^{miss}$ of the event.

* $N_{jet}$ ($E_{jet} > 20$ GeV) is the number of jets with transverse energy $> 20$ GeV (excluding those overlapping with the signature leptons).

* $P_T^{\mu}$ and $P_T^e$ are transverse momenta of the muon and electron respectively.

* $P_T^{\mu}$ (cone $< 30$)$/P_T^{\mu}$ is a measurement of isolation of the muon ($P_T^{\mu}$ (cone $< 30$) is the sum of the transverse momenta of all the tracks in a cone of $\Delta R = \sqrt{\Delta\phi^2 + \Delta\eta^2} < 0.3$ around the selected muon track).

* $\mathcal{L}_{isolation}^e$ is a measure of the isolation of the electron by combining calorimetric and tracking isolation variables using a likelihood estimator [94].

* $f_1^e$ is the fraction of the electron's energy found in the first electromagnetic sampling calorimeter.

*  $W^e_{shower}$ is a measurement of the geometric width of the electromagnetic shower.

The distributions of signal and background for the selected variables are shown normalized to unity in the Figures 9.1 - 9.4. The background is the total background from Table 7.1 scaled to 650 pb$^{-1}$.
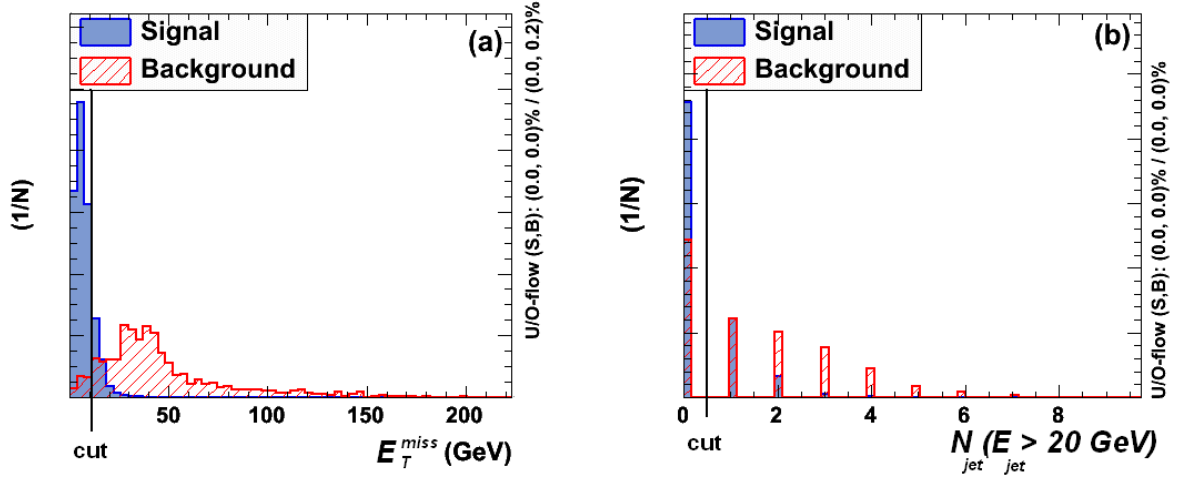


Figure 9.1: $E_T^{miss}$ (a) and $N_{jet}$ ($E_{jet} > 20$ GeV) (b) of the signal and the background. Both the signal and the background are normalized to one.

### 9.2.2 Optimizing Rectangular Selection Criteria

The rectangular selection criteria for this analysis are optimized using TMVA. TMVA optimizes the significance ($\frac{S}{\sqrt{S+B}}$), scanning over the full range of allowed values of the variables. Using this method, the selection criteria (shown in the Table 9.2) were determined. The selection criteria were tuned using datasets approximately normalized to minimum luminosity required ($\sim$650 pb$^{-1}$) to be competitive with the current upper limit. The TMVA cut optimization output is shown in Figure 9.5.

89
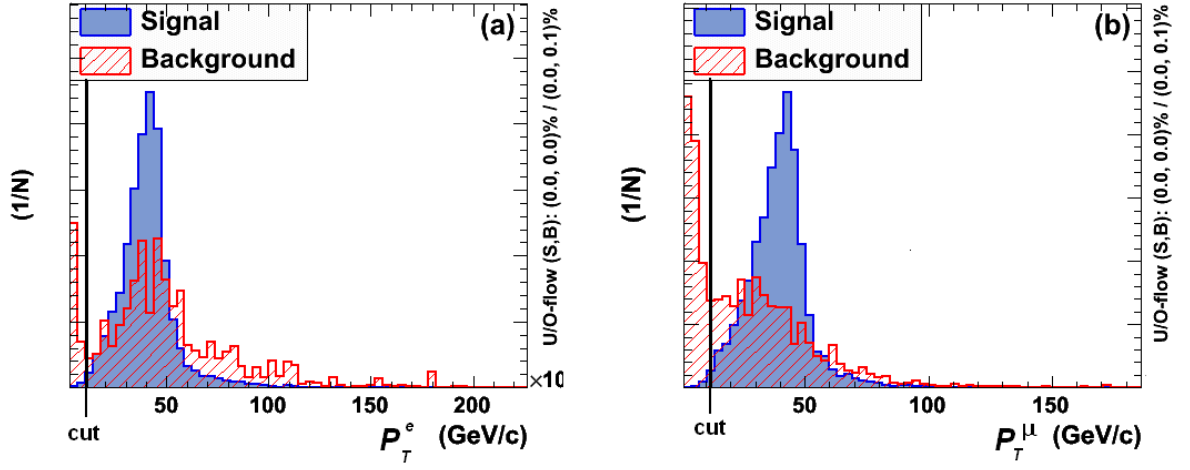
Figure 9.2: Transverse momentum of electrons (a) and muons (b) of the signal and the background. Both the signal and the background are normalized to one.
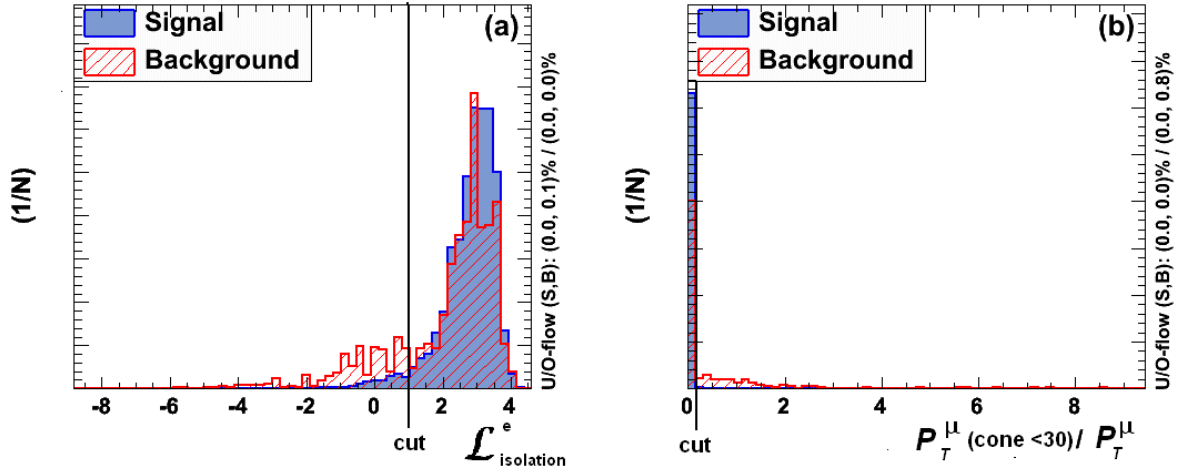


Figure 9.3: Distributions of isolation likelihood of electrons (a) and isolation of muons (b) of the signal and the background. Both the signal and the background are normalized to one.
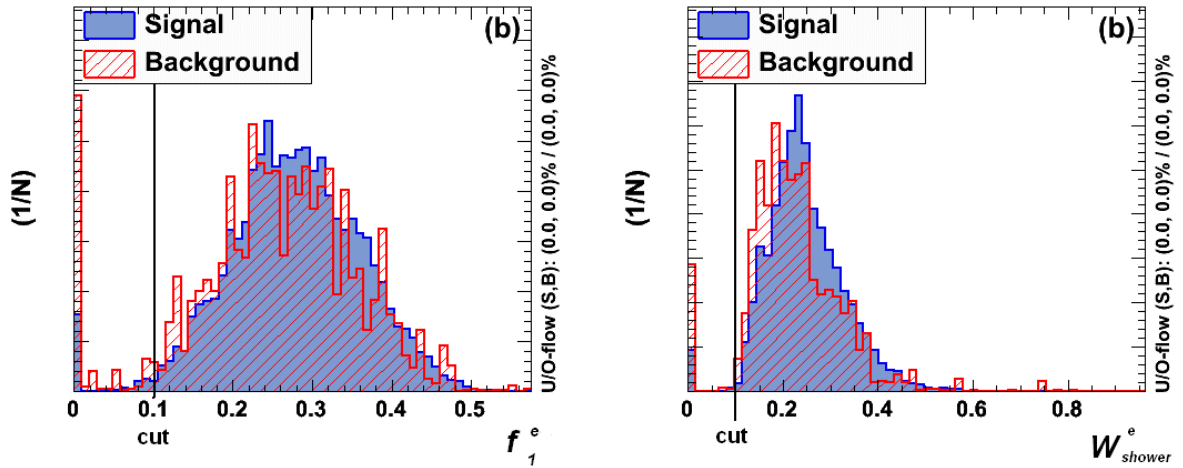
Figure 9.4: Distributions of the fraction of energy in the $1^{st}$ sampling calorimeter (a) and the shower width (b) of the signal and the background. Both the signal and the background are normalized to one.
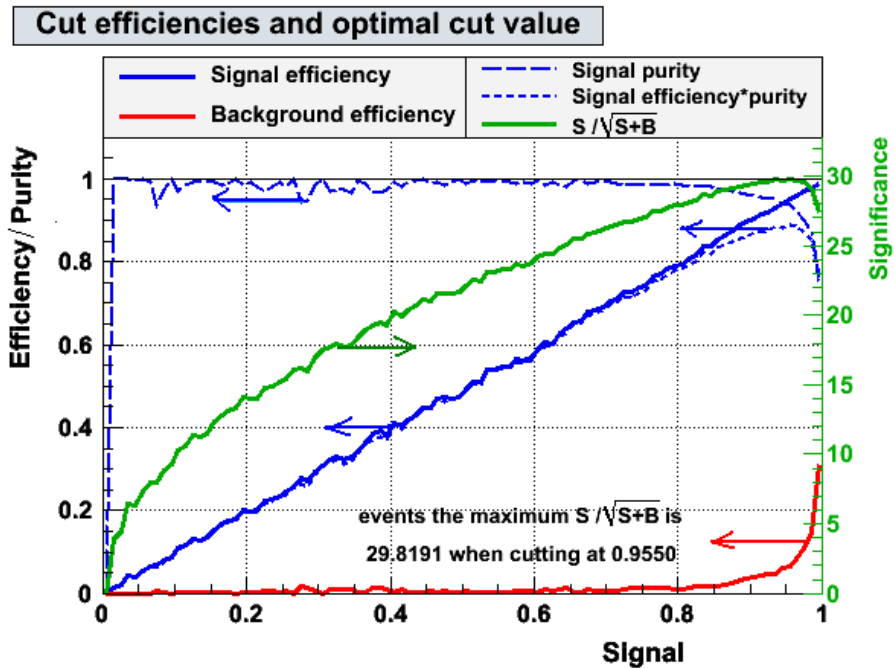


Figure 9.5: TMVA cut optimization, with each point corresponds to a different set of selection criteria.

| $E_T^{miss} < 10$ GeV |
|---|
| $N_{jet}$ $(E_{jet} > 20$ GeV$) = 0$ |
| $P_T^e > 10$ GeV/c |
| $P_T^\mu > 12$ GeV/c |
| $\mathcal{L}_{isolation}^e > 1.0$ |
| $P_T^\mu$ (cone $< 30)/P_T^\mu < 0.1$ |
| $f_1^e > 0.1$ |
| $W_{shower}^e > 0.12$ |

Table 9.2: Final selection criteria for $Z \to ll$.

| Figure | Expected signal |
|---|---|
| 9.7 | $(4.56 \pm 0.02) \times 10^4$ |
| 9.8 | $(1.21 \pm 0.03) \times 10^5$ |

Table 9.3: Expected number of signal events in $ee$ and $\mu\mu$ channels with $70 < m_{ll} < 170$ GeV/c$^2$ for 650 pb$^{-1}$ of MC data.

## 9.3 Results

The invariant mass distribution of the opposite-sign lepton pairs after applying the final selection criteria, as shown in Table 9.2, is presented in Figures 9.6 - 9.8. The MC signal data are fitted using Breit-Wigner convoluted with a Gaussian resolution function. The invariant mass distributions are asymmetric due to bremsstrahlung and contributions from $Z/\gamma^*$ at low invariant mass. However for this analysis we are fitting those distributions to a symmetric resolution function to estimate the number of signals.

Table 9.3 summarizes the number of $Z \to ll$ signal events estimated inside the invariant mass window $70 < m_{ll} < 170$ GeV/c$^2$. The major backgrounds are summarized in Table 9.4. Due to limited statistics in $Z \to \tau\tau$ dataset, no background events are found in the mass window of 88 - 94 GeV/c$^2$. Figure 9.9 shows the invariant mass distribution of the $Z \to \tau\tau$ (unscaled) before and after the $E_T^{miss}$ selection criteria, which indicates that a MC sample of 2 fb$^{-1}$ still has limited precisions in determining the number of background events in this region.

Efficiencies of the three channels ($ee$, $e\mu$, and $\mu\mu$) are calculated similar to Section
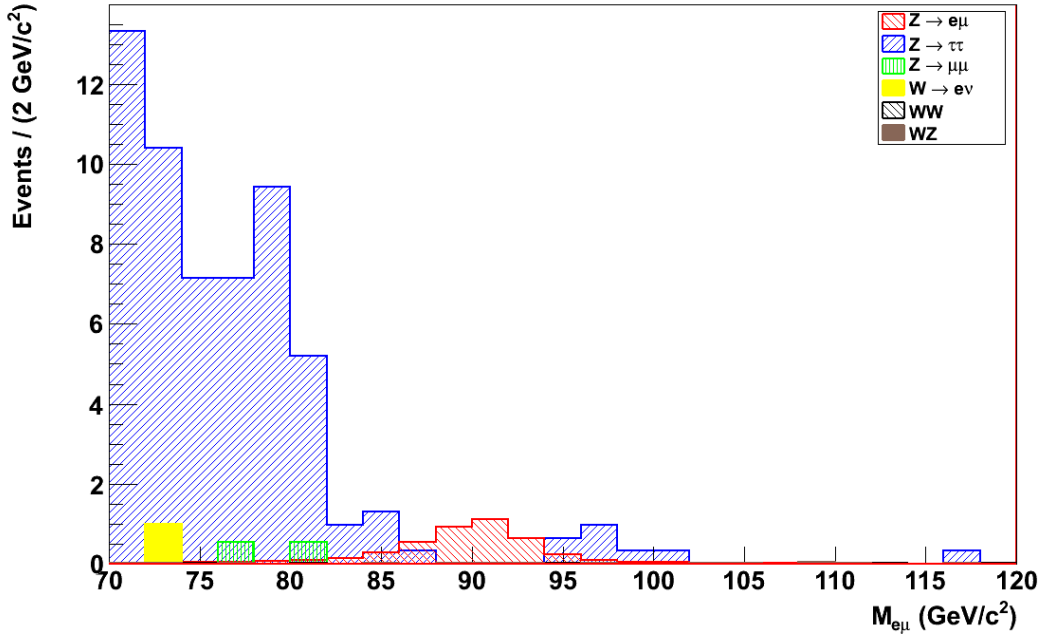
Figure 9.6: Invariant mass spectrum of selected $e\mu$ candidates normalized to 650 pb$^{-1}$. The $Z \to e\mu$ signal is scaled to the current upper limit of $1.7\times 10^{-6}$.
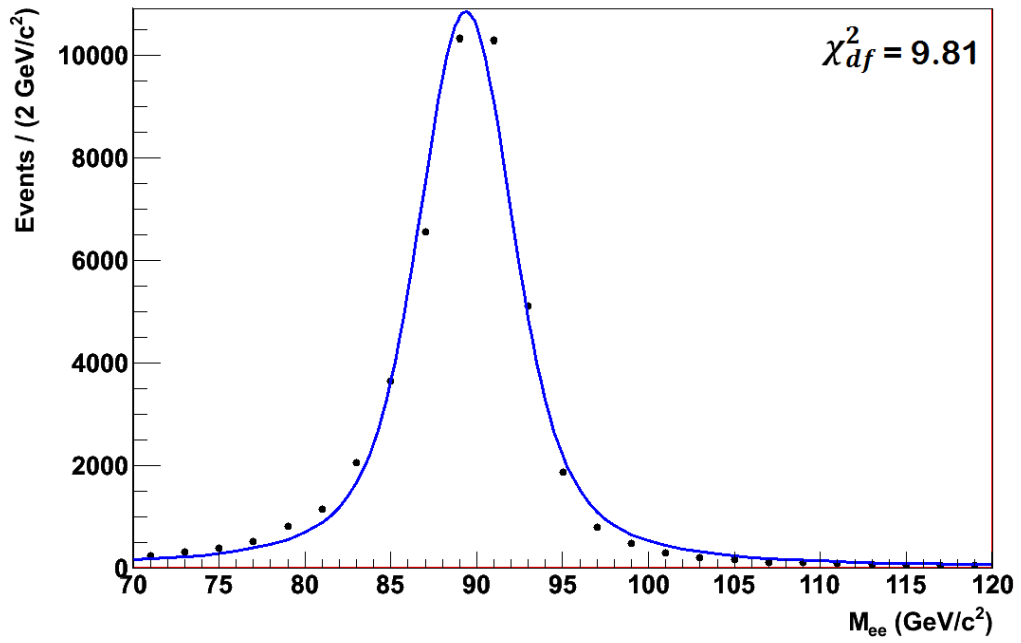


Figure 9.7: A fit to the invariant mass spectrum of $ee$ candidates for 650 pb$^{-1}$.
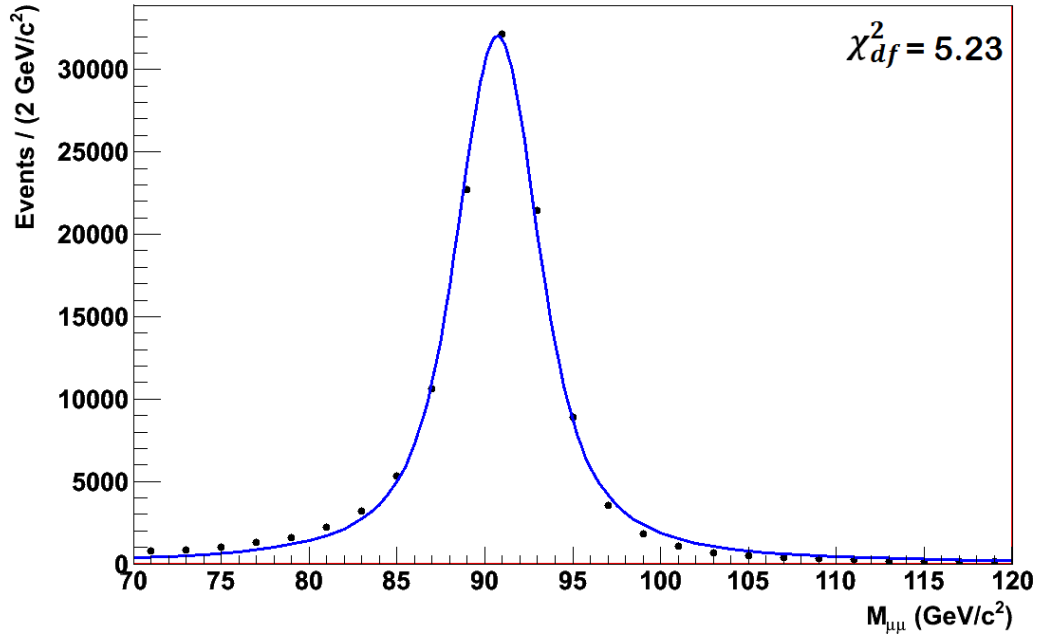
Figure 9.8: A fit to the invariant mass spectrum of $\mu\mu$ candidates for 650 pb$^{-1}$.
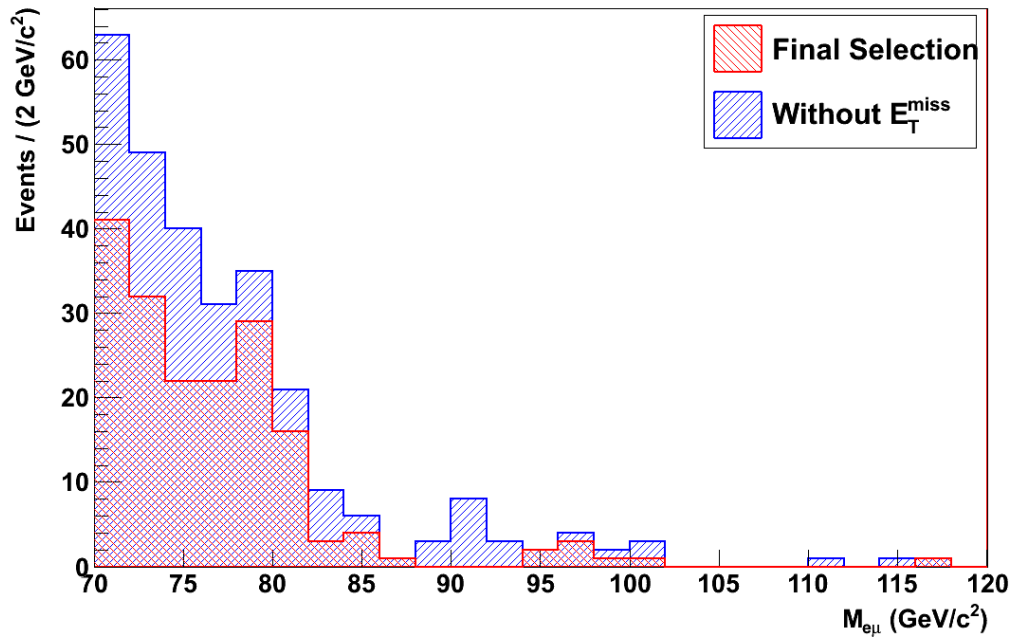


Figure 9.9: Invariant mass spectrum of $e\mu$ candidates from $Z \to \tau\tau$ background sample. All selection criteria has been imposed (red) except the $E_T^{miss}$ requirement (blue).

| Process | $e\mu$ channel | $ee$ channel | $\mu\mu$ channel |
|---------|----------------|--------------|------------------|
| $WW \to e\mu + X$ | $0.268 \pm 0.023$ | $0.148 \pm 0.023$ | $1.563 \pm 0.008$ |
| $WZ \to e\mu + X$ | $0.038 \pm 0.005$ | $3.124 \pm 0.125$ | $0.075 \pm 0.001$ |
| $ZZ \to e\mu + X$ | $0.0034 \pm 0.0007$ | - | $0.050 \pm 0.003$ |
| $W \to e\nu$ | $0.9 \pm 0.1$ | - | - |
| $Z \to \mu\mu$ | $1.6 \pm 0.6$ | - | - |
| $Z \to \tau\tau$ | $57.8 \pm 0.7$ | $20.1 \pm 0.5$ | $58.8 \pm 1.2$ |

Table 9.4: Expected number of background events for all three channels with 650 pb$^{-1}$ of MC data. Background datasets with no events in all channels are not shown.

| Channel | Efficiency (%) |
|---------|----------------|
| $ee$ | $9.5 \pm 1.2$ |
| $e\mu$ | $15.3 \pm 2.0$ |
| $\mu\mu$ | $20.2 \pm 2.3$ |

Table 9.5: Summary of efficiencies for $ee$, $e\mu$, and $\mu\mu$ channels.

7.5. The systematic uncertainties are assumed to be similar to current uncertainties. The efficiencies are listed in Table 9.5. By using the Equation 8.3 (8.4), $N^0_{Z_{ee}}$ ($N^0_{Z_{\mu\mu}}$) is calculated as $(1.42 \pm 0.18) \times 10^7$ ($(1.78 \pm 0.21) \times 10^7$). The weighted average, $\overline{N}^0_Z$ is $(1.52 \pm 0.14) \times 10^7$, from Equation 8.5. The errors are the total uncertainties, dominated by the systematic uncertainties which have been assumed to be similar to current uncertainties. However we expect the systematic errors will be reduced in the future with more data for cross check.

### 9.3.1 Modeling the Signal and Background of $e\mu$ Channel

Assuming that there is no $Z \to e\mu$ signal in the data, we can calculate the upper limit for $B(Z \to e\mu)$ by using the upper limit on the number of signal events expected due to background fluctuations. For this method, the signal and background have to be modeled. First the $e\mu$ invariant mass distribution of $Z \to e\mu$ is described using a Breit-Wigner convoluted with a Gaussian resolution function to model the resonance pole ($m$) with a

natural width ($\Gamma$) convoluted by a detector resolution ($\sigma$):

$$f_{BW}(x, m, \Gamma) \;=\; \frac{1}{(x-m)^2 + \frac{1}{4}\Gamma^2} \tag{9.1}$$

$$f_G(x, m, \sigma) \;=\; e^{-\frac{1}{2}\left(\frac{x-m}{\sigma}\right)^2} \tag{9.2}$$

$$f_S(x, m, \Gamma, \sigma) \;=\; f_{BW}(x, m, \Gamma) \otimes f_G(x, m, \sigma). \tag{9.3}$$

The fit of the signal model to the $Z$ MC data is shown in Figure 9.10. Next, the $e\mu$ invariant mass distribution of the total background is fitted using a exponential function ($f_B(x, a) = e^{ax}$) as shown in Figure 9.11. The combined function of the background and signal is a sum of the Breit-Wigner convoluted with a Gaussian resolution function and the exponential function:

$$f(x, a, N_s, N_b) = N_s f_S(x, m, \Gamma, \sigma) + N_b f_B(x, a) \tag{9.4}$$

where $N_s$ ($N_b$) is the number of events in the signal (background) distribution. All the parameters of the signal function ($m, \Gamma, \sigma$) were fixed to the values obtained from the signal distribution. Note that all these functions are normalized to unity inside the allowed range of $x$ by Roofit [104].

### 9.3.2 A Toy MC for $e\mu$ Determining the $B(Z \to e\mu)$ Upper Limit

Using Roofit [104], 100,000 MC distributions were generated with the background function $f_B(x, a)$ and fitted to the combined distribution $f(x, a, N_s, N_b)$ to obtain the $N_s$ expected due to background fluctuations. The number of signal events was constrained to be positive to ensure convergence in the fit.

To verify the generating and fitting procedure, two sets of toy MC events were generated using the background ($f_B(x, a)$) and signal ($f_S(x, m, \Gamma, \sigma)$ functions with all the parameters fixed. The two sets were combined with different $N_s$ and $N_b$ and fitted to the signal and background combined function $f(x, N_s, N_b)$ to test if it provides the correct numbers for $N_s$ and $N_b$. The results of this test are summarized in Table 9.6, which shows that the method is working as expected.
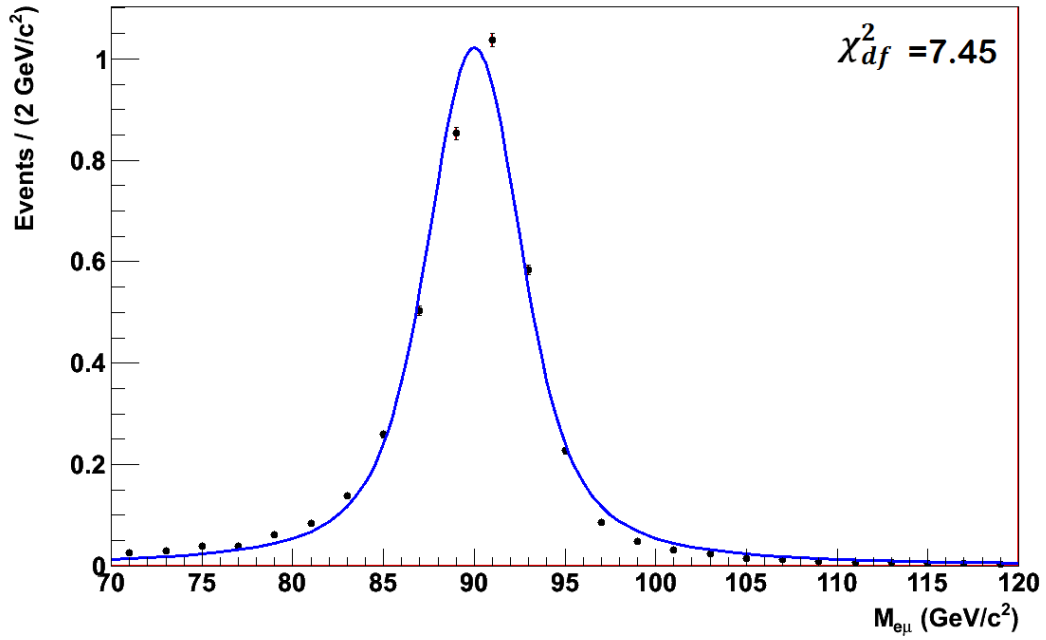
Figure 9.10: A fit to the invariant mass spectrum of $e\mu$ candidates in MC. The signal is scaled to current upper limit on the $BR(Z \to e\mu)$ of $1.7 \times 10^{-6}$ for 650 pb$^{-1}$.
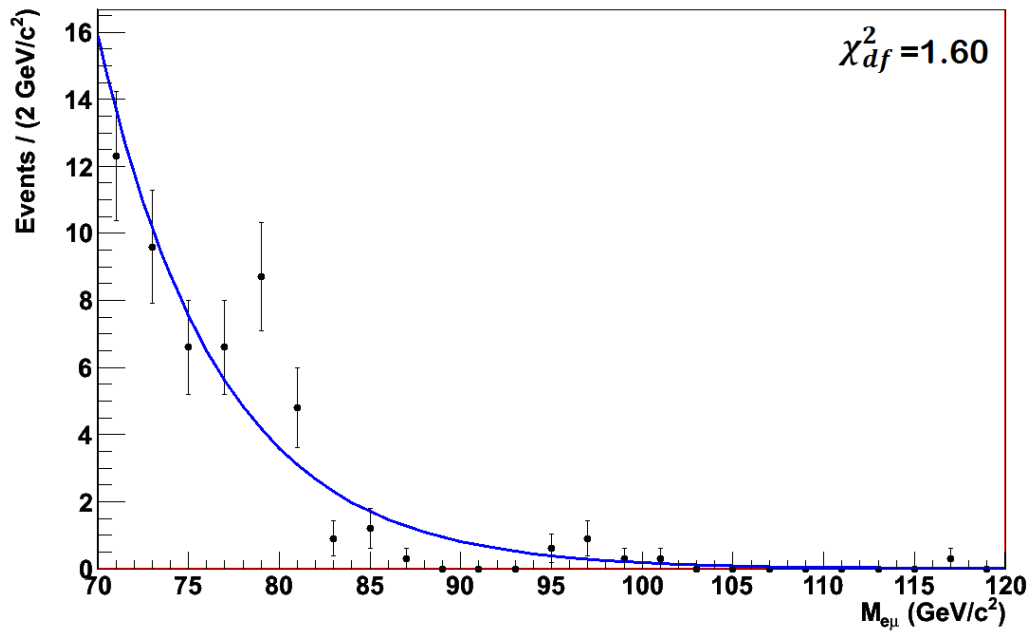


Figure 9.11: A fit to the invariant mass spectrum of $e\mu$ candidates in the background sample of 650 pb$^{-1}$. An exponential function is used.

The distribution of $N_s$ obtained due to background fluctuations is shown in Figure 9.12. The cumulative probability distribution of $N_s$ is shown in Figure 9.13. Using this distribution, the 95% confidence level upper limit for $N_s$ of 3.97 is obtained.
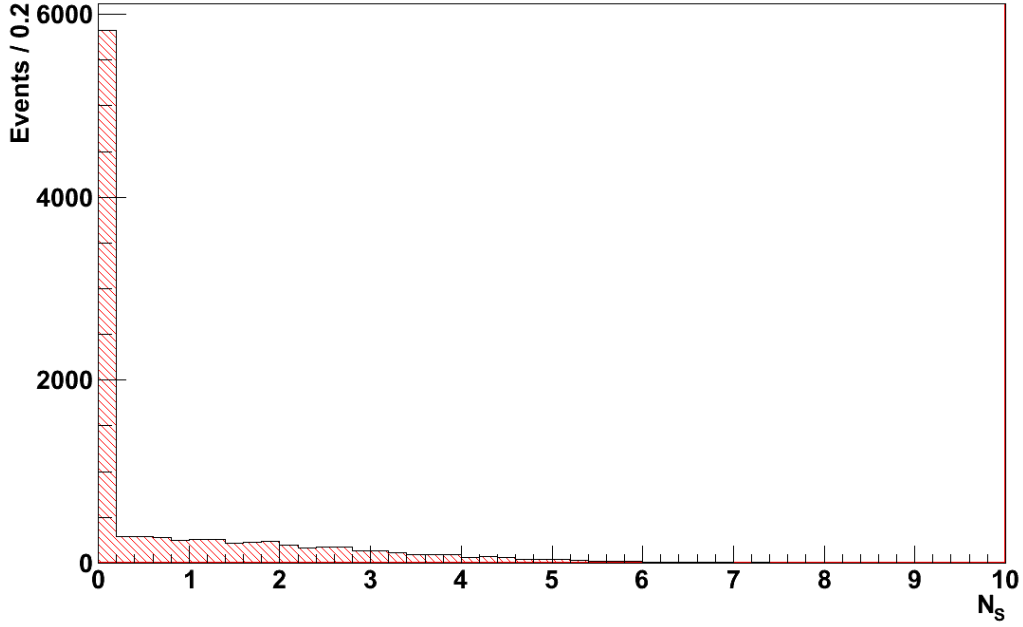


Figure 9.12: The distribution of $N_s$ from the toy MC.

### 9.3.3 The Upper Limit of $B(Z \to e\mu)$

By using the Equation 8.7 and the previously calculated $\overline{N}_Z^0 = (1.52 \pm 0.14) \times 10^7$, $\epsilon_{e\mu} = (9.1 \pm 1.2)$ %, and $N_{95\%} = 3.97$, the expected upper limit is $B(Z \to e\mu) < 1.7 \times 10^{-6}$ at the 95% confidence level for 650 pb$^{-1}$. In this upper limit both the systematic and statistical uncertainties are incorporated using the prescription of Highland and Cousins [102]. This upper limit can be improved as the ATLAS continues to collect data.
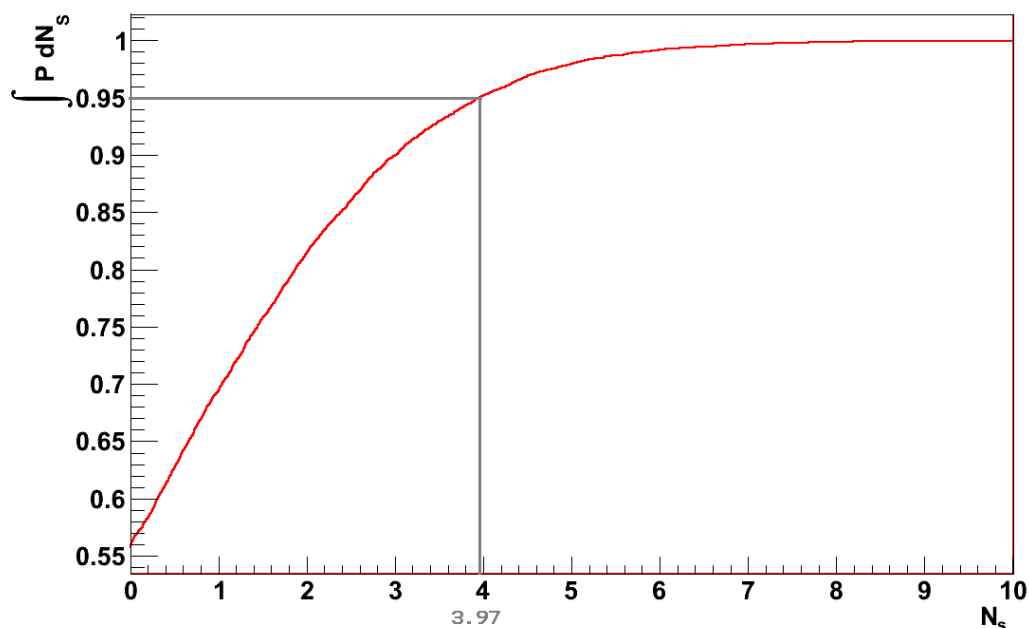
Figure 9.13: The cumulative probability distribution of $N_s$.

## 9.4 Muon Bremsstrahlung in $Z \to \mu\mu$

### 9.4.1 Introduction

Some ATLAS analyses observe large numbers of background events in the $e\mu$ channel from the MC simulated data of $Z \to \mu\mu$. Hence a study of the issue was performed using MC simulated data to measure the rate of fake $e\mu$ from bremsstrahlung, $Z \to \mu\mu$, with one $\mu \to \mu\gamma^*$, $\gamma^*$ reconstructed as an electron through overlapping with the $\mu$ track in the ID.

### 9.4.2 Finding Events with Possible Bremsstrahlung

There are two possible scenarios of muon bremsstrahlung: soft and hard. In case of the soft bremsstrahlung, the muon interact with the material in the detector and emits a photon carrying a part of its energy. In hard bremsstrahlung, the photon carries most of the energy, hence there will be no muon signature in the muon spectrometer.

To simplify the study, all the electrons in the $Z \to \mu\mu$ and $Z \to ee$ datasets are cate-

| Generated | | From fitting | |
|---|---|---|---|
| $N_b$ | $N_s$ | $N_b$ | $N_s$ |
| 99 | 1 | 98.0 | 2.0 |
| 95 | 5 | 94.6 | 5.3 |
| 90 | 10 | 89.7 | 10.3 |
| 50 | 50 | 50.9 | 49.1 |
| 10 | 90 | 13.2 | 86.8 |
| 5 | 95 | 5.4 | 94.6 |

Table 9.6: Results from testing of toy MC method.

gorized to three cases as shown in Figure 9.14. To find the association of truth particles (particles from event generators before going through the detector simulation) and reconstructed particles, a geometrical parameter $\Delta R = \sqrt{(\Delta\phi)^2 + (\Delta\theta)^2}$ is calculated. Type 1 events are defined if a truth electron is found with $\Delta R < 0.2$, from the reconstructed electron. Type 2 events have a reconstructed muon $\Delta R < 0.2$, without a truth electron. Finally, Type 3 events have a truth muon with $\Delta R < 0.2$ from the reconstructed electron but no reconstructed muon in that area. The analysis program was run on the both datasets
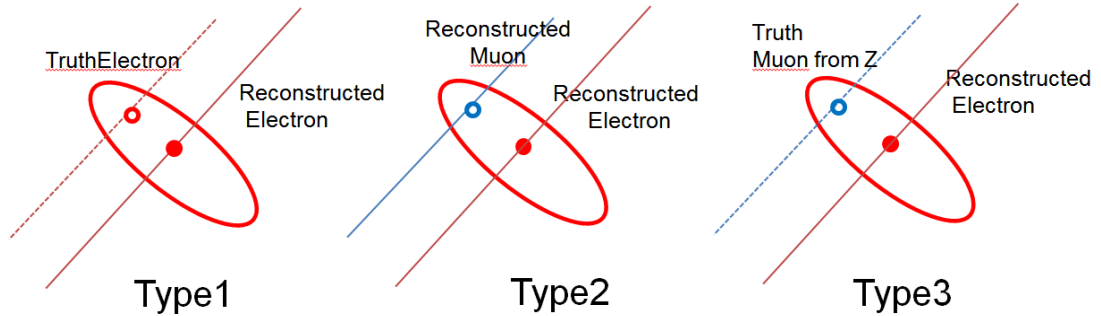


Figure 9.14: Categories of electrons in the $Z \to \mu\mu$.

($Z \to \mu\mu$ and $Z \to ee$).

| Type | Loose | Medium | Medium isolated | Tight | Tight isolated |
|------|-------|--------|-----------------|-------|----------------|
| 2 (soft) | 2451 | 1258 | 1184 | 38 | 35 |
| 3 (hard) | 1462 | 806 | 740 | 29 | 25 |

Table 9.7: Number of soft and hard bremsstrahlung candidates with different electron qualities, for a MC data sample of $Z \rightarrow \mu\mu$ with an integrated luminosity of 4.8 fb$^{-1}$.

### 9.4.3 Effects of Electron Quality

One of the main parameter that can separate the electrons from bremsstrahlung is electron quality (Section 5.4.4). Type 2 and 3 electrons passing the electron quality definition are summarized in Table 9.7.

As a part of the investigation, some of the variables used in the definition of tight electron quality were studied. The variables with the highest discriminating power are: $\eta$ of the electron, number of TRT hits ($N^{TRT}$), and Hadronic leakage ($E^e_{leakage}$). Signal and background distributions for each of the selected variables are shown in Figure 9.15. In the future, with more data, these variables could be used to reduce this type of background.
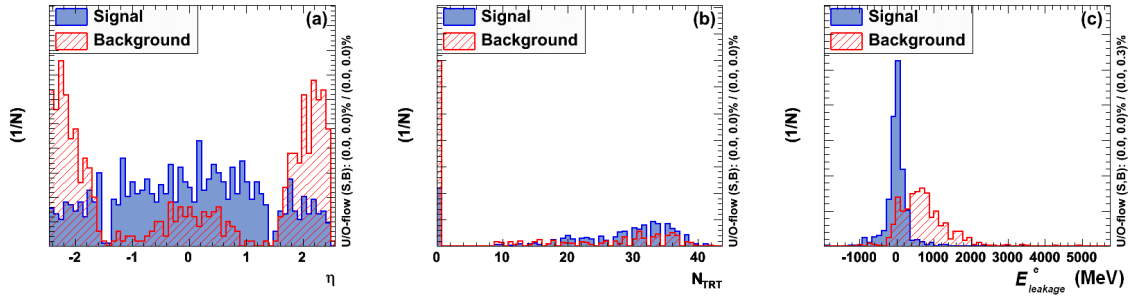


Figure 9.15: (a) $\eta$, (b) number of TRT hits ($N^{TRT}$), and (c) hadronic leakage ($E^e_{leakage}$) of electrons reconstructed from hard bremsstrahlung.

101

### 9.4.4 Conclusions from the Bremsstrahlung

In the $e\mu$ channel, there is some background from $Z \rightarrow \mu\mu$, if one muon has a bremsstrahlung. A higher rate of bremsstrahlung is expected at large $\eta$ since there is more material at large $\eta$. If there is a soft bremsstrahlung, an electron and a muon will both be reconstructed but the overlap removal (Section 7.2) will remove the electron. But in the case of hard bremsstrahlung the fake rate is 5 events/fb$^{-1}$ if using tight electron quality. The definition of tight electron quality uses the number of TRT hits (Section 5.4.4). When it is combined with other selection criteria, the expected background is reduced. With the tuned selection criteria used in this analysis, in 4.8 fb$^{-1}$ of simulated MC data, there were only 2 events of this type left in the invariant mass range of 70 to 120 GeV/c$^2$.

# Chapter 10

## CONCLUSIONS

The work presented in this thesis was performed using data from ATLAS, one of the two general purpose detectors at the LHC at CERN, Geneva, Switzerland. During the construction we (OSU) successfully built, quality controlled, installed, and tested the pixel optical communication system. We (OSU) also built an analysis center to get ATLAS data from the Grid and efficiently do physics analysis. We introduced a signature based data structure (D4PD) for faster processing and to reduce the complexity and size of the ATLAS data.

We searched in ATLAS data for the LFV decay $Z \to e\mu$ in $pp$ collisions at a center of mass energy of 7 TeV. The signature for such a event is an isolated high $p_T$ electron and a muon without jets and not much missing transverse energy. Analysis performed in this thesis looks for candidate events in approximately 3.1 pb$^{-1}$ of data. We observed zero events with $e\mu$ invariant mass above 60 GeV/c$^2$. We set 95% confidence level upper limits on the $Z \to e\mu$ branching ratio as 2.0 $\times 10^{-4}$. We also showed that it is possible to be have a sensitivity near current upper limit with $\sim$ 650 pb$^{-1}$ of data.

# Bibliography

[1] E. Fermi, "Versuch einer theorie der -strahlen. i," *Z. Physik* **88** (1934) 161–177. Available here.

[2] J. Schwinger, "A theory of the fundamental interactions," *Ann. Phys.* **2** (1957) 407–434. Available here.

[3] S. Bludman, "On the universal fermi interaction," *Il Nuovo Cimento* **6** (1958) 433–445.

[4] S. L. Glashow, "Partial-symmetries of weak interactions," *Nucl. Phys.* **22** (1961) 579–588. Available here.

[5] P. W. Higgs, "Broken symmetries and the masses of gauge bosons," *Phys. Rev. Lett.* **13** (1964) 508–509.

[6] S. Weinberg, "A model of leptons," *Phys. Rev. Lett.* **19** (1967) 1264–1266.

[7] M. Gell-Mann, "The interpretation of the new particles as displaced charge multiplets," *Il Nuovo Cimento* **4** (1956) 848–866. Available here.

[8] K. Nishijima, "Charge independence theory of $V$ particles," *Progr. Theoret. Phys.* **13** (1955) 285–304. Available here.

[9] S. H. Neddermeyer and C. D. Anderson, "Note on the nature of cosmic-ray particles," *Phys. Rev.* **51** (1937) 884–886.

[10] E. P. Hincks and B. Pontecorvo, "Search for gamma-radiation in the 2.2-microsecond meson decay process," *Phys. Rev.* **73** (1948) 257–258.

[11] L. Michel, "$\mu$-meson decay and $\beta$-radioactivity," *Phys. Rev.* **86** (1952) 814–815.

[12] G. Feinberg, "Decays of the $\mu$ meson in the intermediate-meson theory," *Phys. Rev.* **110** (1958) 1482–1483.

[13] D. Berley, J. Lee, and M. Bardon, "Upper limit for the decay mode $\mu \to e + \gamma$," *Phys. Rev. Lett.* **2** (1959) 357–359.

[14] G. Danby *et al.*, "Observation of high-energy neutrino reactions and the existence of two kinds of neutrinos," *Phys. Rev. Lett.* **9** (1962) 36–44.

[15] M. L. Perl *et al.*, "Evidence for anomalous lepton production in $e^+ - e^-$ annihilation," *Phys. Rev. Lett.* **35** (1975) 1489–1492.

[16] K. Kodama *et al.*, "Observation of $\tau$ neutrino interactions," *Phys. Lett. B* **504** (2001) 218–224. Available here.

[17] M. C. Gonzalez-Garcia and Y. Nir, "Developments in neutrino physics," *Rev. Mod. Phys.* **75** (2003) 345–402.

[18] B. Gripaios, "Composite leptoquarks at the LHC," *JHEP* **02** (2010) s08021.

[19] G.-J. Ding and M.-L. Yan, "Lepton flavor violating $\mu \to e\gamma$ and $\mu - e$ conversion in unparticle physics," *Phys. Rev. D* **77** (2008) 014005.

[20] M. Hirsch *et al.*, "Majoron emission in $\mu$ and $\tau$ decays revisited," *Phys. Rev. D* **79** (2009) 055023.

[21] M. L. Brooks *et al.*, "New limit for the family number non-conserving decay $\mu^+ \to e^+\gamma$," *Phys. Rev. Lett.* **83** (1999) 1521–1524.

[22] M. Ahmed *et al.*, "Search for the lepton-family-number nonconserving decay $\mu^+ \to e^+\gamma$," *Phys. Rev.* **D65** (2002) 112002.

[23] R. D. Bolton *et al.*, "Search for rare muon decays with the crystal box detector," *Phys. Rev.* **D38** (1988) 2077.

[24] U. Bellgardt *et al.*, "Search for the decay $\mu^+ \to e^+e^+e^-$," *Nucl. Phys.* **B299** (1988) 1.

[25] B. Aubert *et al.*, "Searches for lepton flavor violation in the decays $\tau \to e\gamma$ and $\tau \to \mu\gamma$," *Phys. Rev. Lett.* **104** (2010) 021802.

[26] Y. Miyazaki *et al.*, "Search for lepton flavor violating tau decays into three leptons," *Phys. Lett.* **B660** (2008) 154–160.

[27] R. Akers *et al.*, "A search for lepton flavor violating $Z^0$ decays," *Z. Phys.* **C67** (1995) 555–564.

[28] P. Abreu *et al.*, "Search for lepton flavour number violating $Z^0$ decays," *Z. Phys.* **C73** (1997) 243–251.

[29] J. Nix *et al.*, "First search for $K_L \to \pi^0\pi^0\nu\bar{\nu}$," *Phys. Rev.* **D76** (2007) 011101.

[30] B. Aubert *et al.*, "Search for flavor-changing neutral current and lepton flavor violating decays of $D^0 \to \ell^+\ell^-$," *Phys. Rev. Lett.* **93** (2004) 191801.

[31] T. Aaltonen *et al.*, "Search for the decays $B^0_{(s)} \to e^+\mu^-$ and $B^0_{(s)} \to e^+e^-$ in CDF Run II," *Phys. Rev. Lett.* **102** (2009) 201801.

[32] P. Jenni *et al.*, "ATLAS high-level trigger, data-acquisition and controls," ATLAS-TDR-016, CERN, Geneva, 2003.

[33] E. W. N. Glover, "Rare $Z$ decays and new physics,". Invited talk at DPF Conf., Houston, TX, Jan 3-6, 1990.

[34] G. Altarelli *et al.*, "Workshop on $Z$ physics at LEP1 : General meetings, v.2 : $Z$ physics at LEP 1 - higgs search and new physics," CERN-89-08-V-2, CERN, Geneva, 1989.

[35] ATLAS Collaboration, "ATLAS detector and physics performance:1," ATLAS-TDR-014, CERN, Geneva, 1999.

[36] L. Evans and P. Bryant, "LHC machine," *JINST* **3** (2008) P02013.

[37] G. Aad *et al.*, "ATLAS pixel detector electronics and sensors," *JINST* **3** (2008) P07007.

[38] A. Ahmad *et al.*, "The silicon microstrip sensors of the ATLAS semiconductor tracker," *Nucl. Instrum. Methods Phys. Res. Sect. A* **578** (2007) 98–118.

[39] L. G. Johansen *et al.*, "Radiation studies of silicon-microstrip detectors for use in ATLAS and SCT," *IEEE T. Nucl. Sci.* **49** (2002) 2919–2922.

[40] P. J. Dervan, "The results of the irradiations of microstrip detectors for the ATLAS tracker (SCT)," *Nucl. Instrum. Methods Phys. Res. Sect. A* **514** (2003) 163–166.

[41] Y. Unno, "ATLAS silicon microstrip detector system (SCT)," *Nucl. Instrum. Methods Phys. Res. Sect. A* **511** (2003) 58–63.

[42] F. Campabadal *et al.*, "Design and performance of the ABCD3TA ASIC for readout of silicon strip detectors in the ATLAS semiconductor tracker," *Nucl. Instrum. Methods Phys. Res. Sect. A* **552** (2005) 292–328.

[43] A. Abdesselam *et al.*, "The ATLAS SCT optoelectronics and the associated electrical services," ATL-INDET-PUB-2007-001, CERN, Geneva, 2006.

[44] T. Loddenkoetter, "Alignment of the ATLAS inner detector tracking system," ATL-INDET-PROC-2010-014, CERN, Geneva, 2010.

[45] A. Mayne, "ATLAS silicon microstrip tracker operation and performance," ATL-INDET-PROC-2010-018, CERN, Geneva, 2010.

[46] E. Abat *et al.*, "The ATLAS transition radiation tracker (TRT) proportional drift tube: design and performance," *JINST* **3** (2008) P02013.

[47] M. Capeans, "The transition radiation tracker of the ATLAS experiment," *IEEE T. Nucl. Sci.* **51** (2004) 994–1000.

[48] A. Alonso, "Commissioning and performance of the ATLAS transition radiation tracker with high energy collisions at LHC," ATL-INDET-PROC-2010-017, CERN, Geneva, 2010.

[49] ATLAS Collaboration, "The ATLAS experiment at the CERN large hadron collider," *JINST* **3** (2008) S08003.

[50] B. Aubert *et al.*, "Construction, assembly and tests of the ATLAS electromagnetic barrel calorimeter," *Nucl. Instrum. Methods Phys. Res. Sect. A* **558** (2006) 388–418.

[51] B. Aubert *et al.*, "Performance of the ATLAS electromagnetic calorimeter end-cap module," *Nucl. Instrum. Methods Phys. Res. Sect. A* **500** (2003) 178–201.

[52] ATLAS Electromagnetic Liquid Argon Endcap Calorimeter Group, "Construction, assembly and tests of the ATLAS electromagnetic end-cap calorimeters," *JINST* **3** (2008) P06002.

[53] J. Abdallah *et al.*, "Design, construction and installation of the ATLAS hadronic barrel scintillator-tile calorimeter," ATL-TILECAL-PUB-2008-001, CERN, Geneva, 2007.

[54] D. M. Gingrich *et al.*, "Construction, assembly and testing of the ATLAS hadronic end-cap calorimeter," *JINST* **2** (2007) P05005.

[55] A. Artamonov *et al.*, "The ATLAS forward calorimeter," *JINST* **3** (2008) P02010.

[56] S. Palestini, "The muon spectrometer of the ATLAS experiment," *Nucl. Phys. B, Proc. Suppl.* **125** (2003) 337–345.

[57] Y. Arai *et al.*, "On-chamber readout system for the ATLAS MDT muon spectrometer," *IEEE T. Nucl. Sci.* **51** (2004) 2196–2200.

[58] G. Aielli *et al.*, "Test of ATLAS RPCs front-end electronics," *Nucl. Instrum. Methods Phys. Res. Sect. A* **508** (2003) 189–193.

[59] R. Achenbach *et al.*, "The ATLAS level-1 calorimeter trigger," *JINST* **3** (2008) P03001.

[60] S. Ask *et al.*, "The ATLAS central level-1 trigger logic and TTC system," *JINST* **3** (2008) P08002.

[61] T. Rohe, "Design and test of pixel sensors for the ATLAS pixel detector," *Nucl. Instrum. Methods Phys. Res. Sect. A* **460** (2001) 55–66.

[62] R. Richter *et al.*, "Strip detector design for ATLAS and HERA-B using two-dimensional device simulation," *Nucl. Instrum. Methods Phys. Res. Sect. A* **377** (1996) 412–421.

[63] G. Lindstrm *et al.*, "Radiation hard silicon detectors - developments by the RD48 (ROSE) collaboration," *Nucl. Instrum. Methods Phys. Res. Sect. A* **466** (2001) 308–326.

[64] T. Fritzsch *et al.*, "Experience in fabrication of multichip-modules for the ATLAS pixel detector," *Nucl. Instrum. Methods Phys. Res. Sect. A* **565** (2006) 309–313.

[65] K. Arms *et al.*, "ATLAS pixel opto-electronics," *Nucl. Instrum. Methods Phys. Res. Sect. A* **554** (2005) 458–468.

[66] ATLAS Collaboration, "The ATLAS inner detector commissioning and calibration," *ArXiv e-prints* (2010) `1004.5293`.

[67] H. M. Gray, "Alignment of the ATLAS inner detector tracking system," *JINST* **4** (2009) P03018. Available here.

[68] A. Andreazza, "ATLAS pixel detector operation and performance," ATL-INDET-PROC-2010-015, CERN, Geneva, 2010.

[69] https://twiki.cern.ch/twiki/bin/view/AtlasProtected/McGeneratorsForAtlas.

[70] T. Sjostrand, S. Mrenna, and P. Z. Skands, "PYTHIA 6.4 physics and manual," *JHEP* **05** (2006) 026.

[71] G. Corcella *et al.*, "HERWIG 6.5: an event generator for hadron emission reactions with interfering gluons (including supersymmetric processes)," *JHEP* **01** (2001) 010.

[72] T. Gleisberg *et al.*, "Event generation with SHERPA 1.1," *JHEP* **02** (2009) 007.

[73] Z. Was, "TAUOLA the library for tau lepton decay, and KKMC/KORALB/KORALZ/... status report," *Nucl. Phys. Proc. Suppl.* **98** (2001) 96–102.

[74] F. W. Bopp *et al.*, "Rapidity gaps and the PHOJET monte carlo," `hep-ph/9803437`.

[75] P. Golonka *et al.*, "The tauola-photos-F environment for the TAUOLA and PHOTOS packages, release II," *Comput. Phys. Commun.* **174** (2006) 818–835. Available here.

[76] J. M. Butterworth, J. R. Forshaw, and M. H. Seymour, "Multiparton interactions in photoproduction at HERA," *Z. Phys.* **C72** (1996) 637–646.

[77] S. Frixione and B. R. Webber, "Matching NLO QCD computations and parton shower simulations," *JHEP* **06** (2002) 029.

[78] M. L. Mangano, "ALPGEN, a generator for hard multiparton processes in hadronic collisions," *JHEP* **07** (2003) 001.

[79] J. Alwall *et al.*, "MadGraph/MadEvent v4: the new web generation," *JHEP* **09** (2007) 028.

[80] http://lcgapp.cern.ch/project/simu/generator/.

[81] M. Dobbs and J. Hansen, "The HepMC C++ Monte Carlo event record for high energy physics," *Comput. Phys. Commun.* **134** (2001) 41–46.

[82] J. Allison *et al.*, "GEANT4 developments and applications," *IEEE T. Nucl. Sci.* **53** (2006) 270 –278.

[83] T. Cornelissen *et al.*, "Concepts, design and implementation of the ATLAS new tracking," ATL-SOFT-PUB-2007-007, CERN, Geneva, 2007.

[84] F. Akesson *et al.*, "ATLAS inner detector event data model," ATL-SOFT-PUB-2007-006, CERN, Geneva, 2007.

[85] G. Aad *et al.*, "Expected performance of the ATLAS experiment: detector, trigger and physics," CERN-OPEN-2008-020, CERN, Geneva, 2009.

[86] G. Aad *et al.*, "The ATLAS inner detector commissioning and calibration," arXiv:1004.5293, CERN, Geneva, 2010.

[87] V. Rossetti, "Commissioning of the ATLAS tile hadronic calorimeter with cosmic muons, single beams and first collisions," ATL-TILECAL-PROC-2010-009, CERN, Geneva, 2010.

[88] G. Zevi Della Porta, "Recent performance results with the ATLAS muon spectrometer," ATL-MUON-PROC-2010-003, CERN, Geneva, 2010.

[89] W. Lampl *et al.*, "Calorimeter clustering algorithms: description and performance," ATL-COM-LARG-2008-003, CERN, Geneva, 2008.

[90] ATLAS Collaboration, "Measurement of missing transverse energy," ATL-COM-PHYS-2009-118, CERN, Geneva, 2009.

[91] C. Kesselman and I. Foster, *The Grid: Blueprint for a New Computing Infrastructure*, Morgan Kaufmann Publishers, 1998.

[92] A. Hoecker *et al.*, "TMVA - toolkit for multivariate data analysis," *ArXiv Physics e-prints* (2007).

[93] http://cernvm.cern.ch/cernvm/.

[94] J. Hartert and I. Ludwig, "Electron isolation in the ATLAS experiment," ATL-PHYS-INT-2010-052, CERN, Geneva, 2010.

[95] ATLAS Collaboration, "Measurement of the $Z \to ll$ production cross section in proton-proton collisions at $\sqrt{s} = 7$ TeV with the ATLAS detector," ATLAS-CONF-2010-076, CERN, Geneva, 2010.

[96] ATLAS Collaboration, "Measurement of the $Wl\nu$ production cross-section and observation of $Z \to ll$ production in proton-proton collisions at $\sqrt{s} = 7$ TeV with the ATLAS detector," ATLAS-CONF-2010-051, CERN, Geneva, 2010.

[97] ATLAS Collaboration, "Performance of the ATLAS electromagnetic calorimeter for $\pi^0 \to \gamma\gamma$ and $\eta \to \gamma\gamma$ events," ATLAS-CONF-2010-006, CERN, Geneva, 2010.

[98] C. Amsler *et al.*, "Review of particle physics," *Phys. Lett.* **B667** (2008) 1.

[99] ATLAS Collaboration, "Performance of the missing transverse energy reconstruction and calibration in proton-proton collisions at a center-of-mass energy of 7 TeV with the ATLAS detector," ATLAS-CONF-2010-057, CERN, Geneva, 2010.

[100] ATLAS Collaboration, "Muon reconstruction performance," ATLAS-CONF-2010-064, CERN, Geneva, 2010.

[101] G. J. Feldman and R. D. Cousins, "Unified approach to the classical statistical analysis of small signals," *Phys. Rev. D* **57** (1998) 3873–3889.

[102] R. D. Cousins and V. L. Highland, "Incorporating systematic uncertainties into an upper limit," *Nucl. Instrum. Methods Phys. Res. Sect. A* **320** (1992) 331–335.

[103] R. A. Fisher, "The use of multiple measurements in taxonomic problems," *Annals Eugen.* **7** (1936) 179–188.

[104] W. Verkerke and D. Kirkby, "The roofit toolkit for data modeling," `physics/0306116`. Available here.

[105] A. Lazzaro *et al.*, "MINUIT package parallelization and applications using the RooFit package," *J. Phys.: Conf. Ser.* **219** (2010) 042044.

# Appendix A
## FITTING PROCEDURE

In this analysis, the invariant mass spectrum of di-leptons near the $Z$ pole is fitted using RooFit [104]. We choose a convoluted Breit-Wigner (Voigtian) function to model the resonance pole ($m$) with a natural width ($\Gamma$) convoluted by a detector resolution ($\sigma$):

$$f_{BW}(x, m, \Gamma) = \frac{1}{(x-m)^2 + \frac{1}{4}\Gamma^2} \tag{A.1}$$

$$f_G(x, m, \sigma) = e^{-\frac{1}{2}\left(\frac{x-m}{\sigma}\right)^2} \tag{A.2}$$

$$f(x, m, \Gamma, \sigma) = f_{BW}(x, m, \Gamma) \otimes f_G(x, \sigma). \tag{A.3}$$

The data is fit using a maximum likelihood method, since we have limited statistics. Likelihood is defined as:

$$\mathcal{L}(m, \Gamma, \sigma) = \prod_i f(x_i, m, \Gamma, \sigma) \tag{A.4}$$

$$-log(\mathcal{L}(m, \Gamma, \sigma)) = -\sum_i f(x_i, m, \Gamma, \sigma). \tag{A.5}$$

Instead of fixing the normalization to the number of events in the histogram, an extended likelihood fit is used to include the overall yield as a parameter as follows:

$$-log(\mathcal{L}(m, \Gamma, \sigma)) = -\sum_i f(x_i, m, \Gamma, \sigma) + N_{exp} - N_{obs}\, ln\,(N_{exp}). \tag{A.6}$$

RooFit use HESSE [105] to estimate step size and then uses MIGRAD [105] to minimize $-log\mathcal{L}$ and MINOS [105] to extract the uncertainties.

# Appendix B
## LIST OF ABBREVIATIONS

**ADC** Analog to Digital Converter

**ANN** Artificial Neural Networks

**AOD** Analysis Object Data

**ASD** Amplifer/Shaper/Discriminator

**ASDBLR** Amplifier, Shaper, Discriminator Base Line Restoration Integrated Circuit

**ASM** Amplifier and Shaping Module

**ATLAS** Toroidal LHC ApparatuS

**BDT** Boosted Decision Trees

**BNL** Brookhaven National Laboratory

**BOC** Back Of Crate

**BPM** Bi-Phase Modulated

**CERN** European Organization for Nuclear Research

**CP** Cluster Processor

**CSC** Cathode-Strip Chambers

**CSM** Chamber Service Modules

**CSR** Common Serial Resistance

**CSR** Computer System Commissioning

**CSR** Analysis Object Data

**CTP** Trigger Processor

**CTP** Central Trigger Processor

**D3PD** Level 3 Derived Physics Data

**DAQ/HLT** Data Acquisition System/High-Level Trigger

**DFM** Data Flow Manager

**DPD** Derived Physics Data

**DSP** Digital Signal Processors

**DTMROC** Drift-Time Measuring ReadOut Chip

**$\mathbf{E}_T^{miss}$** Missing Transverse Energy

**EF** Event Filter

**EMBC** ElectroMagnetic Barrel Calorimeter

**EMEC** ElectroMagnetic End-cap Calorimeter

**ESD** Event Summary Data

**EoC** End of Column

**FCal** Liquid-argon Forward Calorimeter

**FSR** Final State Radiation

**GRL** Good Run List

**HEC** Liquid argon Hadronic End-cap Calorimeter

**HLT**  High-Level Trigger

**ID**  Inner Detector

**ISR**  Initial State Radiation

**JEP**  Jet/Energy-sum Processor

**JO**  Job Options

**L1**  Level-1 hardware trigger

**L1A**  Level-1 Accept

**L1Calo**  Level-1 Calorimeter Trigger

**L2**  Level-2 hardware trigger

**L2PU**  Level-2 trigger Processing Units

**L2SV**  Level-2 SuperVisor

**LEP**  Large Electron Positron Collider

**LFV**  Lepton Flavor Violation

**LHC**  Large Hadron Collider

**LVDS**  Low Voltage Differential Signaling

**MC**  Monte Carlo

**MCC**  Module Control Chip

**MDT**  Monitored Drift Tube Chambers

**MuId**  Muon Identification

**OSG**  Open Science Grid

**OSU**  The Ohio State University

**Opto-links** Optical fiber links

**PDF** Probability Density Functions

**PP1** Patch Panel 1

**PROOF** Parallel ROOT Framework

**RDO** Raw Data Output

**ROB** Read Out Buffers

**ROD** Read Out Drivers

**ROI** Region Of Interest

**ROL** Read Out Links

**RPC** Resistive Plate Chambers

**SCA** Switched Capacitor Array

**SCT** SemiConductor Tracker

**SM** Standard Model

**SQP** Service Quarter Panel

**STO** Slow Trun On

**StaCo** Statistical Correlations

**TDC** Time to Digital Converter

**TGC** Thin Gap Chambers

**TMVA** Tool Kit for Multivariate Analysis

**TRT** Transition Radiation Tracker

**TTC** Trigger Timing and Control

**TileCal** Scintillator-Tile hadronic Calorimeter

**ToT** Time over Threshold

**VCSEL** Vertical Cavity Surface Emitting Lasers

**VDC** VCSEL Driver Chip

**VM** Virtual Machine

$\mathbf{X}_0$ Radiation lengths